VARIATION OF ELECTRON AND ION DENSITY DISTRIBUTION ALONG EARTH'S

MAGNETIC FIELD LINE DEDUCED FROM WHISTLER MODE SOUNDING OF

IMAGE/RPI SATELLITE BELOW ALTITUDE 5000 KM

by

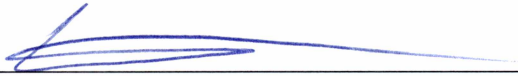Susmita Hazra

RECOMMENDED: _____
Dr. Joan Braddock

_____
Dr. David Newman

_____
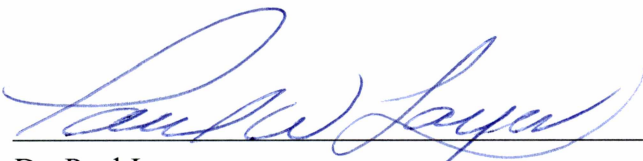Dr. William Simpson

_____
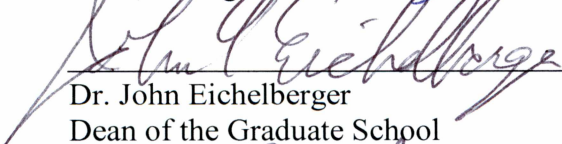Dr. Martin Truffer
Advisory Committee Chair

_____
Dr. Curt Szuberla
Chair, Department of Physics
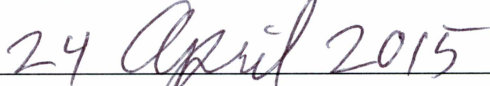
APPROVED: _____
Dr. Paul Layer
Dean, College of Natural Science and Mathematics

_____
Dr. John Eichelberger
Dean of the Graduate School

_____
Date

VARIATION OF ELECTRON AND ION DENSITY DISTRIBUTION ALONG EARTH'S MAGNETIC FIELD LINE DEDUCED FROM WHISTLER MODE (WM) SOUNDING OF IMAGE/RPI SATELLITE BELOW ALTITUDE 5000 KM

A

DISSERTATION

Presented to the Faculty

of the University of Alaska Fairbanks

in Partial Fulfillment of the Requirements

for the Degree of

DOCTOR OF PHILOSOPHY

By

Susmita Hazra

Fairbanks, Alaska

May 2015

Abstract

This thesis provides a detailed survey and analysis of whistler mode (WM) echoes observed by IMAGE/RPI satellite during the years 2000-2005 below the altitude of 5000 km. Approximately 2500 WM echoes have been observed by IMAGE during this period. This includes mostly specularly reflected whistler mode (SRWM) echoes and ~400 magnetospherically reflected whistler mode (MRWM) echoes. Stanford 2D raytracing simulations and the diffusive equilibrium density model have been applied to 82 cases of MRWM echoes, observed during August-December of the year 2005 below 5000 km to determine electron and ion density measurements along Earth's magnetic field line. These are the first results of electron and ion density measurements from WM sounding covering L-shells ~1.6-4, a wide range of geomagnetic conditions (K_p 0+ to 7), and during solar minima (F10.2~70-120) in the altitude range 90 km to 4000 km. The electron and ion density profiles obtained from this analysis were compared with in situ measurements on IMAGE (passive recording; electron density (N_e)), DMSP (~850 km; N_e and ions), CHAMP (~350 km; N_e), Alouette (~500-2000 km; Ne and ions), ISIS-1, 2 (~600-3500 km; N_e, ions), AE (~130-2000 km; ions) satellites, bottom side sounding from nearby ionosonde stations (N_e), and those by GCPM (Global Core Plasma Model), IRI-2012 (International Reference Ionosphere). Based on this analysis it is found that: (1) N_e shows a decreasing trend from L-shell 1.6 to 4 on both the day and night sides of the plasmasphere up to altitude ~1000 km, which is also confirmed by the GCPM and IRI-2012 model. (2) Above ~2000 km altitude, GCPM underestimates N_e by ~30-90% relative to RPI passive measurements, WM sounding results. (3) Below 1500 km, the N_e is higher at day side than night side MLT (Magnetic Local Time). Above this altitude, significant MLT dependence of electron density is not seen. (4) Ion densities from WM sounding measurements are within 10-35% of those from the Alouette, AE, and DMSP satellites. (5) The effective ion mass in the day side is more than two times higher than night side below altitude ~1500 km. (6) The O^+/H^+ and $O^+/(H^++He^+)$ transition heights at day side are ~300-500 km higher than night side; the transition heights from the IRI-2012 model lie within the uncertainty limit of WM sounding for night side, but for day side (L-shell>2.5) they are 200 km higher than WM uncertainty limits. (7) foF2 (F2 peak plasma densities) from ionosonde stations and the IRI-2012 model are ~1.5-3 MHz higher than those from WM sounding during daytime. These measurements are very important as the ion density profile along geomagnetic field lines is poorly known. They can lead to a better understanding of global cold plasma distribution inside the plasmasphere at low altitude and thereby bridge the gap between high topside ionosphere and plasmasphere measurements. These results

will provide important guidance for the design of future space-borne sounders in terms of frequency and virtual range, in order to adequately cover ion density measurements at low altitudes and wide range of MLTs, solar and geophysical conditions.

Table of Contents

List of Figures

List of Tables

Acknowledgments

I would like to thank Prof. Vikas Sonwalkar for introducing me to the IMAGE data and this research topic. I gratefully acknowledge valuable discussions and suggestions from my Committee, Prof. Martin Truffer (chair), Prof. David Newman, Prof. Joan Braddock, and Prof William Simpson. My appreciation goes out to two anonymous external reviewers, their suggestions were very helpful in bringing out the scientific aspect of this work. This thesis could not have been accomplished without the help, constant support, encouragement, and understanding from graduate school dean John Eichelberger. I would like to thank Carol Holz, associate director, Office of International Programs and Initiatives of UAF for her help and support during this course of study. I would like to thank College of Natural Science and Mathematics (CNSM), College of Engineering and Mines (CEM), Graduate School of University of Alaska Fairbanks for their financial support as Teaching assistantship and thesis completion fellowship. I also thank NASA for financial support during first two years of my PhD.

I am grateful to all my good friends here in Fairbanks for their support and inspiration when I needed it the most. I thank my family back in India for being my source of strength and for their unconditional love. Last but not the least, I thank my wonderful husband, my best friend Kumar Mayank and my little daughter Ojasvi for being a part of my life and making it so beautiful.

Chapter 1 Introduction

1.1 The Earth's ionosphere and plasmasphere

The ionosphere is the ionized part of Earth's atmosphere starting from an altitude of 60 km and extending up to 1000 km. Two different ionization processes are involved in its creation: photoionization, principally by solar extreme ultraviolet (EUV) and x-ray photons, and impact ionization by charged particles (including solar and galactic cosmic rays). The ionosphere is vertically structured in three layers or regions that differ from one another in composition, density, ionization sources, degree of variability, chemistry, and dynamics: the D (60-85 km), E (85- 140 km), and F (140-1000 km) regions (NASA's handbook 'The Earth's Ionosphere'). In the day time, the F-region has two divisions, F1 and F2. The F1-region disappears at night as the concentration of electrons decreases above the E-region. The maximum ionospheric plasma density occurs in the noon F-region, called the F2 peak. The F2 peak varies with time of the day, season, solar cycle, and latitude. NO^+ and O_2^+ are the principal ions composing the D and E regions, O^+ is the dominant ion in the F-region (Kelly, 2009). He^+ is a minor atomic constituent at all times. Above the F-region is a region of exponentially decreasing density known as the topside ionosphere. This region extends to an altitude of a few thousand kilometers and, at mid-latitudes, feeds into the plasmasphere. A transition between predominantly O^+ ionosphere to predominantly H^+ occurs moving upward in the topside ionosphere.

The plasmasphere is a torus of plasma in the inner part of the magnetosphere, comprising the co-rotating region of the magnetosphere. Magnetic field lines there are closed and approximately dipolar, permitting filling of the plasmasphere by plasma escaping from the Earth's ionosphere. The cold plasma density in the plasmasphere is a fundamental parameter in propagation of plasma waves and the interaction of these waves with energetic particles. The electron density inside the plasmasphere is quite high, ranging from about 10 to 10^4 electrons/cc. The plasmasphere is populated by the outflow of ions and electrons from the underlying ionosphere along mid- and low-latitude geomagnetic field lines (Lemaire, 1986). The plasma in the plasmasphere is mostly H^+ at high den-
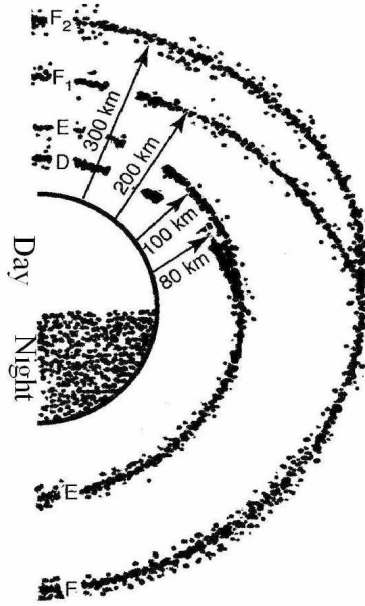
Figure 1.1 Earth's ionospheric layers during day and night time (Courtesy: The Ionosphere, Space Weather and Telecommunications).

sities (10 to 10^3/cc) and low temperatures (1 eV) relative to the rest of the magnetosphere. The plasmasphere is highly variable both spatially and temporally, responding to changes in geomagnetic indices, ring current, penetration and shielding electric fields, and subauroral electric fields. Consequently, the plasmasphere exhibits erosion, emptying, and refilling during active times, along with a high level of structure (Singh and Horwitz, 1992; Reinisch et al., 2004; Johnston, 2007). The plasmasphere was independently identified by in situ plasma measurements and ground-based whistler observations in the early 1960s. Carpenter (1963a) used observations of whistlers, radio waves propagating along geomagnetic field lines, to identify a steep density gradient corresponding to the outer edge of the plasmasphere. Gringauz (1963) used plasma observations from the Lunik Moon probes to identify the same density gradient. Later in the 1960s, the basic theoretical picture emerged with the plasmasphere as the magnetospheric region where co-rotation dominates over the cross-tail electric field. The IMAGE satellite considerably advanced understanding of plasmasphere dynamics and revealed new degrees of structure.

Convection-driven erosion of the outer plasmasphere causes it to contract and creates an abrupt gradient or drop in the number density of the plasmaspheric plasma, called the plasmapause. It marks the boundary of the main body of the plasmasphere, which becomes roughly circular in shape (with a slightly greater radius at dusk). Carpenter et al. (2000) showed from CRESS data that the widths at plasmapause (ΔL) range from ~0.5 to ~1.5 and density drops by a factor of ~2-5. Fu et
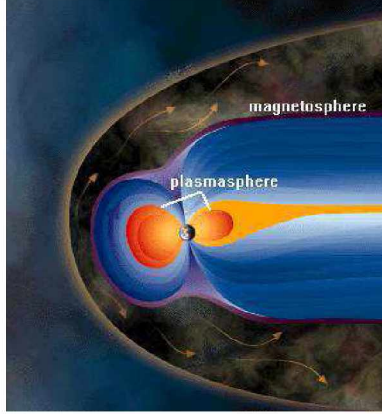
Figure 1.2 A schematic diagram of Earth's plasmasphere (courtesy: http://en.wikipedia.org/wiki/Plasmasphere).

al., (2010) measured the plasmapause from IMAGE/RPI dynamic spectra where the Ne decreases by a factor of 6 over a region of $\sim 0.25 R_e$, where R_e is the Earth's radius. The plasmapause radius tends to vary with the level of geomagnetic activity. During geomagnetic storms the radius is found near L=2 or less. During quiet times the radius is observed beyond L = 8 (Gringauz and Bezrukikh, 1976; Carpenter, 1981; Lemaire and Gringauz, 1998).

1.2 Whistler mode wave

The whistler mode (WM) is a cold plasma wave mode with an upper cutoff frequency at the plasma frequency (f_{pe}) or the cyclotron frequency (f_{ce}), whichever is lower. Waves propagating in WM are found in all regions of the Earth's magnetosphere. These waves may originate from sources outside the magnetosphere, such as lightning or VLF transmitters, or they may originate within the magnetosphere as a result of resonant wave-particle interactions, tending to travel along the magnetic field lines of the Earth. WM waves have been detected on spacecraft carrying a plasma wave receiver and at numerous ground stations (Gurnett and Inan, 1988; Hayakawa, 1995; Helliwell, 1965; Shawhan, 1979; Sonwalkar, 1995). WM propagation, including reflection, refraction, guiding, and scattering, determines the extent to which whistler mode energy can remain trapped in the magnetosphere and influence the nature of wave-particle interactions. Plasma density irregularities to a large extent determine the nature of whistler mode propagation. The WM refractive index can vary over a wide range of values ($\sim$1-10,000). This leads to refraction and scattering of WM waves by field-aligned irregularities (FAIs) of widely varying scale lengths. The main advantage of WM sounding over other modes of sounding is that it can provide measurement of both electron

density and ion composition along the geomagnetic field lines. Measurement of ion composition is made possible by magnetospheric reflection of WM waves at f~f_{lh}, where f is the wave frequency and f_{lh} is the lower hybrid frequency that depends on the ion composition.

1.3 Motivation and objectives

Whistler mode sounding in space by the Imager for Magnetopause-to-Aurora Global Exploration/Radio Plasma Imager (IMAGE/RPI) satellite has fulfilled unrealized goals of space science for many years. It has provided the distribution of plasma along geomagnetic field lines and studied large and small scale plasma density structures and their influence on the propagation of WM waves. The IMAGE/RPI operates in the radio frequency band 3 kHz to 3 MHz, which excites several wave propagation modes. Compared to ground based WM experiments, the WM waves in the topside sounding can be injected to cover a large region inside Earth's magnetosphere with a wide range of wave normal angles. WM sounding of the magnetosphere from space has several advantages over free space R-X, L-O, and Z-mode sounding from space. In particular, WM sounding provides (1) measurement of both electron density and ion composition along the geomagnetic field line **B**, and (2) measurement of field aligned irregularities (FAIs) over a wide range of scale lengths (10 m -100 km) (Sonwalkar et al., 2001, 2004, Sonwalkar 2006). The magnetospherically reflected whistler mode (MRWM) echoes, which get reflected at an altitude where the wave frequency is nearly equal to the local lower hybrid frequency, can provide ion composition/effective ion mass along Earth's magnetic field lines from the satellite altitude up to the reflection altitude. The specularly reflected whistler mode echoes (SRWM) that get reflected at the Earth-ionosphere boundary can provide the electron density distribution along Earth's magnetic field lines from satellite altitude up to the Earth-ionosphere boundary.

The main objectives of this dissertation are:

- Survey in detail of all kinds of WM echoes observed on IMAGE/RPI during the years 2000-2005.

- Derive electron and ion density distribution profiles along the Earth's magnetic field lines from whistler mode (WM) sounding on the IMAGE/RPI satellite using the method developed by Sonwalkar et al., (2011b) to the observed cases inside the plasmasphere, covering a wide range of L-shells, magnetic local times (MLTs), and different geomagnetic and solar conditions.

- Compare these results with in-situ measurements from other satellite data, bottom side sounding data, and empirical models.

1.4 Problem statement and approach

The radio Plasma Imager (RPI) on the IMAGE satellite provided the first opportunity for space based WM sounding of the magnetosphere (Reinisch et al., 2000; Sonwalkar et al., 2001, 2004). At altitudes below 5000 km, IMAGE/RPI has observed a variety of WM echoes up to ~300 kHz during the period 2000-2005. The time delay of these echoes is directly related to the reflection conditions and the properties of the plasma along the ray path. Plasma density profiles can be estimated by studying the time delays of these echoes. MRWM echoes can provide ion composition and electron density distribution while SRWM echoes can provide an electron density distribution profile up to the Earth-ionosphere boundary. This dissertation provides new measurements of electron density and ion composition over a wide range of L-shells from MRWM, SRWM echo characteristics. Two dimensional ray tracing simulations are performed in a smooth magnetosphere to calculate the WM echo frequency-time delay dispersion and cut-off frequencies. A part of this research work has been presented in Hazra and Sonwalkar (2011) and Hazra et al., (2012).

1.5 Organization of this dissertation

This dissertation work is organized into five chapters.

- Chapter One (current chapter) presents the motivation and objectives of this research work and introduces Earth's ionosphere and plasmasphere, WM wave mode, scientific background, and past work.

- Chapter Two describes the IMAGE/RPI satellite, WM data surveys, different types of WM echoes observed on IMAGE/RPI, and statistical analysis of these echoes at different geophysical and solar conditions.

- Chapter Three describes the method to find electron and ion density distributions along Earth's magnetic field lines from the WM echoes on IMAGE/RPI using Stanford 2D raytracing simulation, space plasma modeling, and comparison with other sources of data.

- Chapter Four describes the electron and ion density distribution covering L-shells 1.6 to 4 from 82 cases of WM echoes observed on IMAGE/RPI along different field lines, compared with

in-situ measurements from other satellites, bottom side sounding from different ionosonde stations, and empirical models.

- Chapter Five summarizes the results presented in the previous chapters, and concludes with a discussion of future extensions of this work, including suggestions for experimental validation.

1.6 Background and past research

The past work is reviewed on the basis of determination of plasma density, ion composition, and effective mass of ions of the plasmasphere, and the observations of IMAGE satellite below 5000 km related to plasmaspheric density measurements.

1.6.1 Electron density measurements of ionosphere/plasmasphere

Since 1950, people have been using rocket measurements, in situ probe measurements by satellites, spacecraft borne sounders, and measurements based on the wave propagation method to construct the vertical electron density profile beyond the F layer of the ionosphere (Calvert et al., 1964; Calvert, 1966; Thomas and Sader, 1964). In 1964, the Explorer 22 satellite was launched with a circular orbit of 1000 km to measure the global distribution of electron density. These measurements were in good agreement with the diffusive equilibrium model of electron density distribution for day and night (Brace et al., 1967; Miller and Brace, 1969; Reddy et al., 1969). The Alouette-1 (launched in 1962; 1000 km), and -2 (launched in 1965; 500-3000 km) and ISIS-1 (launched in 1969; 550-3500 km), and -2 (launched in 1971; 1400 km) satellites were equipped with topside sounder instruments to monitor the topside ionosphere from the satellite orbit altitude down to the F-peak. They have returned a wealth of global information on electron density distributions (Benson, 2010; Jackson et al., 1980). A software algorithm (TOPIST) was developed for automated scaling and inversion of ionograms of the Alouette and ISIS satellites, which provided Ne data from the F2 peak up to satellite altitude (Bilitza et al., 2004; Huang et al., 2002). The topside electron density model part of the standard ionospheric parameter empirical model, the IRI (International Reference Ionosphere), uses Alouette and ISIS data (Bilitza et al., 2004, 2006; Bilitza and Reinisch, 2008; Coisson et al., 2009). Nsumei et al., (2012) have introduced a new Vary-Chap function profile of the topside ionospheric electron density for use with the IRI model. In an IM-6 radio astronomy experiment, Mosier et al., (1973) reported the observation of a noise band between the local Upper Hybrid Resonance (UHR) frequency and the electron plasma frequency (f_{pe}), extending down to

the local plasma cut-off frequency. The S3-3 satellite launched in 1976 with an elliptical orbit (240 km perigee and 8000 km apogee) made in-situ measurements and the indirect measurements of electron density from upper hybrid resonance (UHR) frequency (Mozer et al., 1979). Persoon et al., (1983, 1988) measured electron density from the observed upper cut-off of whistler mode (WM) waves at the electron plasma frequency observed in the DE 1 spacecraft data up in the altitude range $1.09R_e$ to $4.4R_e$.

WM waves have become a very powerful tool for probing the ionosphere and plasmasphere. The electron density is determined from WM echoes based on the travel times. Travel time is proportional to the integral of the square root of electron density along the ray path (Carpenter, 1963b, 1988; Carpenter and Smith 1964; Helliwell 1965; Helliwell and Brice 1964; Scarf and Chappell 1973, Walker 1976). Carpenter et al., (1981) compared the equatorial electron density from whistler data in Siple, Antarctica (L = 4.2) with ISEE-1 satellite data in the region 3<L<5.2. This comparison showed good agreement and also supported the diffusive equilibrium model for plasmaspheric density. Sawada et al., (1993) also found the global electron density distribution in the plasmasphere with the help of in-situ measurements of electron density along the trajectory of the Akebono (EXOS D) satellite and the wave normal direction of OMEGA signals simultaneously observed by the same spacecraft. The Langmuir probe carried by the low altitude circular orbit satellites DMSP (850 km), and CHAMP (350 km) has provided in-situ measurements of electron density covering a wide range of solar and geomagnetic activities (Luhr and Xiong, 2010; Liu et al., 2007; Fallen et al., 2011; Migoya-Orue et al., 2013). Carpenter and Anderson (1992) built an empirical electron density model covering the range 2.25<L<8 based on ISEE satellite data. This empirical model estimates the position of the plasmapause, which depends on K_{pmax} (maximum value of K_p index in a day). The other empirical models for the plasmapause have been developed using in-situ measurements from the IMP-2, DE-1, and CRRES satellites (Binsack, 1967; Horwitz et al., 1990; Moldwin et al., 2002, O'Brien and Moldwin, 2003). The Global Core Plasma Model (GCPM), developed by Gallagher et al., (2000), provides empirically derived core plasma density as a function of geomagnetic and solar conditions throughout the inner magnetosphere. It is composed of separate models for the ionosphere, plasmasphere, plasmapause trough, and polar cap. Kakinami et al., (2008) found an empirical model for electron density from Japanese Hinotori satellite data for the equatorial region at an altitude of 600 km during the solar maxima period.

1.6.2 Ion composition in the topside ionosphere/plasmasphere

Measurement of the ionic composition of the upper atmosphere started with the Sputnik 3 satellite in 1958 (Istomin, 1961). The Ariel 1 satellite, launched in 1962, carried an ion mass spectrometer and provided information about major ionic constituents of the ionosphere. Johnson (1966) reported the ionospheric composition and density from 90 to 1200 km during solar minima. The bottomside compositions were made by various rocket measurements and the topsides are from the Soviet satellite Electron 2. The OGO, ISIS, AE, DE1, and DMSP satellites carried Retarding Potential Analyzers (RPAs), which have provided a wealth of information regarding ion composition and its variation in the topside ionosphere and plasmasphere. The major ionic constituents in the plasmasphere are O^+ and H^+, and the minor constituents are N^+ and He^+. Heavy ions (O^+, N^+) have greater densities at noon than at midnight for a given season and in summer than in winter for a given local time. The lighter ion (H^+, He^+) densities are greater at midnight than noon and generally greater in the winter than summer. (Craven et al., 1995; Brinton et al., 1969; Breg and Hoffman, 1975; Hoffman et al., 1974). Statistical studies from DE1 satellite showed that the observed He^+ to H^+ ratios decrease with altitude and the decrease is at $\sim 1R_e$ and $4.5R_e$. The variation of the ratio with solar cycle is significant, about a factor 5 or greater for higher activity than low (Craven et al., 1997). Heavy ion concentration at mid latitudes increases during the main phase of a geomagnetic storm. The source of these ions is the ionosphere. During storms, particle precipitation intensifies and expands toward lower latitudes, heating the atmosphere and producing a large backsplash of energetic neutral oxygen, increasing heavy ion outflows (Torr et al., 1974). These enhanced O^+ fluxes should be observed in the plasmasphere and ring current populations (Berube et al., 2005). The MICS (Magnetospheric Ion Composition Spectrometer) on the CRESS satellite has shown an increase of O^+ ions and a decrease of H^+ ions during storm time in the range $L = 3$ to 6. Indeed, greatly increased concentrations of O^+ have been observed in the ring current (Hamilton et al., 1988). Techniques also exist for remotely sensing the mass density along closed magnetic field lines which involve using pairs of ground-based magnetometers to measure field line resonance frequencies (also referred to as eigenfrequencies) (Schulz, 1996; Denton and Gallagher, 2000; Denton et al., 2006). These measurements agree well with other satellite measurements (Berube et al., 2005).

Another two important parameters related to ion density measurements are effective ion mass (m_{eff}) and transition heights (height at which lighter and heavier ion densities are equal). Bar-

rington et al., 1965 have determined the m_{eff} from the lower cut-off of the VLF noise band (lower hybrid resonance). m_{eff} is found to be larger during the day than at night and increases with latitude. The O^+/H^+ transition height is a sensitive indicator of solar EUV ionizing flux and the dynamics of the topside ionosphere (MacPherson et al., 1998). Data from the CNOFS satellite have shown that during solar minima, the O^+/H^+ transition height is ~850 km, and at night, it is ~450 km (Heelis et al., 2009; Tulasi Ram et al., 2010). He^+/O^+ is ~1 order of magnitude lower than H^+/O^+ during the solar minimum and ~0.5 order of magnitude lower at nighttime. A higher He^+/O^+ ratio indicates a lower O^+/He^+ transition altitude compared to the O^+/H^+ transition altitude (Borgohain and Bhuyan, 2010). Truhlik et al., (2005) have reported that He^+ ions increase with solar activity. Under high solar activity, above 1000 km, the amounts of O^+, H^+, and He^+ may sometimes be equal. Data from incoherent scatter radar measurements at the Arecibo observatory (18.35°N, 66.75°W) and the COSMIC satellites during solar minima show similar results (Aponte et al., 2013; Yue et al., 2010). Marinov et al., (2004) have developed an empirical model for O^+/H^+ transition height from topside sounding data of the Alouette satellite covering low to high solar activity. Results show that the altitude distribution is covered in the range of 400 km to 1200 km.

Based on ion density data from different satellites and other sources, a number of physics-based and empirical models have been proposed for ion densities. The Ion Density Calculator (IDC) model is a computationally efficient and accurate model of ion concentrations in the bottomside ionosphere and is based on photochemistry. This model uses iterative techniques to solve for the O^+ density given the electron density provided by the radar or the IRI model and the fact that the total ion concentration must sum to the electron density (Richards et al., 2010). This model is also used for ion composition in bottomside ionosphere for the IRI-2012 model. Rich and Sultan (2000) have compared ion densities from the DMSP with those from the IRI, Parameterized Ionospheric Model (PIM), and the Reilley ICED- Bent Gallagher (RIBG) model. Results showed that all of the models reproduce some of the features of the observed topside ionosphere but none of the models match all of the observations. Kohlein (1989) found an empirical model of atomic ion densities (H^+, He^+, N^+, O^+) up to 4000 km altitude as a function of time (diurnal, annual), altitude, and solar flux using the observations from the AE, ISIS-2, and OGO-6 satellites and rockets during quiet geophysical conditions. Guiter et al., (1995) proposed a two ion (H^+, O^+) empirical model based on DE1 data, this model is fully interhemispheric and diffusive equilibrium is not assumed. Triskova et al., (2003, 2006) presented an empirical model for relative densities of the four main

plasma components (H^+, He^+, N^+, O^+) based on AE and Intercosmos 24 satellite data in the altitude range 500 km to 2500 km. This model is also a part of ion composition for the IRI-2012 model in the topside ionosphere.

1.6.3 Electron and ion density measurements by IMAGE

The launch of IMAGE in the year 2000 has added to the knowledge of density structure of the magnetosphere, as it is the first satellite to provide plasma density along the magnetic field line based on radio sounding techniques. The IMAGE satellite mission has provided innovative techniques and local and non-local views of the global plasmasphere related to various density structures and their dynamics, as well as plasma wave research and empirical models for densities (Darrouzet et al., 2009; Masson et al., 2009; Matsui et al., 2009; Keyser et al., 2009; Reinisch et al., 2009). The RPI instrument in IMAGE operated sounding in free space LO mode, free space RX mode, Z-mode (ZM), and for the first time, the WM in space, providing a significant method to measure electron and ion density of the magnetosphere (Benson et al., 2003; Reinisch et al., 2000; Sonwalkar et al., 2001, 2004). Plasmaspheric densities were measured from IMAGE data in response to solar wind and geomagnetic activity in middle and high latitudes (Berube et al., 2005; Green and Reinisch, 2003; Nsumei et al., 2003, 2008; Tu et al., 2004, 2005, 2007). The EUV instrument of the IMAGE satellite can extract the He^+ edge of the plasmasphere and identify the plasmapause with the help of steep in situ density gradients measured by IMAGE/RPI (Sandel et al., 2001; Goldstein et al., 2003). Cross-phase derived mass densities have been compared to electron densities derived from both RPI and ground-based VLF receiver measurements. The results are in excellent agreement (Dent et al., 2003). Denton et al., (2006) constructed a realistic density model for the magnetosphere based on the two dimensional image of the magnetosphere from IMAGE/EUV, in-situ measurements of electron density from IMAGE/RPI, and measurements of magnetospheric mass density obtained from field line resonant frequencies measured by the magnetometers on Earth's ground. The equatorial plasma density and composition at L = 2.5 were studied during an extended disturbed interval using field line resonance measurements (yielding plasma mass density), naturally and artificially stimulated VLF whistlers (electron number density), and IMAGE/EUV observations for plasmapause position and line-of-sight He^+ intensity. The results showed the O^+ concentration exceeded 50%, indicative of the formation of an oxygen torus (Grew et al., 2007). Denton et al., (2012) reported measurements of electron density refilling rates in L-shell 2 to 9 from passive radio emissions by the IMAGE/RPI satellite. Reinisch et al., (2004) and Tu et al.,

(2006) developed empirical event models using RPI radio sounding data. In both studies, a density profile of L^{-4} in the magnetic equatorial plane reasonably describes the density distribution over the L-shell range of observations (1.6<L<7) in both the plasmasphere and the trough. Webb et al., (2007) created a database of electron density measurements from passive plasma wave data of IMAGE. Sonwalkar et al., (2004) calculated the electron density profile below 5000 km along the geomagnetic field line from time delay measurements of WM and Z-mode echoes observed on IMAGE/RPI. The study of MR echoes observed by IMAGE/RPI can provide measurements of ion densities along the field line both above and below the satellite altitude (Sonwalkar et al., 2011b). Sonwalkar et al., (2011b) illustrated a new satellite-based method of sounding electron density, ion composition, and FAIs from the WM echoes observed on IMAGE/RPI. Ozhogin et al., (2012) developed an empirical model of the plasma density of the plasmasphere based on more than 700 density profiles along the field line derived from active sounding measurements made by IMAGE/RPI covering L-shells 1.6 to 4 using measurements of the electron density from passive radio wave observations by the IMAGE/RPI on consecutive passes through the magnetosphere.

Chapter 2 Experiment description and data analysis

2.1 Experiment setup

2.1.1 The IMAGE satellite orbit

The Imager for Magnetopause-to-Aurora Global Exploration (IMAGE) mission was launched from Vandenberg AFB on 25 March 2000 at 20:34:43 UT. It was the first satellite mission dedicated to imaging the Earth's magnetosphere, the region of space controlled by the Earth's magnetic field that contains extremely tenuous plasmas of both solar and terrestrial origin. IMAGE employed a variety of imaging techniques to 'see the invisible' and to produce the first comprehensive global images of the plasma populations in the inner magnetosphere. It measured, in a way never before possible, large-scale dynamics of the magnetosphere and the interactions among its constituent plasma populations (Burch, 2000; Reinisch et al., 2000).

At the time of launching, IMAGE had an initial perigee altitude of 1000 km in the southern hemisphere and an apogee altitude of $7.2R_e$ ($\sim$45921 km) with an apogee inclination of $40°$ in the northern hemisphere. The satellite travels around the Earth with a 14.2-hour orbital period at different speeds at different positions along its orbit. When the satellite is closer to the Earth, near perigee, its speed is much higher than when it is farther away, near apogee, like any Keplerian orbit. The spacecraft has a spin period of two minutes with the spin axis perpendicular to the orbital plane. The region of interest in this research is the low altitude ($<2R_e$) region in the northern hemisphere.

Figure 2.1 shows a plot of the IMAGE satellite orbit in the geomagnetic coordinate system in the month of May for the years 2000 to 2005. The tick marks (e.g, May, 2005 orbit) indicate the IMAGE satellite location every 30 minutes. The IMAGE satellite orbit precesses by about $40°$ a year, allowing the satellite to probe a range of locations in the magnetosphere. The satellite had a lower perigee altitude ($\sim$600 km) in 2003 and higher perigee altitudes ($\sim$1700 km) in 2001 and 2005.
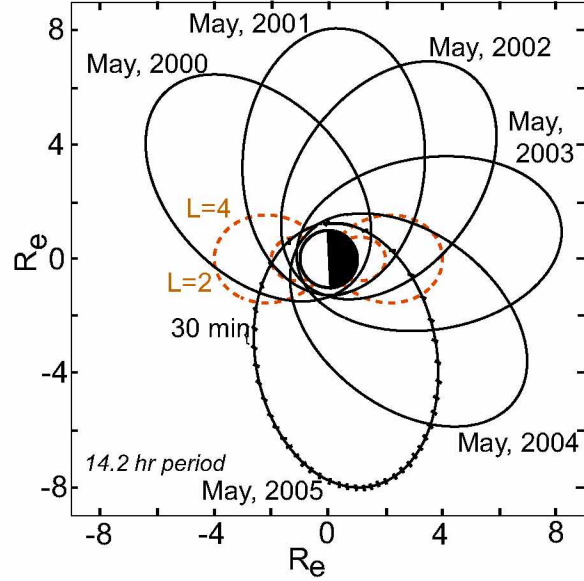
Figure 2.1 The IMAGE satellite orbit. Figure shows the IMAGE satellite orbit precession between the years 2000 and 2005 in the geomagnetic coordinate system. The tick marks indicate IMAGE satellite location every 30 minutes. The orbit precesses 40° in a year allowing the satellite to probe a range of locations in the magnetosphere.

2.1.2 Radio Plasma Imager (RPI)

The Radio Plasma Imager (RPI) on the IMAGE satellite is a highly flexible, multi-mode instrument in which sounding and listening frequencies, range detection, pulse characteristics, and repetition rate are adjustable parameters over a wide range of values. The flexibility in programming the RPI allows the instrument to sound magnetospheric boundaries remotely, perform local relaxation sounding, and observe natural emissions over a selectable duty cycle. The instrument covers the frequency range from 3 kHz to 3 MHz with a receiver bandwidth of 300 Hz. (Burch, 2000; Reinisch et al., 2000, 2001). There are three orthogonal thin-wire antennas, two of them are of 500 m length (X-, Y-antennas; tip to tip dipoles in the spin plane), another one is of 20 m length (Z-antenna; tip to tip dipole along the spin axis). The long dipoles are used for transmission, and all three antennas are used for reception. The nominal radiated power from RPI, variable (in terms of free space mode excitation) from 0.1 mW at low frequencies to 10 W per dipole at 200 kHz, was reduced by 3 dB on 8 May 2000 when the power supply for the y-axis transmitter failed. The dipole length of the X-antenna was reduced to 340 m on 3 October 2000, when one of the x-axis monopoles was partially severed, apparently by a micrometeorite. On 18 September 2001 an unknown (small and negligible) section of the Y-antenna was lost. On 30 September 2004, as a result of an unknown failure of the Y antenna/receiver system, the signal strength received by

the Y-antenna was reduced substantially (Carpenter et. al 2003, 2007, Sonwalkar et al., 2011a). The failure of the Y-antenna/receiver system in September 2004 made the detection of diffuse MR echoes (as observed on X-antenna) in discrete form and thus provided an unexpected advantage. During 5.8 years lifetime of the IMAGE satellite mission, RPI supplied good variety of WM echoes at different geophysical locations. IMAGE mission was ended on 18 December, 2005 due to failure of power distribution unit. More information about the IMAGE satellite and its data can be found at http://image.gsfc.nasa.gov/

The programs in the RPI can be classified into two groups by the operating mode: one is the active sounding experiment, in which the RPI transmits signals and detects the echoes returning to the satellite, another is passive recording, where it only records all the background signals. This experiment is schematically shown in figure 2.2.
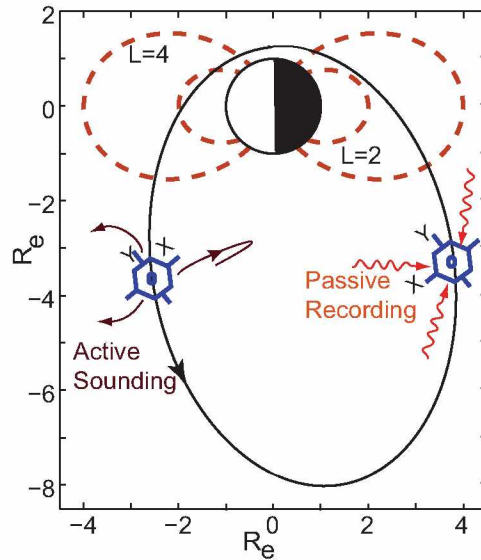
Figure 2.2 Schematic showing the RPI active sounding and passive recording.
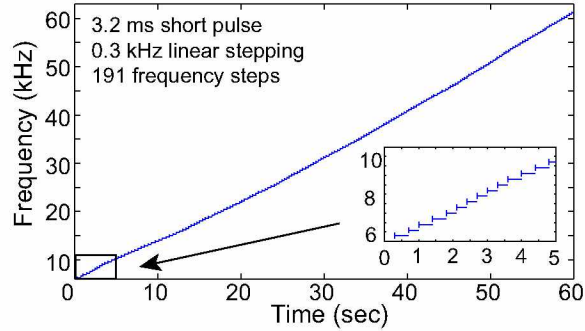
Figure 2.3 An example of program format used in RPI sounding experiment. Frequency and time step of transmitted signal in the sounding program number 38. The inset shows the details of the program. The vertical line at the beginning of each horizontal line represents 3.2 ms duration transmitted pulse at that frequency. The length of the horizontal line represents the waiting period during which RPI listens to the echoes (adapted from Li, 2004).

2.1.3 Pictorial RPI data representation of data on BinBrowser

BinBrowser is a browsing tool for the RPI database query system developed by the University of Massachusetts Lowell. A detailed description of this software is provided in Galkin (2004) and Li (2004). This software is available for free at http://ulcar.uml.edu/Installation/BinBrowser/install.htm. In BinBrowser, the measurement of active sounding data is shown by a plasmagram and the passive recording is shown by a dynamic spectrogram.

2.1.4 Plasmagram

In a plasmagram, the virtual range of echoes in Earth radii as a function of sounding frequency are shown. Virtual range is calculated from the measured time delay, assuming that the signal has propagated at the velocity of light in free space. For convenience, the plasmagrams discussed later are in the format of time delay versus frequency. The color bar, on the right in figure 2.4, shows the amplitude of the electrical field in dBnV/m. This electrical field is calculated by dividing the measured amplitude of voltage on the antenna by the antenna's effective length. The antenna's effective length is considered to be half of its physical length that makes the effective length for the X-, Y-, and Z- antennas as 250 m, 250 m, and 10 m respectively. Figure 2.3 shows the frequency step vs time step of program number 38 transmitted by the RPI. This program has 0.3 kHz of linear stepping of 191 frequency steps in the range 6-63 kHz with pulse width of 3.2 ms. For this reason, each frequency bin has ± 0.15 kHz of uncertainty. Each time delay measurement bin (virtual range/c) has 3.2 ms of uncertainty. Figure 2.4 shows an example of the magnetospherically reflected (6.6-9.3 kHz) and specularly reflected (10.2-33.3 kHz) WM echoes. A detailed explanation of those

16

types of echoes are discussed in the later part of this chapter.
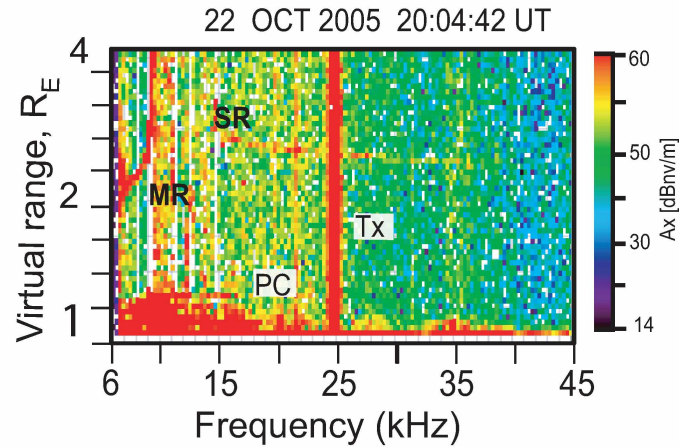
Figure 2.4 Plasmagram. The x axis of a plasmagram is the frequency in kHz; the y axis is the virtual range in R_e. The color bar on the right shows the amplitude of electric field in dBnV/m. The observed magnetospherically reflected (MR), specularly reflected (SR) whistler mode (WM), proton-cyclotron (PC) echoes, and transmitter signals (Tx) are shown.

2.1.5   Dynamic spectrogram
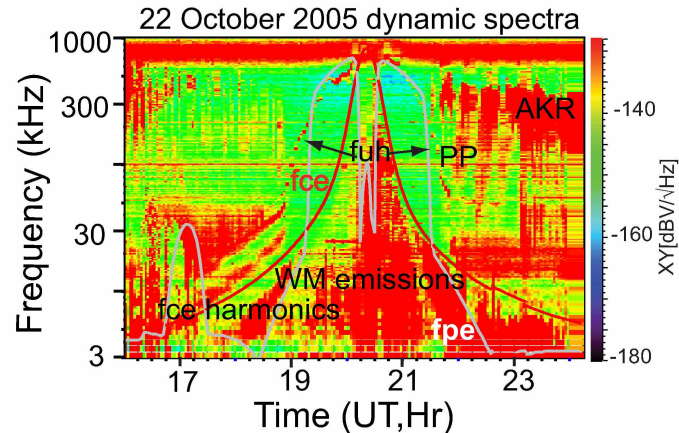
Figure 2.5 Dynamic Spectrogram. The x axis of a dynamic spectrogram is time in UT, y axis is the frequency. The color bar on the right shows the amplitude of voltage in $dBV/\sqrt{Hz}$. Signals from ground transmitters, upper hybrid emissions, plasmapause, and gyro frequency harmonics are shown.

An RPI dynamic spectrogram displays frequency versus time of the passive measurements (thermal noise) made by program number 23 (pr#23) and pr#26. An example of a dynamic spectra is shown in Figure 2.5. The thermal noise energy in dynamic spectra is collected over the receiver bandwidth of 300 Hz is normalized to 1 Hz, which corresponds to $1/\sqrt{300}$ factor in voltage. The color bar on

the right shows the amplitude of the voltages measured on the RPI antennas in $dBV/\sqrt{Hz}$, which is the voltage divided by square root of the 300 Hz bandwidth. Finally, the value is plotted on a decibel (dB) scale. The solid red curve indicates the gyro frequency calculated by the IGRF2000 model for internal magnetic field and the T96 model for the external magnetic field (Tsyganenko and Stern, 1996). Whistler mode signals from various ground transmitters in 10 to 30 kHz are frequently observed when the satellite travels from the pole to the equatorial region in the northern hemisphere. These signals appear as slim horizontal lines in the dynamic spectrogram. The harmonics of the gyro frequency, which is usually found close to the plasmapause (where the upper hybrid emission band drops suddenly, varying the electron density by two orders of magnitude (Sonwalkar et al., 1995), can be used to estimate the electron gyro frequency. The other natural emissions generally seen on the dynamic spectrogram are WM emissions and auroral kilometric radiation (AKR).

2.1.6 Electron plasma frequency (f_{pe}) measurements from upper hybrid emissions (f_{uh}) of the dynamic spectra
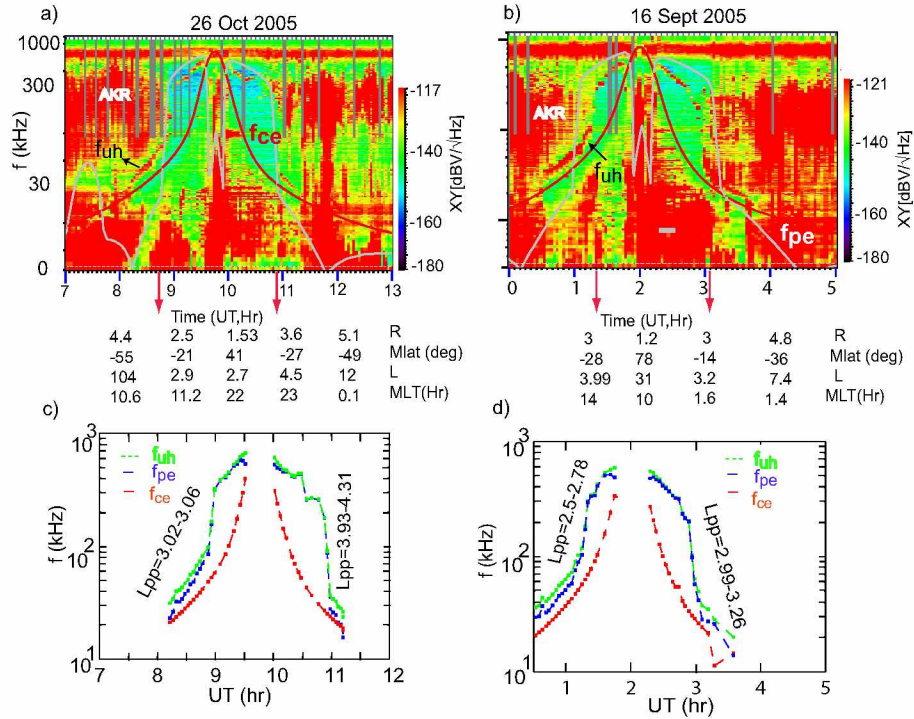
Figure 2.6 f_{pe} measurements from f_{uh} of the dynamic spectra. Top panels show the RPI dynamic spectrograms on 26 Oct 2005, 16 Sept 2005 with the upper hybrid frequency, f_{uh}, AKR, WM emissions, model f_{pe} (white), model f_{ce} (red). Bottom panels show the plasma characteristic density profiles extracted from the RPI dynamic spectrograms of 26 Oct 2005 and 16 Sept 2005.

The upper hybrid frequency (f_{uh}) is a combination of the electron cyclotron frequency, f_{ce}, and the electron plasma frequency, f_{pe}

$$f_{uh} = \sqrt{f_{pe}^2 + f_{ce}^2} \qquad (2.1)$$

The electron cyclotron frequency is a function of the magnetic field strength, B,

$$f_{ce} = \frac{|e|B}{2\pi m_e} \qquad (2.2)$$

the electron plasma frequency is a function of the electron number density, Ne,

$$f_{pe} = \frac{1}{2\pi} \left(\frac{N_e e^2}{m_e \epsilon_o} \right) \qquad (2.3)$$

and the electron number density (N_e) can be written in terms of f_{pe} as

$$N_e = \frac{4\pi^2 m_e \epsilon_o f_{pe}^2}{e^2} \qquad (2.4)$$

Here e is the charge of the electron, m_e is the mass of an electron, and ϵ_o is the permittivity of free space. The upper limit of the noise band at f_{uh} is usually the most pronounced cut-off in the RPI data. The two examples of dynamic spectra shown in the upper panel of Figure 2.6 show f_{uh} emissions, AKR, and WM emissions. The upper cut-off of the f_{uh} is identified and Ne is determined using equation 2.4 and the cyclotron frequency (f_{ce}) inferred from the IGRF model for magnetic field (equation 2.2). The bottom panel Figure 2.6c and d show the corresponding upper cut-off of f_{uh} measurements (green), f_{ce} from IGRF model (red), and (f_{pe}) (blue) calculated using equation 2.1. Under the condition of $f_{pe}/f_{ce} \gg 1$, f_{uh} is approximately the same as f_{pe}. In the dynamic spectra of 2.6a the day side plasmapause is measured from the drop in f_{uh} emissions in the time interval 08:55:27 to 08:59:10 UT (shown with red arrow in 2.6a when f_{uh} changes from 325 kHz to 174 kHz. It shows typical plasmapause features such as Ne dropping from 1268/cc to 342/cc, about a factor of 4 over the L-shell range 3.02 to 3.06. In the night side of this dynamic spectrogram the plasmapause is measured from the drop in f_{uh} emissions in the time interval 10:49:22 UT to 10:55:23 UT when the f_{uh} changes from 234 kHz to 50 kHz (Ne dropped from 668/cc to 23/cc, about a factor of 20 over the L-shell range 3.93 to 4.31). Similarly, for the 16 September 2005 dynamic spectra the day side plasmapause is measured from the drop in f_{uh} emissions in the time interval 01:19:50 UT to 01:14:34 UT when the f_{uh} changes from 304 kHz to 121 kHz (Ne dropped from 1089/cc to 141/cc, about a factor of 10 over the L-shell range 2.5 to 2.78). At night side plasmapause is measured from the drop in f_{uh} emissions in the time interval 02:53:26 UT to 02:58:59 UT when the

f_{uh} changes from 192 kHz to 65 kHz (Ne dropped from 443/cc to 41/cc, about a factor of 10 over the L-shell range 2.99 to 3.26).

2.2 List of Whistler mode programs transmitted on IMAGE/RPI

Table 2.1 lists details of the programs transmitted in the WM frequency range during the years 2000 to 2005.

Table 2.1 List of details of programs transmitted in WM frequency range during the years 2000 to 2005. LTD is Linear Time Domain Data; DBD is Double Byte Data; SMD is Spectral Maximum Data.

Program	f(kHz)	Format	Year	Echo type
5	60 to 1000	LTD; (0-7)R_e; 3.2 ms pulse; Duration: 74 sec step: 2% logarithmic; 144 frequency steps	2001, 2002, 2003, 2004, 2005	single, double SR
20	6 to 65	LTD; (0-3)R_e; 3.2 ms pulse; Duration:64 sec step: 0.3 kHz linear; 227 frequency steps	2003	Diffuse SR >60 deg
21	15 to 500	LTD; (0-4)R_e; 3.2 ms pulse; Duration:79 sec, step: 2% logarithmic; 179 frequency steps	2002, 2003	Diffuse SR >60 deg
29	3 to 3000	DBD; (0-7)R_e; 3.2 ms pulse; Duration:202 sec 178 frequency steps; step:4% logarithmic	2000	MR and single SR
38	6 to 63	LTD; (0-4)R_e; 3.2 ms pulse; Duration:60 sec step: 0.3 kHz linear; 191frequency steps	2003, 2004, 2005	MR, single and double SR
43	10 to 150	LTD; (0-2)R_e; 3.2 ms pulse; Duration:27 sec, step: 10% logarithmic; 30 frequency steps	2000	single SR
43	50 to 900	LTD; (0-7)R_e; 3.2 ms pulse; Duration:73 sec, step: 2% logarithmic; 147 frequency steps	2003	single SR
56	50 to 1000	LTD; (0-4)R_e; 3.2 ms pulse; Duration:52 sec, step: 2% logarithmic; 153 frequency steps	2003, 2004	single and double SR
57	20 to 326	LTD; (0-4)R_e; 3.2 ms pulse; Duration:82 sec, linear 1.2 kHz step; 256 frequency steps	2003, 2004, 2005	single and double SR
61	10 to 1800	SMD; (0-4)R_e; 8 chip complimentary, 40 frequency steps; Duration: 109 sec, 8 pulse per frequency	2000	single SR

Table 2.2 Number/types of WM echoes observed corresponding to the number of transmissions during year 2000-2005.

Year	No. of WM transmissions	Types/no. of WM echoes
2000	1061	MR=14, SR=44, MR+SR=0, Double SR=0
2001	178	MR=No, SR=18, Double SR=0
2002	4818	MR=5, SR=596, MR+SR=0, Double SR=2
2003	4160	MR=10, SR=579, MR+SR=5, Double SR=10
2004	5980	MR=13, SR=557, MR+SR=3, Double SR=11
2005	4415	MR=389, SR=712, MR+SR=142, Double SR=3
Total	20613	MR=431, SR=2506, MR+SR=150, Double SR=28

Relatively few MR echoes observed in the years 2000-2004, as more than 2000 numbers of pr#38 (suitable frequency range (6-63 kHz) for MR echo) were transmitted in the year 2005.

In the year 2005, WM echoes were observed on ∼25% of the transmissions (highest numbers of pr#38 transmissions in year 2005; 2040 transmissions. During the years 2000 to 2004 WM echoes were observed on ∼10% of the total transmissions. The efficiency of the antennas drops steeply with decreasing frequency below 100 kHz from a maximum near 200-300 kHz (Reinisch et al., 2000; Sonwalkar et al., 2004).

2.2.1 Calculated $f_{lh,sat}$ and measured $f_{lh,sat}$ on plasmagram

The lower hybrid resonance (LHR) emissions arise due to a resonance between electromagnetic wave and ambient plasma in the vicinity of satellite location. Therefore, it is a function of the location of the satellite. The frequency of LHR emissions lies below electron plasma frequency. Figure 2.7a and 2.7b show $f_{lh,sat}$ (lower hybrid resonance frequency at satellite location) measured (blue lines) from the plasmagrams and calculated from measured f_{pe} (electron plasma frequency from upper hybrid emissions of the dynamic spectra and electron cyclotron frequency from the IGRF model using equation 3.22) and taking effective ion mass as 1 (red dots). Figure 2.7a is for the day side cases and Figure 2.7b is for the night side cases. In most of the cases, the f_{lh} resonance is observed in two bins. There are a few cases where the resonance is spread over three bins. The range of $f_{lh,sat}$ for all cases varies from 6.3 kHz to ∼10 kHz. This is because the location of the cases varies in L-shell from 1.6 to 4 and in altitude from ∼1800 km to ∼4000 km. For a number of cases, the calculated values of $f_{lh,sat}$ are lower than 6 kHz. For these cases, $f_{lh,sat}$ can not be measured as it is beyond the lower cut-off frequency of the plasmagram (6 kHz). This is mostly for the cases of

higher altitude ($\geq$3000 km) and lower L-shells ($\leq$2.2). In most of the cases, the calculated $f_{lh,sat}$ is within the measured $f_{lh,sat}$ range. For night side cases, the $f_{lh,sat}$ varies from ~6.9 kHz to 9 kHz. The calculated $f_{lh,sat}$ values also lie within this range. There are not many night side cases where $f_{lh,sat}$ can not be measured from plasmagrams for lower cut-off limitations due to the trajectory of the IMAGE satellite in night side for the months of August to December 2005 (no transmission of pr#38 in L-shell<1.9 range).
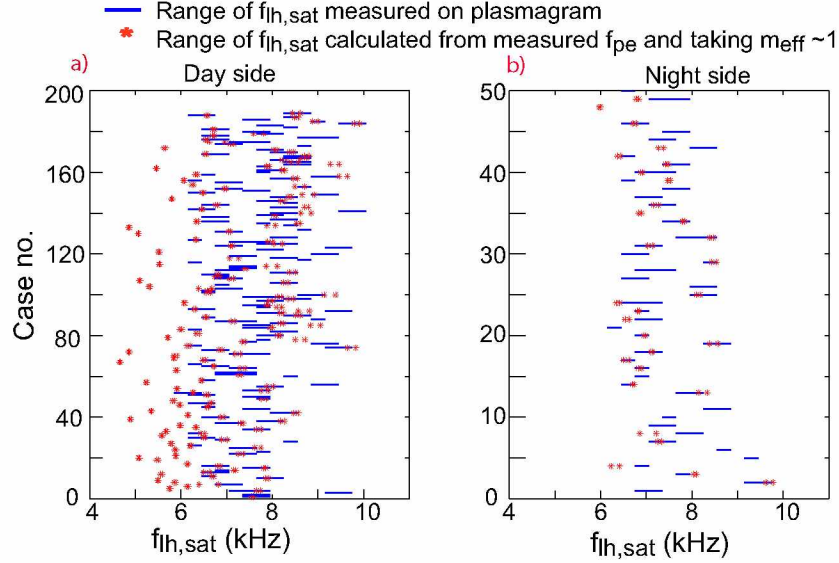
Figure 2.7 Measured and calculated lower hybrid frequency at satellite location. Range of $f_{lh,sat}$ (lower hybrid frequency) at satellite measured from the plasmagram (blue lines). Red dots are the ranges of $f_{lh,sat}$ at satellite location calculated from measured $f_{pe,sat}$ from dynamic spectra and taking m_{eff}=1 for all the case with MR echo. Figure a) is for the day side cases, Figure b) is for night side cases.

2.2.2 Measured $f_{pe,sat}$ from dynamic spectra and calculated from measured $f_{lh,sat}$ on plasmagram

The ranges of f_{pe} (electron plasma frequency) at satellite locations calculated from the measured f_{uh} (upper hybrid emission) on the dynamic spectra and f_{ce} (electron cyclotron frequency) from the IGRF model from Equation 2.1 (blue line, Figure 2.8). The red line represents range of f_{pe} at the satellite, calculated from $f_{lh,sat}$ (lower hybrid resonance) and taking effective ion mass as one (since the altitude of all these cases is above 1800 km). These ranges are comparatively longer than the measured ones (blue lines) because in most cases $f_{lh,sat}$ is spread over two bins and for a few cases it is observed for three bins. For most of the cases, the measured ranges lie within the calculated ranges. The measured f_{pe} goes from ~400 kHz to ~700 kHz for both day side and night

side. For most of the raytracing cases near L-shell 3 and greater, the f_{uh} emissions are not observed, hence, f_{pe} can not be measured for those cases. For the cases where $f_{lh,sat}$ is not observed f_{pe} can not be calculated. As seen from these figures, the measured/calculated $f_{pe,sat}$ does not show any dependence on day or night side because the cases are not plotted in terms of L-shell or altitudes.
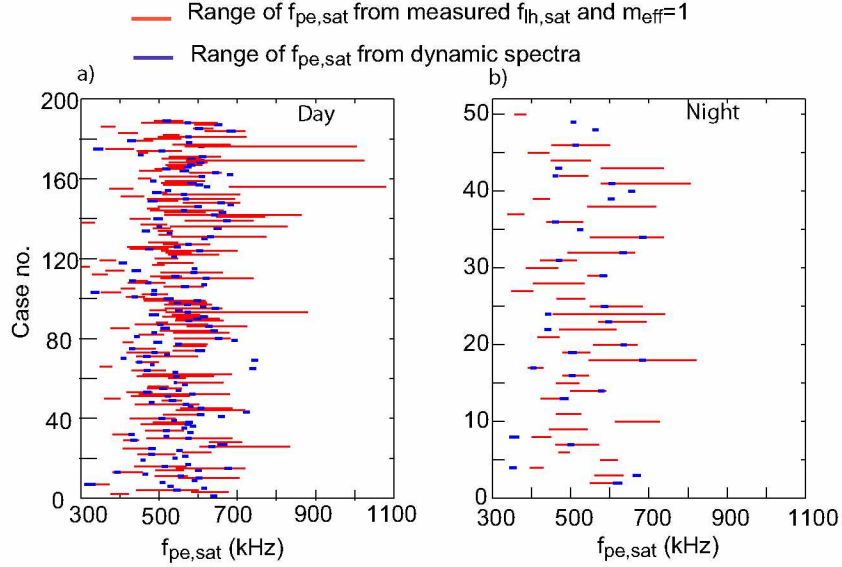
Figure 2.8 Measured and calculated plasma frequency at satellite location. Range of f_{pe} (electron plasma frequency) at satellite location calculated from measured f_{uh} emission at satellite location (blue lines), f_{ce} (electron cyclotron frequency) from IGRF model, red lines are the ranges of f_{pe} at satellite location calculated from measured $f_{lh,sat}$ and taking $m_{eff}=1$ for all the case with MR echo. Figure a) is for the day side cases, Figure b) is for night side cases.

2.3 Examples of WM echoes observed on IMAGE/RPI

As discussed before, there are two main types of WM echoes observed on IMAGE/RPI: MR and SR (OI-SR and NI-SR). In this section, examples of combinations of these echoes at different geophysical locations are shown. These examples show how the appearances of these echoes can be affected by different geophysical locations and conditions. These combinations of echoes at different locations and conditions can provide a wealth of information related to electron and ion density distributions along magnetic field lines.

2.3.1 Criteria for detecting WM echo on IMAGE/RPI plasmagrams

WM echoes are observed at frequencies lower than the local f_{pe} or f_{ce} (whichever is lower). In IMAGE/RPI, they are mostly observed below altitude 5000 km and below 300 kHz frequency. All the WM echoes on IMAGE/RPI presented in this thesis are detected manually. For a given case,

echoes on the plasmagrams of all the X-, Y-, and Z-antennas and combined amplitude representations are compared to get the proper cut-offs and time delay measurements. In many cases, the MR echo is diffused on the X-antenna but discrete on the Y-antenna due to the Y-antenna's breakdown (as discussed in Section 2.1.2). This gives proper cut-offs and time delay measurements on the Y-antenna. In all examples of echoes included here, the plasmagrams are shown with color bar representation, to reproduce the echo. The basic criteria for MR and SR echo detection are as follows.

MR echo:

1. MR echoes are observed in lower frequency range below 15 kHz. The best transmission program format on IMAGE/RPI for observing MR echoes is program#38 (6-63 kHz). The lower cut-off of the MR echo is the local f_{lh} resonance (referred to as $f_{lh,sat}$) which is observed mostly in one or two bins (sometimes three). Due to program transmission frequency limitations we do not always see the lower cut-off of the MR echoes. The upper cut-off of the MR echoes is always less than the local f_{lhmax1} (maximum lower hybrid frequency).

2. The time delay of the MR echoes increases with frequency. A sharp rise in time delay ($\sim$20-40 ms higher than the adjacent frequency bins) is observed near the upper cut-off frequency (two-three bins of frequency). Some of the MR echoes in the lower L-shells (L<2) and higher altitudes (>3000 km) are U shaped.

SR echo:

1. SR echoes are higher in frequency ranges than MR echoes. Most of them are observed with more than 20 kHz difference in frequency between upper and lower cut-offs. The lower cut-off of the OI-SR echo is 1-2 kHz higher than the upper cut-off of the MR echo observed simultaneously. So, they are lower than frequency $\sim$15 kHz. At the region near the lower cut-off frequency of the OI-SR, the time delay decreases very sharply (20-40 ms covering 4-5 frequency bins). We do not see all OI-SR echoes with the lower cut-off frequency due to scattering of the rays by field aligned irregularities (FAIs) .

2. The time delay of SR echoes (both OI and NI) decreases with frequency. The NI-echo can be observed overlapping with MR echoes, at a lower frequency (<15 kHz). Near the lower cut-off of the OI echo (<15 kHz), the echo has higher slope than the NI echo at same frequency. However, towards frequency >30 kHz, the NI echo has slightly higher slope than that of the OI echo.

3. Both the MR and OI-SR echoes propagate at higher wave normal angles (close to resonance cone angle) while the NI-SR echoes propagate at low wave normal angles. At low frequency, the

25

antenna power is low at lower wave normal angles, hence NI-SR rays get scattered by FAIs. This is one of the reason for not observing many NI-SR echoes at low frequency (overlapping with MR echoes). To distinguish the SR echo whether it is NI or OI at higher frequency (>60 kHz), raytracing simulations can be used to identify the OI- and NI-SR echoes. Chapter three describes the raytracing simulation code.

2.3.2 Example of MR echo observed simultaneously with OI-SR for IMAGE altitude above $R_{flhmax1}$ at mid latitude
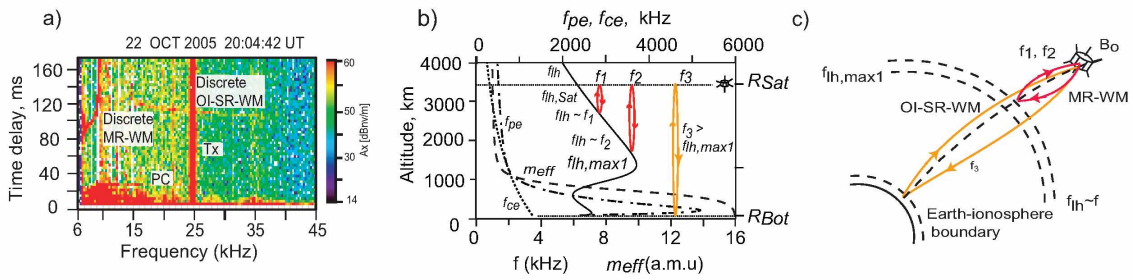
Figure 2.9 Simultaneous occurrence of MR and SR at mid latitude for IMAGE altitude above $R_{flhmax1}$
a) Discrete magnetospherically reflected (MR) and obliquely incident specularly reflected (OI-SR) whistler mode echoes received during the transmission of pr#38
b) Typical variation of plasma parameters f_{pe} (black dash-dot curve), f_{ce} (black dotted curve), f_{lh} (black solid curve), m_{eff} (black dashed curve), with altitude along the field line passing through the IMAGE satellite
(c) Schematic showing the formation of MR (red colored ray) by reflecting at altitude $f \sim f_{lhmax1}$ and OI-SR (gold colored ray) by reflecting at Earth-ionosphere boundary.

Figure 2.9a shows a typical example of an MR echo observed with OI-SR echo on the X-antenna on 22 October 2005 at L-shell 2.13, altitude 3400 km, $\lambda = 31.9°N$, and MLT = 11.2. We have reported this case in Sonwalkar et al., (2011a). This echo was observed well inside the plasmasphere (plasmapause L-shell $\sim$5.5). The plasma frequency (f_{pe}) estimated from the upper cut-off of the upper hybrid emission in passive recording ($f_{uh}\sim$666 kHz) f_{ce} (IGRF model) $\sim$321 kHz was $\sim$584 kHz (Benson et al., 2004). Both the MR and OI-SR echoes observed frequencies were much lower than the f_{ce} and f_{pe}, confirming the whistler mode character of their propagation. The altitude indicates that IMAGE was above f_{lhmax1} (altitude corresponding to maximum upper hybrid frequency f_{lhmax1}). The MR echo is seen from 6.3 kHz ($f_{MR,min}$) to 9.3 kHz ($f_{MR,max}$). The lower hybrid resonance ($f_{lh,sat}$; indicated by the arrow) appeared at $f_{MR,min}$. Generally, this resonance occupied 1-2 bins at $f_{MR,min}$. The $f_{MR,max}$ is generally 1-2 kHz lower than the maximum upper hybrid frequency (f_{lhmax1}) along the field line passing through the satellite. The echo at the upper cut-off generally

occupies 1-2 bins (0.3-0.6 Hz) of frequency. The lower frequency part of the MR echo occupies 2-3 bins of time delay. The time delay of the MR echo increases with frequency, with a sharp increase near the upper cut-off at 9.3 kHz. Assuming $m_{eff} \sim 1$, which is a good approximation for altitude ~ 3400 km, we can estimate f_{lh} as ~ 6.3 kHz, which is consistent with our statement that the lower cut-off of the MR echo is the local lower hybrid frequency. The lower cut-off of the OI-SR echo is 9.9 kHz. The time delay of the OI-SR echoes decreases very sharply near the lower cut-off region.

Figure 2.9b shows the altitudinal profiles of plasma frequency (f_{pe}; shown by the dashed dotted curve), f_{ce}; shown by the dotted curve), lower hybrid frequency (f_{lh}; shown by the solid curve) and effective ion mass (m_{eff}; shown by the dashed curve) along the satellite L-shell. The propagation of the MR echo is shown by the ray path illustrated by frequencies f_1 and f_2 (red colored loop). The frequency f_1 and f_2 are greater than f_{lhsat} and less than the f_{lhmax1} frequency. The ray paths are shown from the satellite altitude to the altitude $f \sim f_{lh}$, at which they get reflected. The gold colored loop is for OI-SR echoes, which are observed at frequencies $f_3 > f_{lhmax1}$. These rays get reflected from the Earth-ionosphere boundary.

Figure 2.9c is a schematic representation of the MR and OI-SR echoes. The frequencies f_1 and f_2 for the MR echo (shown by the red colored loop) get reflected at altitude $f \sim f_{lh}$ (shown by the dashed line). The OI-SR echo (f_3; shown by the gold loop) gets reflected at the Earth-ionosphere boundary. Tx is the transmitter signal (NLK) observed on the plasmagram. The horizontal traces seen below 40 ms of time delay are the proton cyclotron echoes (Carpenter et al., 2007). MR echoes seen in low to mid latitudes are accompanied with PC echoes most of the times.

These examples of echoes can be used for determination of electron density and ion compositions at mid latitudes along the field lines in the plasmasphere.

2.3.3 Example of MR echo observed simultaneously with OI-SR and NI-SR echoes for IMAGE altitude below $R_{flhmax1}$ at high latitude
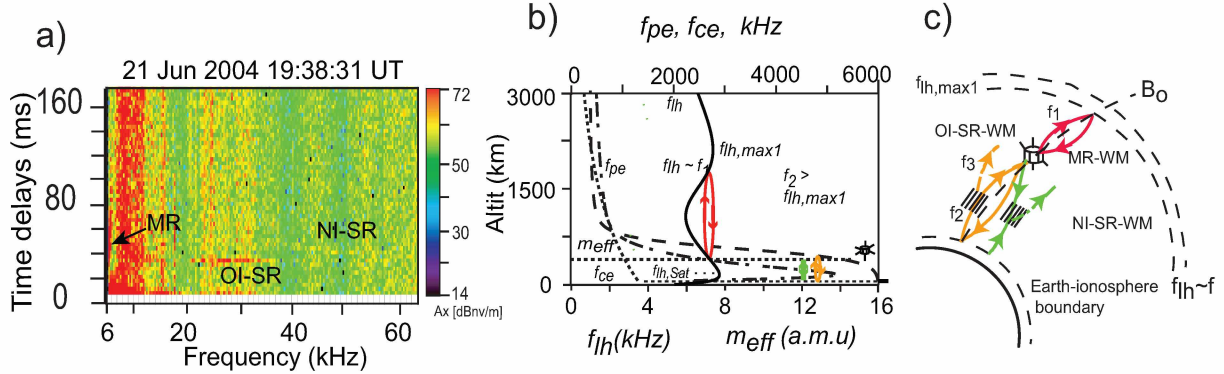
Figure 2.10   MR observed with OI-SR and NI-SR for IMAGE altitude above $R_{flhmax1}$ and at high latitude
a) Multipath magnetospherically reflected (MR), obliquely incident specularly reflected (OI-SR)and normally incident specularly reflected whistler mode echoes received during the transmission of pr#38
b) Typical variation of plasma parameters f_{pe} (black dash-dot curve), f_{ce} (black dotted curve), f_{lh} (black solid curve), m_{eff} (black dashed curve), with altitude along the field line passing through the IMAGE satellite. (b) Schematic representation of magnetospheric reflections at altitudes where $f_{lh} \sim f$ (red colored rays) and of specular reflections of normally incident (NI) and obliquely incident (OI) rays at the Earth ionosphere boundary (green and gold colored rays, respectively)
c) Schematic showing the formation of MR (red colored ray) by reflecting at attitude $f \sim f_{lhmax1}$, OI-SR (gold colored ray) and NI-SR(green colored ray) by reflecting at Earth-ionosphere boundary.

Figure 2.10a shows a multipath MR echo with discrete and patchy OI-SR and NI-SR echoes. The location of the satellite is given in the figure. There is no plasmapause seen on the dynamic spectra of this day. The MR echo is observed in three frequency bins from 6.6 kHz to 7.2 kHz. There is a data gap in the first two bins (6 kHz, 6.3 kHz) and it is likely that the MR echo reached IMAGE at these frequencies and below. A band of noise in the frequency range 8 to 12.5 kHz is observed on the plasmagram. This noise band is frequently observed on the plasmagrams and its origin is not clear. The NI-SR and OI-SR echoes are visible in the range ∼34-52 kHz and ∼22-41 kHz, respectively. Both the NI-SR and OI-SR echoes are patchy (with gaps between observed frequencies) due to deflection of the ray path in the presence of field aligned irregularities (FAIs). We have reported this case in Sonwalkar et al., (2009, 2011a).

Figure 2.10b shows the altitudinal profiles of f_{pe} (dashed dotted curve), f_{ce} (dotted curve), f_{lh} (solid curve) and m_{eff} (dashed curve) along the satellite L-shell. The raytracing simulation results show that $R_{flhmax1}$ is at ∼2100 km and the MR echo is formed by reflecting the rays from altitudes above the satellite altitude. We generally do not see all three types of echoes simultaneously. Only

three such cases are observed during the transmission of pr#38. Analysis of these types of MR echoes can provide ion density distribution below the satellite altitude.

Figure 2.10c shows a schematic representation of the three types of echoes observed on the plasmagram of Figure 2.10a. The frequencies f_3 and f_4 get deflected by the FAIs and do not come back to the satellite, which explains the patchy nature of the observed NI-SR and OI-SR echoes.

2.3.4   Example of overlapping NI-SR and MR echo
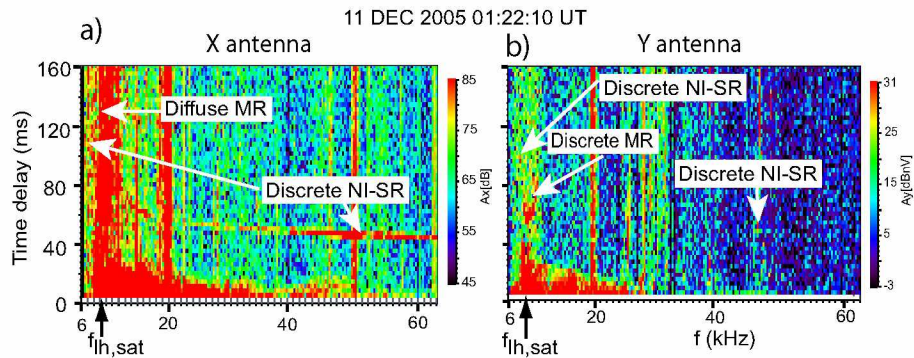
Figure 2.11   Example of overlapping NI-SR and MR echo
a) Example of overlapping diffuse magnetospherically reflected (MR) and discrete normally incident specularly reflected (NI-SR) echoes received on X-antenna during the transmission of pr#38 at 2440 km altitude, above $R_{flhmax1}$.
b) Discrete MR and NI-SR echo observed on the Y-antenna.

Plasmagrams in Figure 2.11a and 2.11b show NI echoes. It is possible that in most of the soundings from above $R_{flhmax1}$, the RPI antenna did not generate sufficient WM radiation at the low wave normal angles and the low frequencies required for the generation of NI echoes close to f_{lhmax1}. Another possibility is that low wave normal angles WM waves injected from IMAGE encountered FAIs, which deflected their raypaths. As indicated in Figure 2.10c), the raypath of an NI echo tends to deviate from the field line B_0 passing through the satellite, whereas the paths of MR and OI lie close to B_0. It is possible that, in some cases, WM waves injected at small wave normal angles that were capable of producing NI echoes encountered FAIs, whereas those injected at large wave normal angles and producing MR and OI echoes did not. When NI echoes were evident, they were generally found at higher frequencies and from sounder altitudes below $R_{flhmax1}$. The NI echo observed on Figure 2.11 at frequencies below f_{lhmax1} (illustrated when IMAGE was at 2440 km, $\lambda = 28.5°$N, L = 1.79, MLT = 8, model f_{ce} = 514.4 kHz in Figure 2.11a), from the X-antenna, shows a diffuse MR echo and a discrete NI echo that extends below 8 kHz, the low frequency limit of the MR trace. We have reported this case in Sonwalkar et al. (2011a). In Figure 2.11a), the

lower and upper cut-off frequencies of the MR echoes cannot be identified. Figure 2.11b, from the Y antenna, shows a discrete MR echo, presumably embedded in the diffuse band shown in Figure 2.11a. In Figure 2.11b), the SR echo is barely visible. In this figure, two SR echo segments that appear stronger than the background in the ranges 7.5-8.1 kHz and between 44.7-50.1 kHz have been identified by comparing the plasmagram of Figure 2.11b with that of Figure 2.11a. In order to verify this particular identification of MR and NI-SR echoes further, ray tracing analysis was performed. It is found that with a reasonable magnetospheric density model, it is possible to match the calculated time delays with those observed. This is the only case where overlapping MR and NI echoes were observed.

2.3.5 Example of simultaneous observation of NI-SR and OI-SR echoes at low latitude
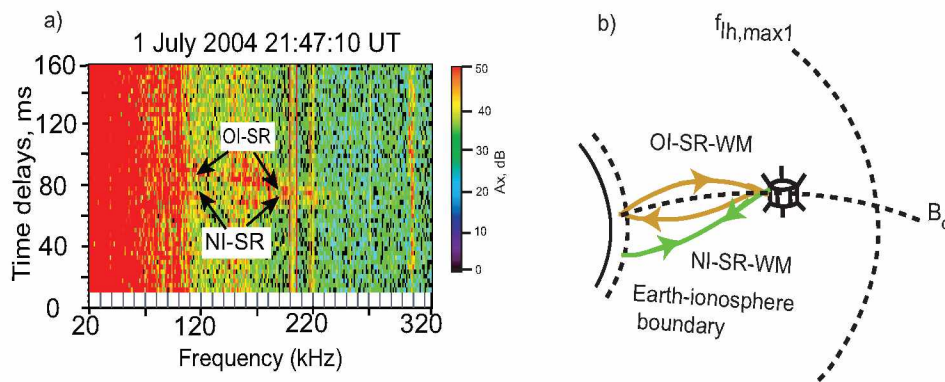
Figure 2.12 Example of observation of NI-SR and OI-SR at low latitude
a) Multipath OI-SR and NI-SR in the transmission of Program 57 when IMAGE was in equatorial region
b) Schematic showing the formation of NI-SR (green colored ray) and OI-SR (gold colored ray) get reflected at Earth-ionosphere boundary and form the echoes.

Figure 2.12a shows an example of NI-SR ($\sim$101.6-179.6 kHz) and OI-SR ($\sim$101.6-220.4 kHz) echoes observed on the X-antenna on 1 July 2004 at 21:47:10 UT at L-shell 1.22, altitude $\sim$1335 km, λ = 7°N, and MLT = 6.7. There is a noise band present in the frequency range $\sim$20 kHz to 100 kHz. The origin of this noise band is not known. The raytracing results show the f_{lhmax1} altitude is $\sim$1400 km, which is very close to the satellite altitude. The time delay calculated from raytracing simulation for NI-SR agrees well with the lower echo and the time delay calculated for the OI-SR agrees well with the upper echo. We have reported this case in Sonwalkar et. al., (2009, 2011a). These kinds of echoes are important to study the electron density distribution in the equatorial

region both along the field line (OI echo) and along the NI echo ray path. The patchy and multipath nature of the echoes can provide information about the FAIs present in the equatorial region, which can be compared with the FAIs present in the mid-latitude region.

2.3.6 Example of simultaneous observation of NI-SR echoes at low latitude from two hemispheres:
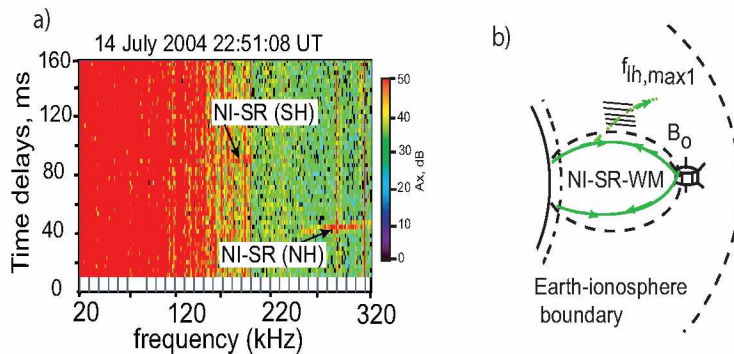
Figure 2.13 Example of observation of NI-SR at low latitude from two hemispheres
a)Discrete NI-SR from two hemispheres in the transmission of pr#57 when IMAGE was in low latitude region
b) Schematic showing the formation of NI-SR (green colored ray) which gets reflected at Earth--ionosphere boundary from the either hemispheres and forms echo.

Figure 2.13a shows an example of two NI-SR echoes observed on the X-antenna on 14 July 2004 at 22:51:06 UT at L-shell 1.28, altitude ~1150 km, $\lambda = 16°N$, and MLT = 5.9. The raytracing results show that the upper SR echo observed in the frequency range 182 kHz to 201.2 kHz is NI reflected from the southern hemisphere (SH). The lower cut-off of the NI-SR reflected from the SH is 150 kHz. There is a noise band present in the frequency range 20 kHz to ~170 kHz. The echo below 182 kHz may be buried under the noise band. This noise band appears in a number of plasmagrams. Its upper cut-off varies between ~100 kHz to ~200 kHz. The lower SR echo observed in the frequency range 254 kHz to 326 kHz is the NI reflected from the northern hemisphere (NH). From raytracing simulations, the lower cut-off of the NI-SR from the northern hemisphere is 179.6 kHz. The echo is observed from 254 kHz, as it may get deflected by FAIs at frequencies below 254 kHz before coming back to the satellite. The raytracing results show the f_{lhmax1} altitude is ~1700 km, which is above the satellite altitude. The time delay calculated from the raytracing simulations for both the NI-SR echoes agrees well with the measured time delay. Figure 2.13b shows a schematic representation of the NI-SR echoes from both hemispheres. The FAIs present in NH deflect the part of the NI-SR

31

rays below 254 kHz before coming back to the satellite. We have reported this case in Sonwalkar et al., (2009, 2011a). These kinds of echoes are important to know the simultaneous electron density distribution of both the hemispheres in the equatorial region and can also be compared with the FAIs of both hemispheres.

2.4 Examples of cases of WM echoes along the satellite orbit

The WM echoes in successive cases show the changes of time delay as the satellite moved from the high latitude of the northern to the low latitude of the southern hemisphere. This is because of the integral relationship between the change of electron density (group velocity, v_g) and the path length (ds) covered by the ray.

$$T = \int \frac{ds}{v_g} \tag{2.5}$$

The time delay pattern of these echoes gives the propagation characteristics of WM at different latitudes. The WM time delays provide an estimate of the measure of electron density between the IMAGE and underlying ionosphere.

2.4.1 Successive cases of only MR echo and MR echo observed with SR along the orbit
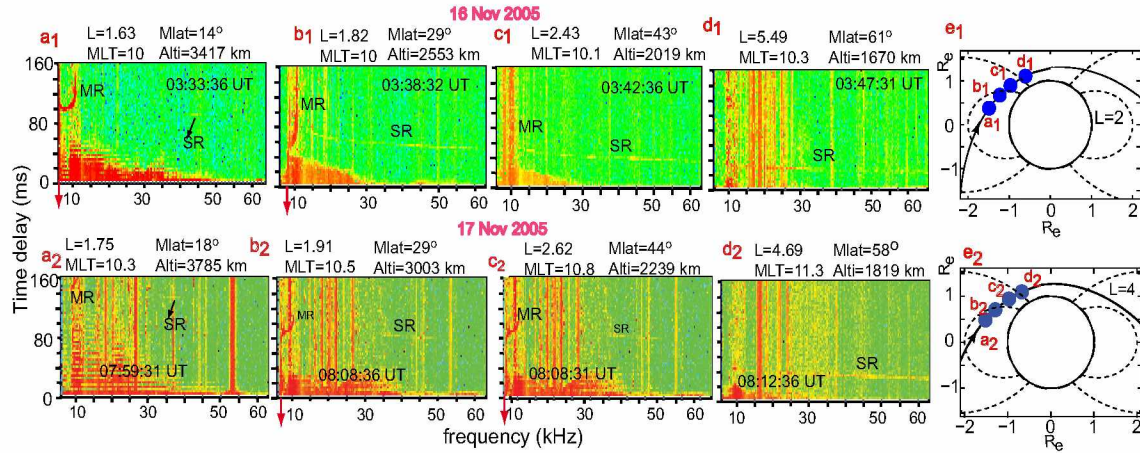
Figure 2.14 Successive cases of only MR and MR observed with SR along the orbit. a_1), b_1), c_1), and d_1) show series of f vs t plasmagrams showing whistler mode echoes on four successive soundings on 16 Nov 2005 extending from L = 1.63 to L = 5.49 (outside plasmapause Lp~4.57). Figure e_1) shows the plot of the low-altitude portion of the IMAGE polar orbit. The locations of IMAGE for cases are indicated by blue dots. Dipole field lines at L = 2 and L = 4 are shown as a reference. The magnetic local times for these cases varied from 9.98 to 10.39. a_2), b_2), c_2), and d_2) show series of f vs t plasmagrams showing whistler mode echoes on four successive soundings on 17 Nov 2005 extending from L = 1.75 to L = 4.69 (outside plasmapause; plasmapause Lp~4.55). e_2) shows the plot of the low-altitude portion of the IMAGE polar orbit. The approximate locations of IMAGE for cases are indicated by blue dots. Dipole field lines at L=2 and L=4 are shown as a reference. The MLT for the cases in these figures varied from 10.53 to 11.31.

Characteristics of MR and SR echoes in terms of time delay and cut-offs change as IMAGE moved from the lower L-shell region (inside the plasmasphere) to the higher L-shell region (outside the plasmasphere). Figure 2.14 shows frequency vs virtual range of discrete/multipath MR-WM and SR-WM echoes received during successive transmissions on two different days as IMAGE moved through perigee in the northern polar region. All the successive cases shown here are from pr#38. In between those successive cases of pr#38, pr#23, pr#26 and pr#33 were transmitted. pr#23 and pr#26 are in TTD (Thermal noise time domain) mode. pr#33 has a frequency range from 15 kHz to 72 kHz, which is not suitable for MR echo observation. pr#38 covers the frequency range from 6 kHz to 63 kHz. Each of these frequencies are spaced by 1.5 kHz. The virtual range covered by this program is $0.3R_e$ to $4.1R_e$, which is equivalent to 12.75 ms to 174.33 ms. The echoes shown in Figure 2.14 for 16 November 2005 are separated by ~10-14° in latitude, a result of such sounding being separated in time by ~5 min.

The first plasmagram of Figure $2.14a_1$ was observed on 16 November 2005 at 03:36:32 UT. At

this time, IMAGE was at $\lambda = 14°N$, L$\sim$1.63, MLT$\sim$10, and $f_{ce}\sim$307 kHz (IGRF model). The lower hybrid resonance (f_{lhsat}; indicated by the arrow) appeared at 6.3 kHz. There is a data gap at 6 kHz, so the f_{lhsat} could be 6-6.3 kHz. The MR echo observed is discrete, occupying a frequency range from 6.6-10.8 kHz. The MR echo observed is U shaped. Generally, the echoes observed in low latitude region (L<1.8) are of this shape. There is a patchy SR echo observed in the frequency range 40.5-45.6 kHz and at an average time delay of $\sim$100 ms. Raytracing analysis shows that this is an OI-SR echo. The local proton-gyro period (t_p) calculated from the well separated PC echoes observed on this plasmagram is $\sim$6.1 ms (Carpenter et al., 2007) and the local $f_{ce} = 1836/t_p$ ($\sim$300 kHz) and is comparable to f_{ce} calculated from the IGRF model ($\sim$307 kHz).

The next plasmagram in Figure 2.14b$_1$ was observed at 03:38:32 UT. At this time IMAGE was at $\lambda = 29°N$, L$\sim$1.82, MLT$\sim$10 and $f_{ce}\sim$492 kHz (IGRF model). The lower hybrid resonance (f_{lhsat}) appeared at 8.1-8.4 kHz. The MR echo observed is multipath, occupying a frequency range of 8.7-10.8 kHz. There is an OI-SR echo observed throughout the plasmagram starting at a frequency above the upper cut-off of the MR echo (10.8 kHz). The time delay for the MR and OI-SR echoes calculated from the raytracing simulation is comparable to the observed time delay. The average time delays of both MR and the OI-SR echoes are lower than the previous plasmagram, as IMAGE, at this time, had moved to a higher L-shell and lower altitude, which made the path traveled by the WM waves lower. There are a number of transmitted signals observed on this plasmagram. Among them, the transmitter signals at $\sim$14.7 kHz, $\sim$18.3 kHz (JJH, VTX), $\sim$26.4 kHz (NPM, NLK, NPG, NEJ) and $\sim$49.8 kHz (SXA) are the strongest ones. PC echoes are also seen in this plasmagram, but they are not sufficiently separated to measure the proton-gyro period (t_p).

The plasmagram in Figure 2.14c$_1$ was observed at 03:42:36 UT. At this time IMAGE moved to a lower altitude and a higher L-shell ($\lambda = 42.7°N$, L$\sim$2.43), MLT$\sim$10.15, and $f_{ce}\sim$676 kHz (IGRF model). The lower hybrid resonance (f_{lhsat}; indicated by the red arrow) appeared at 8.1-8.4 kHz. The MR echo observed is diffuse. Its upper cut-off could be $\sim$10.8 kHz. The MR rays at this time encountered FAIs which lead to a diffuse MR echo. There is an OI-SR echo throughout the plasmagram. Its time delay is $\sim$15-20 ms lower than the time delay of the OI-SR echo observed at 03:38:32 UT. This can be due to decreased electron density at higher L-shells and decreased path lengths at lower altitudes. The transmitter signals observed at frequency $\sim$19.8 kHz (NWC/NPM/NPL/NPG/TBA) and at $\sim$37.8 kHz (NRK/TFK).

The plasmagram in Figure 2.14d$_1$ was observed at 03:47:31 UT when IMAGE was at $\lambda = 61°N$, L$\sim$5.49, MLT$\sim$10.39 and $f_{ce}\sim$822 kHz (IGRF model). At this time IMAGE was outside the

plasmapause. From the f_{uh} emission observed on the dynamic spectra the plasmapause is seen at L-shell ∼4.5. We do not see any f_{lhsat} resonance or MR echo on the plasmagram. The lower cut-off of the SR echo observed is ∼9 kHz. There is a noise band observed from ∼9 kHz to ∼25 kHz. Its origin is not known and it could be overlapped with few transmitter signals in that frequency range.

The plasmagrams in Figure 2.14a_2-d_2 explain similar echoes as those shown in Figure 2.14a_1-d_1. They were observed on 17 Novemebr 2005 at 07:59:31 to 08:12:36 UT. The satellite locations are given in each of the plasmagrams. Figure 2.14e_2 shows the position of the satellite for each of the cases with blue dots. The transmitter signals received by IMAGE, shown in the plasmagram in Figure 2.14a_2 at frequency at ∼53.4 kHz and in Figure 2.14d_2 at frequency 16.6 kHz, were forward scattered by small scale FAIs, hence, were Doppler broadened in frequency (f∼0.6 kHz, f∼1.2 kHz respectively).

In both sets of examples, the time delay of the echoes changed by a factor of ∼2.5, which suggests a change of Ne on the order of ∼6 (square of 2.5). The diffuse MR echoes and broadened transmitter signals can provide sizes and locations of FAIs.

2.4.2 Successive cases of SR echo along the orbit
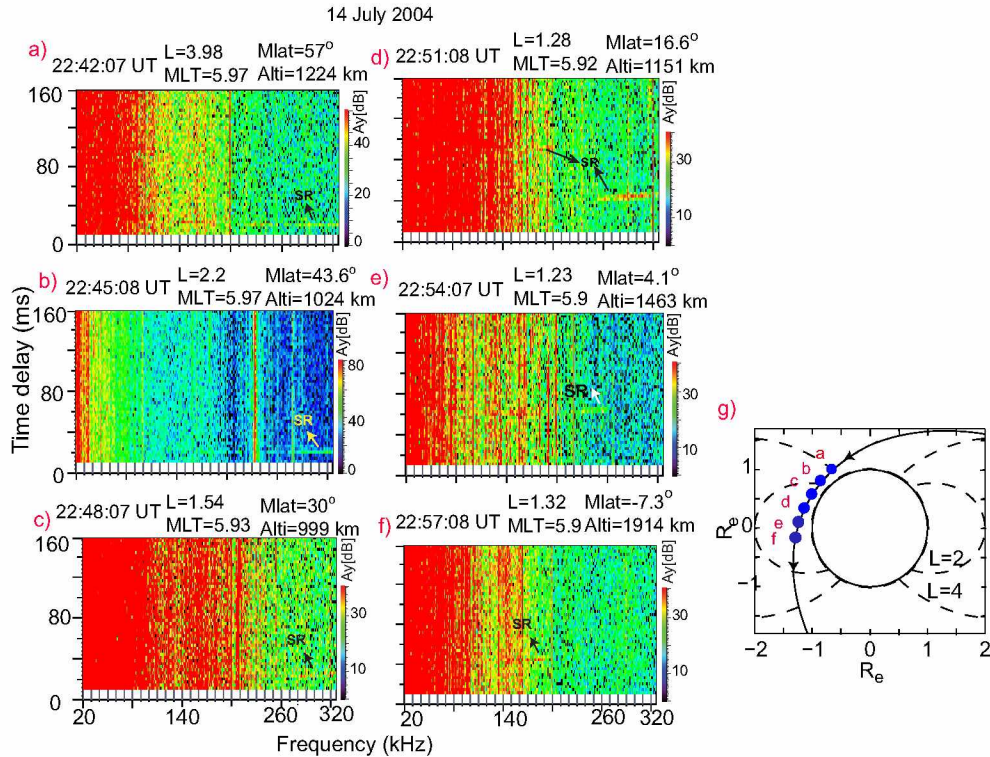
Figure 2.15 Successive cases of SR along the orbit. Figures a) to d) show series of f vs t plasmagrams showing WM echoes on five successive soundings on 14 July 2004 extending from L~4.02 to L~1.32 inside the plasmasphere. Orbit of IMAGE is shown in figure g) with the approximate locations of IMAGE, for cases in a)-f) (blue dots). Dipole field lines at L=2 and L=4 are shown as a reference. The MLT for the cases in a)-e) varied from 5.97 to 5.88.

Figures 2.15 a-d show the frequency vs virtual range of discrete/multipath SR-WM echoes received on the Y-antenna during six successive transmissions as IMAGE moved from the equatorial region through perigee in the northern polar region. The echo pattern is the strongest in the Y antenna among all the three antennas. All the successive cases shown here are of pr#57. In between the successive cases of pr#57, pr#23, pr#26, and pr#15 were transmitted. These three programs are in TTD (Thermal noise time domain) mode. pr#57 covers the frequency range from 20 kHz to 326 kHz. These frequencies are spaced by 1.2 kHz with linear stepping. The virtual range covered by this program is $0.3R_e$ to $4R_e$, which is equivalent to 12.75 ms to 170.08 ms. All of these plasmagrams have noise band of unknown origin below frequency 150 kHz. The study of successive cases can give the electron density distribution along the satellite orbit. This set of examples is similar to Figure 2.14 but only for SR echoes. The plasmagram in Figure 2.15d shows two SR echoes from two hemispheres with a nearly 40 ms time delay (also confirmed with raytracing

simulations). In the next plasmagram, Figure 2.15e, only one SR echo is seen. In the frequency range 264.8 kHz to 320 kHz the time delay increases slightly with frequency. This is due to the nose frequency. At frequencies above the nose frequency, time delay increases with frequency. The nose frequency generally occurs at f$\sim$f$_{ce}$/2, where f is the whistler frequency and f$_{ce}$ is the local electron cyclotron frequency (Helliwell, 1965). At this time transmission, the satellite is very near to the equator, hence, the time delay of the echo reflected from both hemispheres will be comparable (also obtained from raytracing analysis).

Figure 2.15 shows the typical dispersion characteristics of SR echoes as IMAGE moved from the higher L-shell region to lower L-shells. The change in electron density encountered by IMAGE is integrally related to the time delay of the observed echoes. The time delays of the echoes in the first three plasmagrams (Figure 2.15 a, b, c are comparable at frequencies $\sim$240 kHz and above. Even though the altitude decreases as the satellite moves from a to c, as shown in the orbit diagram of Figure 2.15, the satellite also moves towards the lower L-shell where the electron density increases, causing the decrease in group velocity. The decrease in path length (since the satellite moves towards a lower L-shell) is compensated by the group velocity, hence, the time delay does not change significantly. There is a factor of $\sim$3.5 change in the time delay between the plasmagrams of Figure 2.15c and Figure 2.15f. This suggests a change in electron density by a factor of $\sim$12 (square of $\sim$3.5). This type of example provides a latitudinal change of Ne with distance along field lines.

2.5 Examples of WM echoes near plasmapause

2.5.1 Cases of MR echo observed near the plasmapause
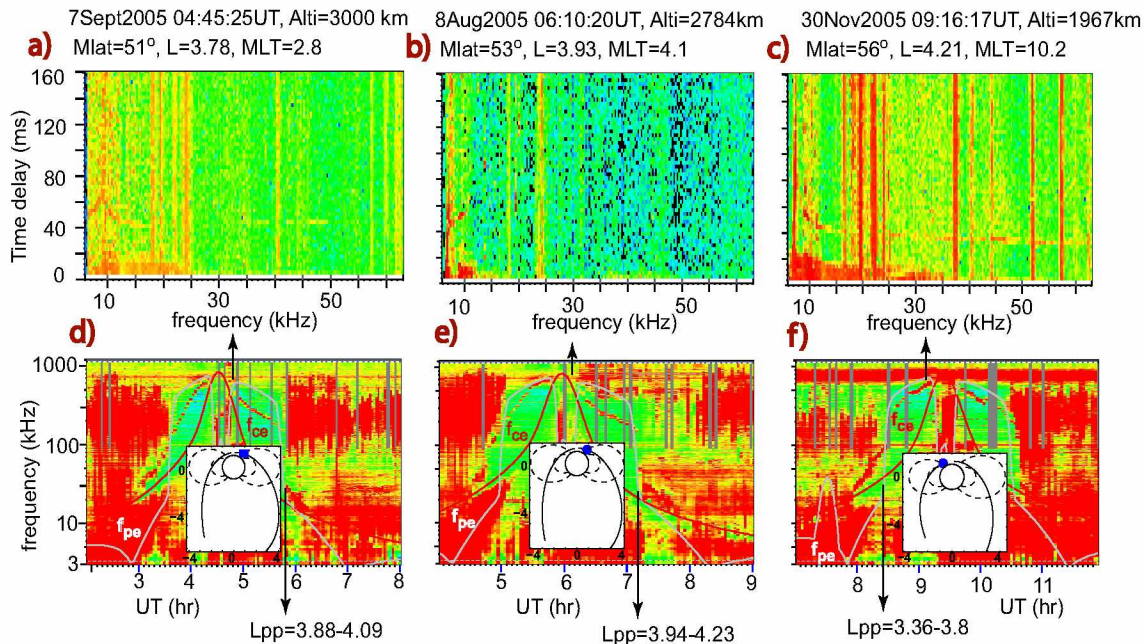
Figure 2.16 Cases of MR observed near the plasmapause. Figures a) to c) show f vs t plasmagrams showing MR-WM echoes observed when IMAGE was near the plasmapause region. Figures d) to f) show corresponding dynamic spectrograms of those cases with the location of plasmapause with satellite orbit plot in the inset.

The echoes observed near the plasmapause region can provide information about the change of electron density distribution along the L-shell there. However, the echoes observed near this region do not show any special appearance (in terms of cut-offs and time delays) compared to other echoes observed well within the plasmasphere.Figure 2.16d displays a dynamic spectrogram obtained by the RPI during the interval of 0200 UT to 0800 UT on 09 September 2005. In the spectrogram covering waves from 3 to 1000 kHz, the upper hybrid resonance (UHR) band with an enhanced signal is clearly displayed. The red curve in the spectrogram denotes f_{ce} calculated using the T96 model (Tsyganenko, 1995). The white curve is the model f_{pe}. There is a drop in f_{uh} emissions in the time interval 05:43:33 UT to 05:47:11 UT when the f_{uh} changes from 160 kHz to 73 kHz. Showing typical plasmapause features, the electron density dropped from 312/cc to 60/cc, about a factor of 5 over the L-shell range 3.88 to 4.09. The width and density drop in this case are consistent with that observed by Carpenter et al., (2000): widths ranging from $\Delta L \sim 0.5$ to $\Delta L \sim 1.5$ and density decreasing by a factor of ~ 2-5. The inset at the middle of the dynamic spectrogram presents

IMAGE orbit configuration with the black geomagnetic field lines denoting L = 3.88 and L = 4.09 (position of the plasmapause). The time and satellite locations are given at the top of the plasmagram. This case was observed when IMAGE was at the plasmapause region. The discrete MR echo is observed in the frequency range 6.6-9 kHz and the discrete/patchy OI echo is observed in the range of 9.6-50 kHz. The lower cut-off is lower than 6.6 kHz, which is not observed in the plasmagram due to transmitted program limitations (pr#38). Raytracing analysis shows the f_{lhsat} at 6.3 kHz. The satellite position is shown as a blue dot on the orbit diagram. The study of cases near the plasmapause can provide information about the electron and ion density profile near the plasmapause region and their effect on the appearance of the echo.

Figure 2.16b and 2.16f show another example set of dynamic spectra and corresponding plasmagrams, respectively, observed near the plasmapause region. There is a drop in f_{uh} emissions in the time interval 07:09:00 UT to 07:13:29 UT when the f_{uh} changes from 160 kHz to 52 kHz (the electron density dropped from 310/cc to 28/cc, about a factor of 10 over the L-shell range 3.94 to 4.23). The small panel in the middle of the dynamic spectrogram shows the IMAGE orbit configuration with the black geomagnetic field lines denoting L = 3.94, and L = 4.23 (position of the plasmapause). The location of the satellite is given in Figure 2.16b above the plasmagram. The discrete MR echo was observed in the frequency range 7.5-11.1 kHz; the f_{lhsat} resonance is 6.9-7.2 kHz (shown by the black arrow at the bottom of the plasmagrams). No SR echo is observed in this case.

In the next example, the case is just outside the plasmapause. The plasmapause (Figure 2.16c) is measured from the drop in f_{uh} emissions in the time interval 08:32:54 UT to 08:28:21 UT when the f_{uh} changes from 226 kHz to 103 kHz (the electron density dropped from 606/cc to 109/cc, about a factor of 6, over the L-shell range 3.8 to 3.36). The inset shows IMAGE orbit configuration with geomagnetic field lines denoting L = 3.8, and L = 3.36 (position of the plasmapause) and the satellite location shown in blue. The plasmagram shows a very narrow MR (7.2-7.5 kHz) (it may be the f_{lhsat} resonance too) observed with discrete OI-SR echo when IMAGE was at an altitude of ~1967 km, at an L-shell of 4.21, MLT~10.2 and f_{ce}~623 kHz (IGRF model).

2.5.2 Examples of SR echo observed near the plasmapause:
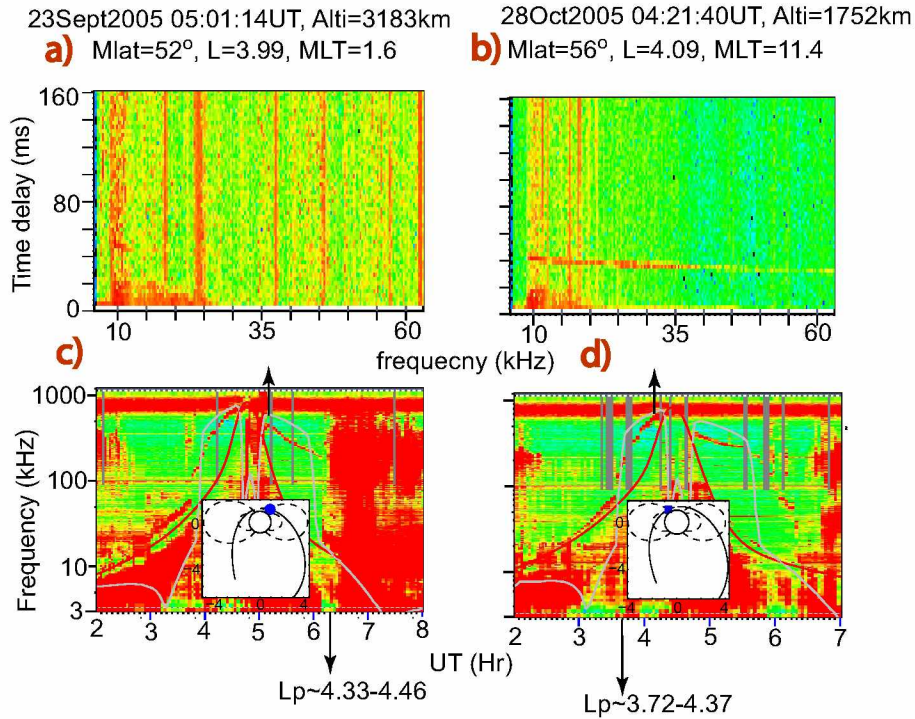
Figure 2.17 Cases of SR observed near the plasmapause. Figures a), b) show f vs t plasmagrams showing SR-WM echoes observed when IMAGE was near the plasmapause region. Figures c), d) show the corresponding dynamic spectrograms of those cases with the location of plasmapause with satellite orbit plot with its location at the inset.

Figure 2.17 shows example cases of plasmagrams observed with only SR echoes just at the plasmapause. Both of these cases are observed without any MR echoes. The cases in the first column were observed on 23 September 2005 when IMAGE was at an altitude of ∼3180 km, at an L-shell of 3.99, MLT∼1.59, and f_{ce}=408 kHz (IGRF model). The plasmapause was observed in the time interval 06:08:15 UT to 06:10:20 UT when the f_{uh} emissions drop from 195 kHz to 82 kHz in the L-shell range 4.33 to 4.46. The Ne at this time changes from 468/cc to 79/cc (by a factor of ∼8). In the plasmagram shown in Figure 2.17b, observed on 28 October 2005 at 04:21:40 UT, IMAGE was at an altitude of ∼1752 km, an L-shell of 4.09, MLT∼11.44, and f_{ce}∼794 kHz (IGRF model). The dynamic spectrogram shows the plasmapause in the time interval 03:38:32 UT to 03:33:42 UT when the f_{uh} emissions drop from 202 kHz to 79 kHz in the L-shell range 3.72 to 4.37. The electron density dropped by a factor of 13 (447/cc to 34/cc) at this time. On both the plasmagrams the lower cut-off of the SR echo is 9 kHz. It could be lower than 9 kHz as there are a number of cases near these L-shells with the same 9 kHz lower cut-off of the SR echo. In some of these

plasmagrams, the SR echo is seen at frequencies lower than 9 kHz but the echo amplitude is very low. This suggests that there may have problems with the power of the frequency transmitted lower than 9 kHz or the rays at lower frequency may have been scattered away by FAIs. In the past, researchers have reported irregularities on the order of several 100 km to several 1000 km near the plasmapause region and beyond from various satellites and VLF transmitter observations. These irregularities are associated with the plasma instability, closely connected with the formation mechanism of the plasmapause (LeDocq et al., 1994; Carpenter and Anderson 1992; Moldwin et al., 1995; Inan et al., 1977; Chappell et al., 1971; Lemaire and Gringauz 1998). The patchy nature of the SR echo, the diffuse WM echoes, and spectral broadening of the transmitter signals observed on the plasmagrams can provide more information about irregularities near the plasmapause region.

2.6 Occurrence pattern of WM echoes during years 2000-2005

2.6.1 Occurrence pattern of only MR echoes and MR echoes observed simultaneously with SR echoes
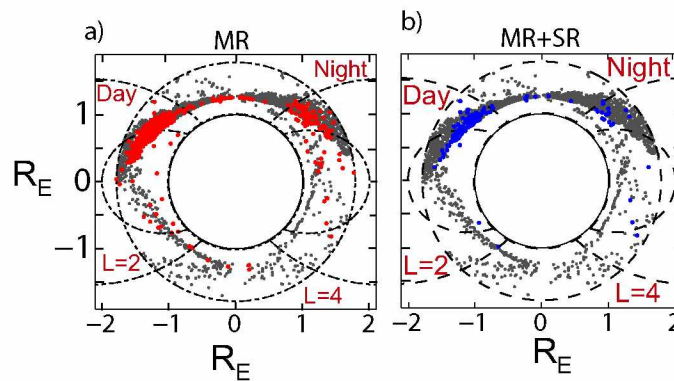
Figure 2.18 (a) Occurrence pattern of MR echoes and (b) MR echoes observed simultaneously with SR echoes in magnetic meridional plan.

The factors on which the echo occurrence depends are radiated power and pattern, antenna orientation, frequency, distance traveled and spreading losses, efficiency of reflection, losses due to absorption (D region), and the presence of FAIs along the signal raypaths. Figures 2.18a and b show the occurrence pattern of only MR echoes and MR echoes accompanied with SR echoes (OI/NI) along IMAGE orbit in the geomagnetic meridional plane. The grey dots in both the figures are the transmissions of pr#38, pr#29, and pr#36. These three programs transmitted in frequency ranges suitable for observation of MR echoes (represented by red dots in figure 2.18a. pr#29 and

pr#36 were transmitted in the year 2000 (∼300 total transmissions) and ∼15 MR echoes were observed in these two programs. Most of the MR echoes were observed in the year 2005 (August-December), due to a large number of transmissions of pr#38 (∼2100). Approximately 400 MR echoes were observed during this time, which is ∼20% of the total transmission of pr#38. The blue dots in Figure 2.18b represent the MR echoes accompanied by SR echoes. ∼250 such cases are observed.
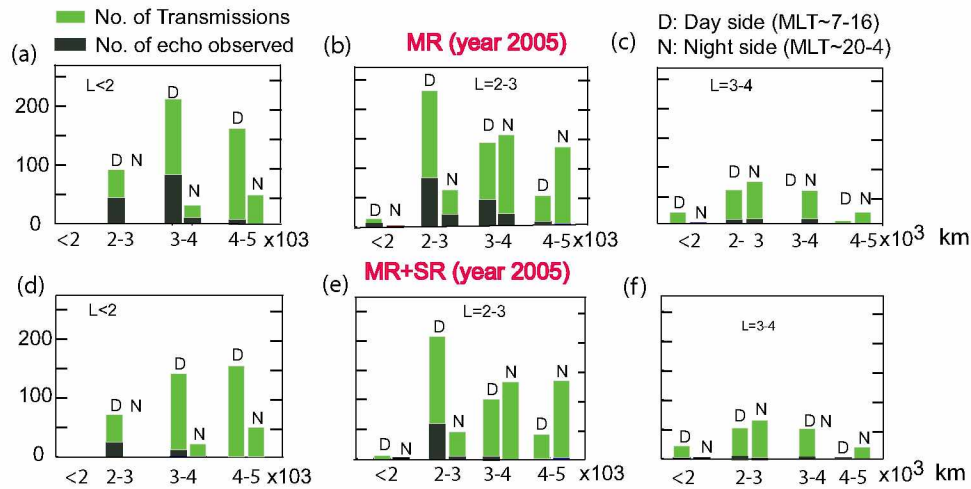
Figure 2.19 Occurrence pattern of MR echo in day and night side as a function of the altitude at different L-shell range.

The first panel in Figure 2.19 shows a histogram of the MR echoes (black) with respect to the transmissions (green) in the day side (MLT∼7-16) and night side (MLT∼22-2) of the plasmasphere at different altitude ranges. The cases are categorized into three sections based on L-shells: L<2, L = 2-3, and L = 3-4. The second panel is the same type of representation of the MR echoes observed with the SR echoes. In both, more echoes were observed on the day side than night side. One of the reasons for this could be the IMAGE orbit orientation on the day side. The echoes were mostly observed when there is a large number of transmissions in the mid latitude region (L-shell ∼1.8 to 2.6; λ ∼ 25° to 45°) in the altitude range 2000-3000 km. The day side IMAGE orbit covers this region, while at night side in this region of L-shells, the altitude range was a little higher (3000-4000 km).

2.6.2 Occurrence pattern of single and double SR echoes
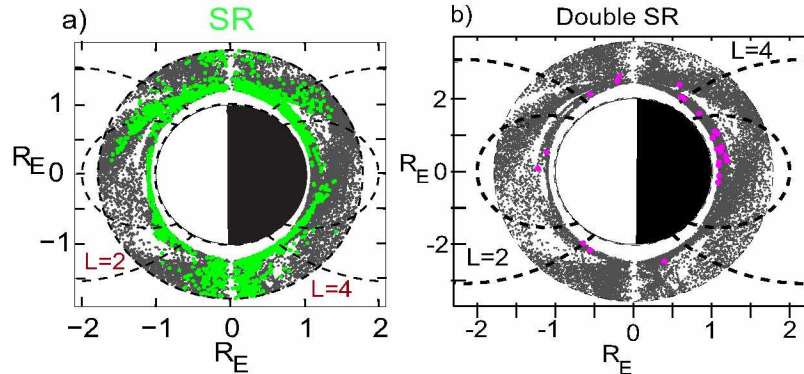
Figure 2.20 (a) Occurrence pattern of total SR echoes (b) and total double SR echoes during 2000-2005 in the magnetic meridional plan.

Figure 2.20a shows the occurrence pattern of total SR echoes observed during the years 2000 to 2005. SR echoes were mostly observed on pr#5, pr#20, pr#21, pr#29, pr#38, pr#56 and pr#57. pr#20, and pr#21 were transmitted in the polar region during the years 2002 and 2003. The echoes observed in these two programs are all diffuse. During the years 2003 and 2004, when IMAGE perigee was ~600 km in the equatorial region, we see a large number of discrete echoes in pr#5, pr#56, and pr#57. SR echoes are observed in all MLTs below 5000 km wherever the transmissions were made. During the years 2000-2004, the SR echoes were observed on ~10-12% of total transmissions (mainly on pr#5, pr#56, pr#57). In the year 2005, SR echoes were observed on ~20% of total transmissions on pr#38 due to its low frequency range. Figure 2.20b shows the simultaneous occurrence of two SR echoes. There are 30 cases of two SR echoes (magenta dots). All these cases are below 2000 km of altitude, covering low to higher L-shells. These echoes appear in all types including discrete, multipath, and diffuse. Nine cases observed in the low latitude region could have two SR echoes from both hemispheres.

2.6.3 Occurrence of diffuse SR echo observed above 50° latitude
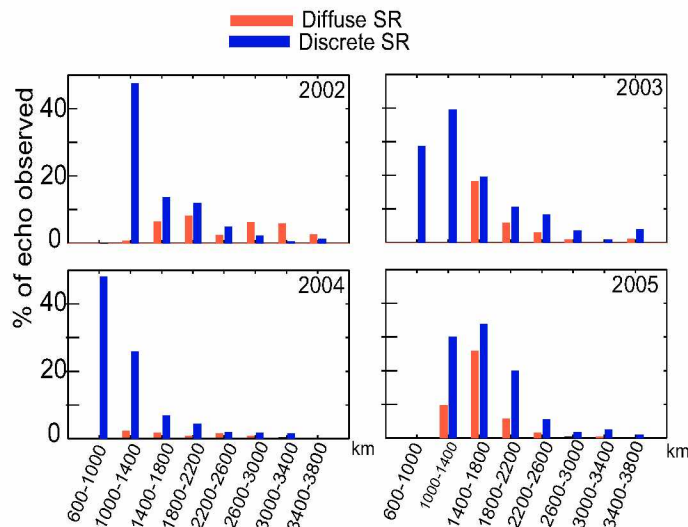
Figure 2.21 Histogram representation of diffuse SR echo (orange) and discrete SR echo (blue) echo observed above 50° latitude range of 600-3800 km).

The echoes with more than ∼10 ms of time delay spread at a given frequency are considered to be diffuse echoes. They are occurred due to scattering by FAIs and rays of the same frequency take different time (as well as path) to reach the satellite, causing the spread of time delays. Diffuse WM echoes are mostly observed in high latitudes because of the presence of FAIs in this region. Figure 2.21 shows a histogram of diffuse SR echoes (orange) and discrete SR echoes (blue) observed above 50° latitude in the altitude range of 600-3800 km for the years 2003 to 2005. Due to the projection of IMAGE orbit, there were not enough cases transmitted in the WM frequency range in the high latitude ranges below 5000 km in the years 2000 and 2001. The total number of echoes (diffuse and discrete SR) observed depends on the number of transmissions in the high latitude region. The altitude ranges are shown in intervals of 400 km. In the year 2002, there were no transmissions below 1000 km. The maximum number of discrete echoes were observed (∼60%) in the altitude range 1000-1400 km, while only 2% diffuse echoes were observed below 1000 km. In the rest of the altitude ranges we see comparable numbers of discrete and diffuse echoes. In the year 2003, in the altitude ranges 600-1000 km and 1000-1400 km, there were no diffuse SR echoes observed, only discrete SR echoes were observed, in rest of the altitude ranges we see significant numbers of diffuse echoes. In the year 2004, there were no diffuse echoes below altitude 1000 km, in the altitude range 1000-1400 km very few (∼5%) diffuse echoes were observed compared to ∼30% discrete echoes observed in this altitude range. In other altitude ranges the observed diffuse and

discrete echoes were comparable. In the year 2005, there were no transmissions below altitude 1000 km. In the altitude range 1000-1400 km, ~10% diffuse SR echoes and ~40% discrete SR echoes were observed. In the altitude range 1400-1800 km, the numbers of observed diffuse and discrete SR echoes are comparable. In the altitude range 1800-2200 km, and above more discrete echoes were observed than diffuse; however, the number of echoes observed decreased above altitude 1800 km for all the years as the number of transmissions also decreased. As diffuse echoes are not observed below altitude 1500 km, it may be an indication that the FAIs that make the echoes diffuse lie at a region above this altitude range. This type of categorization can not be done for MR echoes as not enough MR echoes were observed in the years 2000 to 2004, and most of the programs for SR echoes shown in the figure have a frequency range above the frequency required for observation of MR echoes.

2.7 Occurrence of WM echo on IMAGE/RPI with respect to geomagnetic activity
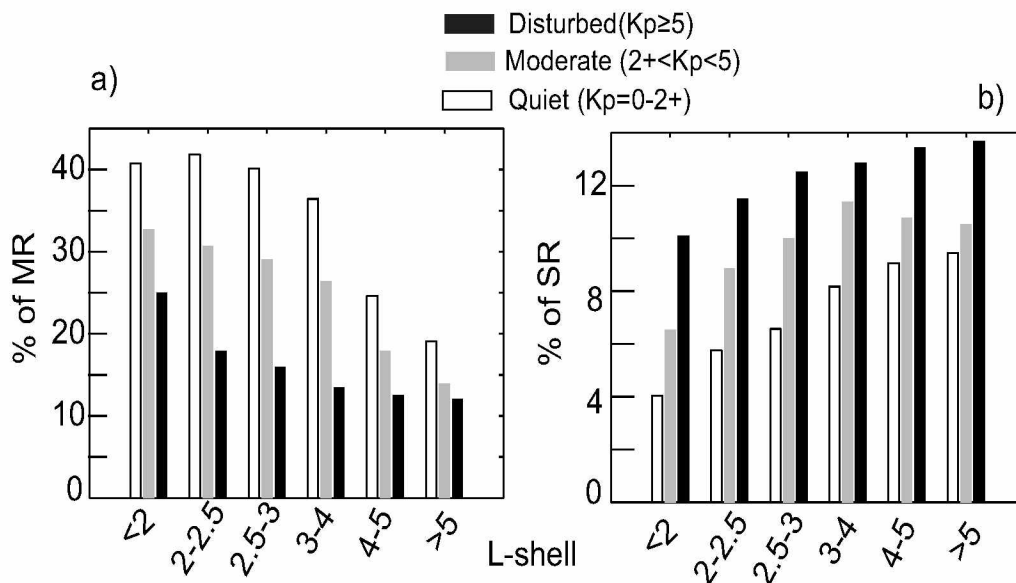
Figure 2.22 Occurrence of total MR and SR echoes below altitude 5000 km relative to the total transmissions at different L-shells and at different geomagnetic conditions. Figure a) shows the relative percentage occurrence of MR echoes, Figure b) shows the relative percentage occurrence of SR echoes at quiet (K_p=0-2+), moderate (2+<K_p<5), and disturbed ($K_p \geq 5$) geomagnetic conditions.

Magnetic field observation using ground-based magnetometers is the most commonly used technique for monitoring magnetic disturbances such as magnetic storms, substorms, auroras, and the

state of the magnetosphere (Meng and Liou, 2002). Several magnetic activity indices have been developed based on magnetometer data to quantify geomagnetic disturbances. For example, the planetary K_p index (Bartels et al., 1939) is constructed to measure magnetic disturbances at middle latitudes. Although its physical meaning is not established, K_p has been widely used as a proxy for global geomagnetic disturbances. Based on the categorization by NOAA (National Oceanic and Atmospheric Administration) (Menvielle et al., 2011, Huttunen et al., 2002, Ritter et al., 2004, Wanliss and Cersosimo, 2006) $K_p = 0\text{-}2+$ is considered as "quiet", $2+<K_p<5$ is considered as "moderate" and $K_p \geq 5$ is considered as "disturbed" geomagnetic period in our analysis.

Figure 2.22a shows a histogram representation of the occurrence of total MR echoes relative to the total transmissions for the years 2000 to 2005 (only pr#38 is included) at different L-shells below altitude 5000 km and at different geomagnetic conditions. White bars with black borders represent quiet periods (K_p=0-2+), grey bars represent moderate periods ($2+<K_p<5$), and black bars represent disturbed periods ($K_p \geq 5$). The K_p considered here is the K_{pmax} of the previous 24 hours K_p indices. In the L-shell range <2, the percentage of MR cases observed during quiet, moderate, and disturbed periods are ~40%, 32%, and 25% of total transmissions, respectively. In the L-shell range 2-2.5, the percentage of cases observed during quiet, moderate, and disturbed periods are ~40%, 30%, and 18% of total transmissions, respectively. In the L-shell range 2.5-3, the percentages of cases observed during quiet, moderate, and disturbed periods are ~40%, 29%, and 16% of total transmissions, respectively. In the L-shell range 3-4, the percentage of cases observed during quiet, moderate, and disturbed period are ~36%, ~26%, and ~13% of total transmissions, respectively. In the L-shell range 4-5, the percentage of cases observed during quiet, moderate and disturbed period are ~24%, ~18%, and ~12% of total transmissions respectively. Above L-shell 5 the percentage of cases observed during quiet, moderate, and disturbed period are ~19%, ~14%,and ~12% of total transmissions, respectively. Above L-shell 2.5, the percentage of MR echoes observed in different geomagnetic conditions decreases with L-shells. In all the L-shell ranges the percentage of MR echo observed is highest during quiet times and the percentage of MR echoes observed during moderate times is higher than during disturbed times.

Figure 2.22b shows the occurrence pattern for SR echoes during the years 2000 to 2005 with respect to geomagnetic activity. In the L-shell range <2, the percentage of SR cases observed during quiet, moderate, and disturbed periods are ~5%, ~6%, and ~8.7% of total transmissions respectively. In the L-shell range 2-2.5, the percentage of cases observed during quiet, moderate and disturbed period are ~7%, ~8%, and ~9.7% of total transmissions respectively. In the L-shell

range 2.5-3 percentage of cases observed during quiet, moderate, and disturbed period are ∼8%, ∼9.4%, and ∼10% of total transmissions, respectively. In the L-shell range 3-4, the percentage of cases observed during quiet, moderate, and disturbed period are ∼9%, ∼11%, and ∼11% of total transmissions respectively. In the L-shell range 4-5, the percentage of cases observed during quiet, moderate, and disturbed period are ∼12%, ∼11%, and ∼13% of total transmissions, respectively. Above L-shell 5, the percentage of cases observed during quiet, moderate, and disturbed period are ∼13%, ∼12%, and ∼14% of total transmissions, respectively. The percentage of SR echoes observed during disturbed times is higher than that observed during moderate times, and the percentage of SR echoes observed during moderate times is higher than that observed during quiet times for all L-shells.

2.7.1   Examples of MR echo observed at similar locations and different geomagnetic conditions
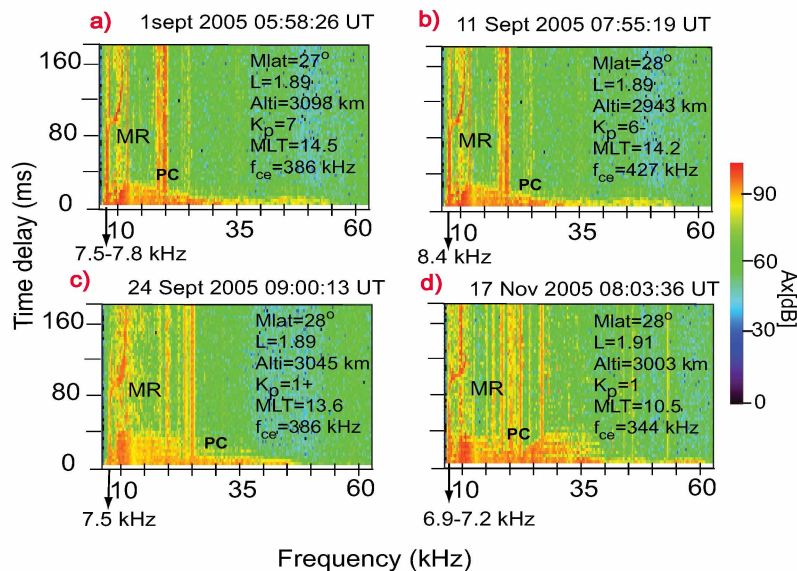
Figure 2.23   MR echoes observed at quiet (Figure c; Figure d) and disturbed (Figure a; Figure b) geomagnetic conditions at L-shell ∼1.9.

Figure 2.23 shows a set of MR echoes at similar geomagnetic locations but different geomagnetic conditions (K_p). These cases are observed at L-shell ∼1.9, altitude∼3000 km, λ=28°, and MLT∼10-14. Date and time of the cases are given at the top of the plasmagrams. For plasmagram shown in 2.23a K_p was 7 (disturbed). The f_{lhsat} (shown by the black arrow) is 7.5-7.8 kHz and the MR frequency range is 8.1-10.8 kHz. For plasmagram shown in 2.23b K_p was 6- (disturbed). The MR

range observed is 8.7 to 10.8 kHz. The f_{lhsat} is 8.4 kHz. For plasmagram 2.23c K_p was 1+ (quiet). The observed f_{lhsat} is 7.5-7.8 kHz and the MR range is 8.1-11.1 kHz. For plasmagram shown in 2.23d has K_p 1 (quiet). The f_{lhsat} resonance observed was 6.9-7.2 kHz and the MR observed range is 7.5-10.5 kHz. PC echoes and transmitter signals are seen in all the four cases.
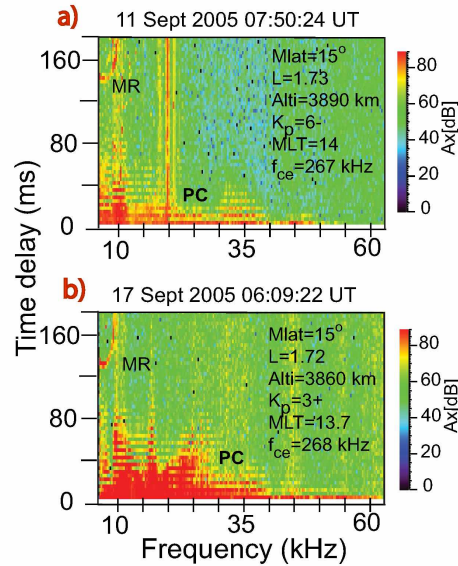
Figure 2.24 MR echoes observed at disturbed (Figure a) and moderate (Figure b) geomagnetic conditions at L-shell~1.7.

Figures 2.24a and 2.24b show another example of MR echoes observed at L-shell 1.7, MLT~14, and altitude ~3900 km, but at different geomagnetic conditions. Plasmagram in 2.24a was observed on 11 September 2005 at 07:50:24 UT and K_p for this case was 6- (disturbed). The MR echo range observed is 6.3-9.9 kHz. The second case was observed on a moderately disturbed day at K_p=3+ on 17 September 2005 at 06:09:22 UT. The range of MR echoes observed is 6.3-9.3 kHz. PC echoes are observed in both cases.

2.7.2 Examples of SR echo observed at similar locations but different geomagnetic conditions
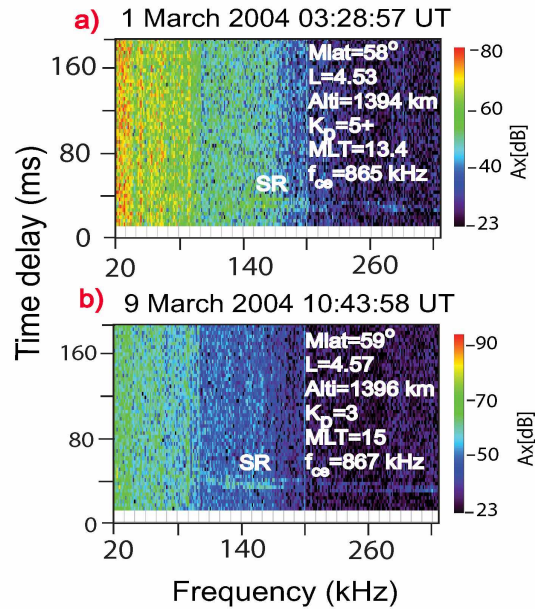
Figure 2.25 SR echoes observed at disturbed (Figure a) and moderate (Figure b) geomagnetic conditions at similar locations.

Figures 2.25a and 2.25b show examples of SR echoes observed at similar locations (L~4.5, MLT = 13, altitude~1400 km) at different geomagnetic conditions on pr#57. Case 2.25a was observed on 1 March 2004 at 03:28:57 UT at K_p=5+ (disturbed), while case 2.25b was observed on March 9 2004 at 10:43:58 UT at K_p=3 (moderate).

Figures 2.23, 2.24 show that the f_{lhsat} resonance, MR cut-offs, and time delay of the echoes do not depend on geomagnetic activity. Figure 2.25 too shows that the SR echoes observed in both cases are multipath and have similar time delay spreads (~25-35 ms at the higher frequency range). However, field line dependence of electron density can be studied during the passes of IMAGE/RPI during quiet geomagnetic conditions as well as during the whole phase of a magnetic storm. Plasma refilling and depletion along magnetic flux tubes during geomagnetic storms has a different field line dependence. Field line dependence is derived from the average electron densities measured in coarse coverage of L shells and latitudes (Gallagher et al., 2000; Goldstein et al., 2001; Denton et al., 2002, 2004, Reinisch et al., 2004). In addition, the plasma distribution may vary substantially in space and time during magnetic storms, compromising the values of statistical models. Therefore, instantaneously measuring the electron density distribution along a magnetic field line is necessary

49

in order to accurately determine the plasma density and its field line dependence along a depleted flux tube (Tu et al., 2004, 2006). Previous results have reported that, following a geomagnetic storm, the lighter ion density decreases in the plasmasphere whereas the O^+ ion density increases (Singh and Horwitz 1992). The ion density distribution from WM sounding on IMAGE/RPI can provide information about this.

2.8 Occurrence of WM echo on IMAGE/RPI with respect to solar activity:
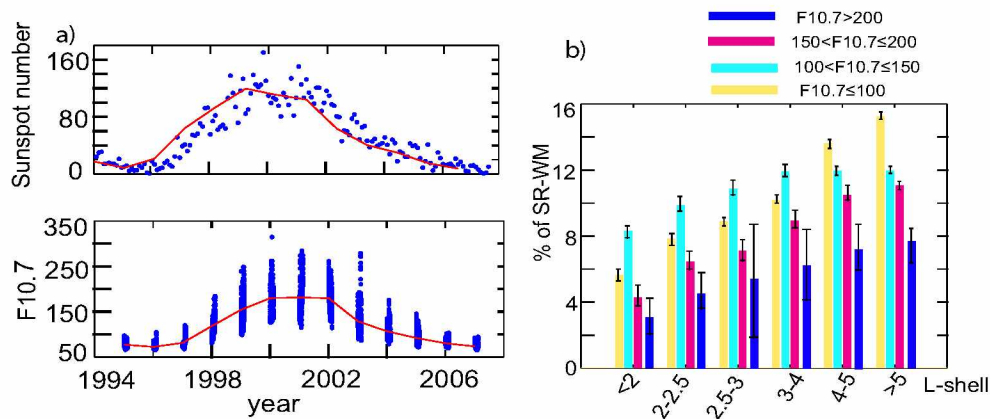
Figure 2.26 Occurrence of WM echo on IMAGE/RPI with respect to solar activity. Figure a) shows the solar activity (sunspot number and F10.7) variation during the year 1994 to 2006, figure b) shows relative percentage occurrence of SR-WM echo during the years 2000 to 2005 with respect to F10.7.

Earth's ionosphere is mainly produced via the photoionization of the upper atmosphere by solar EUV and X-ray radiation. As a result, the behavior of the ionosphere is strongly controlled by solar radiation. Variations of solar radiation are significant over different timescales, which of course will cause corresponding variations in the ionosphere (Kawamura et al., 2002; Rishbeth and Garriott, 1969; Chen et al., 2008). The 11-year solar cycle is a prominent component of the variations in solar radiation (Kane, 1992, 2003; Lean et al., 2001), which affects the ionosphere significantly. There is a nonlinear relation between daytime ionospheric parameters (foF2, plasma frequency at the F2-peak and TEC, total electron content) and solar proxies (such as F10.7 which is 10.7 cm solar radiation flux) in all seasons (Lei et al., 2005; Liu et al., 2003, 2004, 2006; Richards, 2001; Sethi et al., 2002; Su et al., 1999, Chen et al., 2008).

The 23rd solar cycle started in 1996 and ended in 2007. The solar maximum for this solar cycle occurred during year ∼2000/2001, and year 2005 was a near solar minima. IMAGE satellite period (2000-2005) covers maxima to near minima of this solar cycle. As most of the MR echoes (∼90%)

were observed in year 2005 (F10.7 varies between 70 to 120 during MR echo occurrence) due to more transmissions of pr#38, the occurrence of MR can not be compared with solar activity. The SR echoes were observed through 2000-2005, hence, their occurrence can be analyzed with respect to solar activity. Figure 2.26a's top panel shows sunspot numbers for the 23rd solar cycle. The blue dots are the daily average of the sunspot numbers for the years 1995-2007. The red curve is the monthly average of sunspot numbers for the years 1995-2007. The bottom panel of figure 2.26a) shows the variation of F10.7 over the years 1995 to 2007. The blue dots are the daily F10.7 data, while the red curve represents the average F10.7 from the years 1995 to 2007. The daily F10.7 index is given in Solar Flux Units (1 s.f.u. = 10-22 W*m-2*Hz-1).

Figure 2.26b) shows a histogram of the percentage of SR echoes occurring during the years 2000 to 2005 relative to the transmissions with respect to different L-shell ranges. During the 23rd solar cycle the F10.7 varied between 72 to 300. Yellow represents F10.7≤100 (low solar activity), cyan represents 100<F10.7≤150 (medium solar activity), magenta represents 150<F10.7≤200 (medium-high solar activity), and blue represents F10.7>200 (high solar activity). The total occurrence number of SR echoes increases with L-shell. In all the L-shell ranges, SR echoes observed for F10.7>200 have lowest occurrence percentage than other ranges of F10.7. Below L-shell 4, the maximum number of SR echoes are observed during medium solar activity; above L-shell 4, the maximum number of SR echoes are observed at low solar activity.

2.8.1   SR echo observed at similar locations but different solar activity
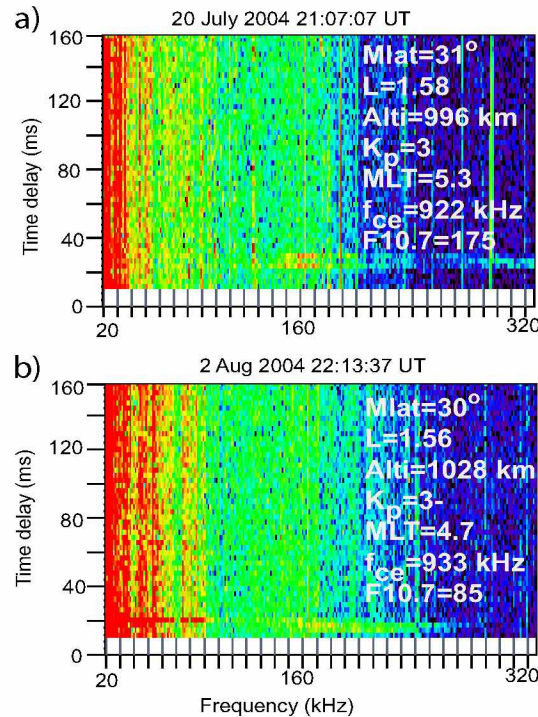
Figure 2.27 Examples of SR echo observed at similar locations but different solar activity. Figure a) shows case of SR echo with higher solar activity and b) shows case with lower solar activity.

Figure 2.27 shows an example of SR echoes observed at similar location and similar geomagnetic conditions during low and high solar activity periods. Date, time, and locations of the cases are given in the plasmagrams. Top panel case was observed at high solar activity with F10.7=175. Bottom panel case was observed at low solar activity with F10.7=85. The echo observed on the higher solar activity day has a ~10-15 ms higher time delay than the echo observed on lower solar activity day. Recent work by Chen et al., (2008), Liu et al., (2006, 2007), and Mielich and Bremer (2013) showed the increase of NmF2 (F2 peak electron density) with solar activity. This can increase the time delay of the SR echoes as it gets reflected from the Earth-ionosphere boundary. But the WM data set on IMAGE/RPI does not cover many examples of SR echoes at similar locations (MLT, Altitude, L), similar geomagnetic activity (K$_p$), and different solar conditions (year 2001-2004).

Table 2.3 Summary of example of WM echoes.

Figure number	Date and time	Types and no. of WM echoes	comment
Figure 2.9	22 Oct 2005; 20:04:42 UT	one MR and one OI-SR	Simultaneous occurrence of MR and SR at mid latitude
Figure 2.10	21 Jun 2004; 19:38:31 UT	one MR, one OI-SR and one NI-SR SR	Simultaneous occurrence of MR echo with OI-SR and NI-SR echoes at high latitude
Figure 2.11	11 Dec 2005; 01:22:10 UT	one MR and one NI-SR	Overlapping NI-SR and MR echo
Figure 2.12	1 July 2004 21:47:10 UT	one OI-SR and one NI-SR	Simultaneous observation of NI-SR and OI-SR echoes at low latitude
Figure 2.13	14 July 2004 22:51:08 UT	Two NI-SR	Simultaneous observation of NI-SR echoes at low latitude
Figure 2.14	16 Nov 2005; 03:33-03:47 UT; 17 Nov 2005 07:59-08:12 UT	MR, SR	Successive cases of MR echo and SR echoes along the IMAGE orbit
Figure 2.15	14 July 2004, 22:42-22:57 UT	SR	Successive cases of SR echoes along IMAGE orbit
Figure 2.16	07 Sept 2005; 08 Sept 2005; 30 Nov 2005	MR, SR	MR echo observed near the plasmapause
Figure 2.17	23 Sept 2005 05:01:14 UT; 28 Oct 2005 04:21:40 UT	SR	SR echo observed near the plasmapause
Figure 2.23	1 Sept 2005 05:58:26 UT; 11 Sept 2005 07:55:19 UT; 24 Sept 2005, 09:00:13 UT, 17 Nov 2005, 08:03:36 UT	MR	MR echo observed at different geomagnetic conditions
Figure 2.24	11 Sept 2005 07:50:24 UT; 17 Sept 2005 06:09:22 UT	MR	MR echo observed at different geomagnetic conditions
Figure 2.25	1 Mar 2005 03:28:57 UT; 9 Mar 2004 10:43:58 UT	SR	SR echo observed at different geomagnetic conditions
Figure 2.27	20 Jul 2004 21:07:07 UT; 2 Aug 2004 22:13:37 UT	SR	SR echo observed at different solar activity conditions

Chapter 3   Method of electron and ion density determination from WM echoes

This chapter discusses important tools to analyze and interpret the observations of whistler mode echoes on the IMAGE/RPI satellite that are discussed in the previous chapter. Topics included are: cold plasma wave mode, diffusive equilibrium density model, Stanford two dimensional ray tracing simulation, the method developed by Sonwalkar et al., (2011b) for determining electron and ion densities from WM echoes, and tools developed as a part of this thesis project.

3.1   Cold plasma wave theory

In linear theory, solutions to Maxwell's equations are obtained for plane waves of the form

$$\vec{E} = \vec{E_0} \cdot e^{[j(\vec{\mathbf{k}} \cdot \vec{r} - \omega t)]} \tag{3.1}$$

where, $\vec{E_0}$, $\vec{\mathbf{k}}$, $\vec{r}$, and ω, are the wave polarization, wave normal vector, position vector, and angular frequency ($\omega = 2\pi f$, f is the frequency of the wave), respectively. As a first approximation, the magnetospheric plasma is considered to be made up of cold plasma consisting of electrons and ions with zero temperature. It is also assumed that the plasma is homogeneous and of infinite extent. The plasma parameters that determine the nature of the solution in this case are: electron (or plasma) density (N_e), electron mass (m_e), electron charge e, ion masses (m_i), ion charges (e_i), ion composition (relative abundance of various ion species), and the ambient geomagnetic field, B_o. For propagation in warm or thermal plasma, the temperatures of the the electrons and ions also have to be taken into account. Figure 3.1 shows the geometry representing the angle between the ambient geomagnetic field B_o, and the wave normal vector k is called the wave normal angle θ. The refractive index (μ) of a wave is defined as:

$$\mu = \frac{c|\vec{\mathbf{k}}|}{\omega} \tag{3.2}$$

where c is the velocity of light. The phase velocity from comparison of equation 3.1 and 3.2 is v_p = (ω/k), the wave normal vector k can be written in terms of the refractive index μ as follows:
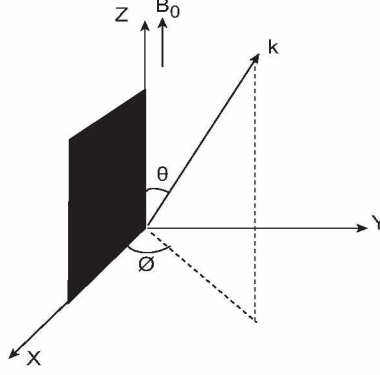
Figure 3.1 Geometry showing wave propagation in Earth's magnetosphere.

$$\vec{\mathbf{k}} = \frac{\omega \mu}{c} \vec{u}(\theta, \phi) \tag{3.3}$$

where $\vec{u}(\theta, \phi)$ is the unit vector in the direction of the wave normal vector. The equation showing the relation between k and ω is called the dispersion relation.

The solution to Maxwell's equation for a plane wave in a cold magnetoplasma is obtained in terms of general expression for the wave refractive index (Stix, 1962; Sonwalkar, 1995; Li, 2004).

$$A\mu^4 - B\mu^2 + C = 0 \tag{3.4}$$

where

$$A = S \sin^2 \theta + P \cos^2 \theta \tag{3.5}$$

$$B = RL \sin^2 \theta + PS(1 + \cos^2 \theta) \tag{3.6}$$

$$C = PRL \tag{3.7}$$

The quantities R (for right), L (for left), S (for sum), D (for difference) and P (for plasma) are defined in terms of the characteristic plasma frequency, ω_p , and the gyrofrequency ω_h. These frequencies are determined by the electron density (Ne), ion species (mass m_i and density N_i), and the ambient magnetic field strength (B).

The formulas for ω_p and ω_h are given as:

$$\omega_p = \sqrt{\frac{N_e e^2}{m_e \epsilon_0}} \tag{3.8}$$

$$\omega_h = \frac{|e|B}{m_i} \tag{3.9}$$

where ϵ_{o} is the permittivity of free space or electric constant.

$$R = 1 - \sum_k \frac{\omega_{pk}^2}{\omega^2} \left(\frac{\omega}{\omega + \epsilon_k \omega_{hk}} \right) \tag{3.10}$$

$$L = 1 - \sum_k \frac{\omega_{pk}^2}{\omega^2} \left(\frac{\omega}{\omega - \epsilon_k \omega_{hk}} \right) \tag{3.11}$$

$$S = \frac{1}{2}(R + L) \tag{3.12}$$

$$D = \frac{1}{2}(R - L) \tag{3.13}$$

$$P = 1 - \sum_k \frac{\omega_{pk}^2}{\omega^2} \tag{3.14}$$

where ω_{pk} is the plasma frequency of species k, ω_{hk} is the gyro frequency of species k, and ϵ_{k} is +1 for positive ions and -1 for electrons and negative ions.

An alternative expression for the refractive index is given by:

$$tan^2\theta = \frac{-P(\mu^2 - R)(\mu^2 - L)}{(S\mu^2 - RL)(\mu^2 - P)} \tag{3.15}$$

From Equation 3.2 we note that for a given set of plasma parameters, wave frequency and wave normal direction, four solutions exist for the value of the wave refractive index. Each of the four solutions represents a unique wave mode. Because of the ambient magnetic field, the magnetospheric plasma is anisotropic, and therefore the refractive index for each mode is a function of wave frequency as well as wave normal vector direction. The refractive index for the whistler mode is always a positive real number greater than 1, corresponding to propagation at phase velocities less than the speed of light. The refractive index expression for whistler mode at a frequency ω is given as (Helliwell, 1965):

$$\mu^2 = 1 + \frac{\omega_p^2}{\omega(\omega_h cos\theta - \omega)} \tag{3.16}$$

3.2 Dipole geomagnetic field model

Earth's magnetic field extends from its interior and interacts with charged particles from the solar wind. It can be approximately compared to the field of a bar magnet dipole tilted at an of angle $\sim 10°$ with respect to Earth's rotational axis. Solar wind interacts with Earth's magnetic field and distorts it; however, close to Earth's surface it can still be considered a dipole field. The dipole model is a good approximation for lower altitudes and most of the WM echoes are observed below

57
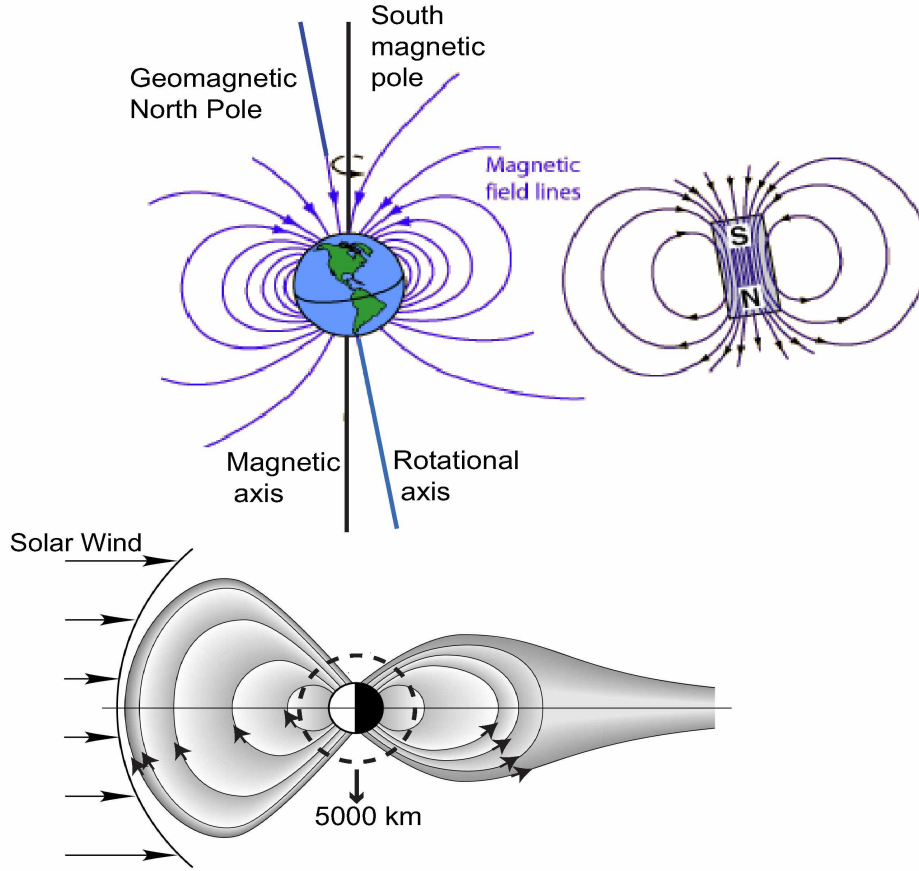
Figure 3.2 Schematic representation of Earth's dipole magnetic field: Top figure shows the schematic representation of Earth's dipole magnetic field along with its magnetic axis, rotational axis in comparison with the magnetic field of a dipole. Bottom figure shows the interaction of the Earth's magnetic field with solar wind, the magnetic field is still in dipolar shape at low altitude (∼5000km) (Courtesy:http://hyperphysics.phy-astr.gsu.edu/hbase/magnetic/magearth.html).

5000 km inside the plasmasphere. The expressions for the radial and azimuthal components of the Earth's magnetic field are given as:

$$B_R = -2B_0(\frac{R_e}{R})^3 sin\lambda \tag{3.17}$$

$$B_\theta = -B_0(\frac{R_e}{R})^3 cos\lambda \tag{3.18}$$

$$|B| = B_0(\frac{R_e}{R})^3 \sqrt{1 + 3sin^2\lambda} \tag{3.19}$$

where B_o is the mean value of the magnetic field at the magnetic equator on the Earth's surface, (typically $B_o = 3.12 \times 10^{-5}$T), R_e) is the radius of the Earth, r is the radial distance from the center

of the Earth. λ is the azimuth measured from the north magnetic pole, and $|B|$ is the total magnetic field. The equation of a dipole field line can be written as:

$$R = R_e L sin^2 \lambda \qquad (3.20)$$

Using the magnetic field Equation 3.19 the gyrofrequency at any point on Earth's surface is given as:

$$f_{ce} = f_{ce,Eq}(\frac{R_e^3}{R^3})\sqrt{1 + 3sin^2\lambda} \qquad (3.21)$$

where $f_{ce,Eq}$ is the gyrofrequency at the equator.

3.3 Diffusive equilibrium (DE) density model and its limitations

The plasma diffusion process plays an important role in the formation of the F2 peak of the ionosphere. Since diffusion processes become more important with decreasing atmospheric density, it is reasonable to expect that the topside ionosphere could be approached in terms of diffusive equilibrium (Rishbeth, 1967; Johnson, 1960; Angerami and Thomas, 1964; Bauer, 1969). The diffusive equilibrium model is an ideal situation representing a limiting case of the continuity equation for charged particles in the ionosphere. The density scale height of this distribution depends on the mean ionic mass (i.e., ion composition) and the electron and ion temperatures and their gradients. It is assumed that at thermal equilibrium, electron temperature (T_e) and ion temperature (T_i) are equal. The diffusive equilibrium model represents the plasma density (and of the major ions) distribution reasonably well, but the distribution of the minor ions in the topside ionosphere may still have the effect of chemical and transport processes. Because of the magnetic field's control of plasma diffusion, equilibrium conditions apply along magnetic field lines. At high latitudes ($>60°$), diffusive equilibrium applies directly to vertical density profiles. Beyond the plasmasphere trough, where local plasma density is very low and can be considered as almost collisionless, leading to an ion-exosphere distribution, which decays with altitude much faster than a diffusive equilibrium distribution. Thus the diffusive equilibrium model is not a good approximation for high latitude cases. Another drawback of this model is that at the same electron and ion temperature, a diffusive equilibrium distribution with a constant scale height (due to same temperature) can not be considered an appropriate description of the topside ionosphere (Angerami and Thomas, 1964; Bauer, 1969). Irrespective of the plasma dynamics, the slowly

decreasing electron density distribution along Earth's magnetic field line is well approximated by DE models.

3.4   Stanford 2-D raytracing simulation code

The Stanford 2-D ray tracing program uses a Runge-Kutta/Adams routine to integrate a system of linear differential equations (Haselgrove equations (Haselgrove, 1955)) given by ray theory (Kimura, 1966) assuming slowly varying magnetospheric plasma conditions. The ray tracing technique is based on two component (ions and electrons) cold plasma theory (Stix, 1962) and is used to determine the index of refraction and to compute the ray paths using geometric optics formulations. Both group time delay and wave normal angle can be calculated along ray paths for rays injected at arbitrary latitudes and altitudes. The Stanford ray tracer employs a dipole field model, a diffusive equilibrium model for density along field lines within the plasmasphere, and an (r^{-n}) density falloff outside the plasmasphere. The dipole field model is characterized by a single assignable parameter, $f_{ce,Eq}$, the gyrofrequency at the geomagnetic equator at the Earth's surface (Inan and Bell, 1977). Reflections at the Earth-ionosphere boundary are modeled as specular reflections at a specified altitude, typically 90 km. This approach therefore falls short of providing the type of full wave treatment that would be essential for a complete analysis. The ray tracing program also neglects D region absorption, which is important in the day time and increases with frequency (Helliwell, 1965). The diffusive equilibrium model has four components including electron density Ne), and ion composition (α_i, i=1, 2, 3 for hydrogen (H^+), helium (He^+) and oxygen (O^+) ions. In this model both ions and electrons are considered at the same temperature T. There is another parameter in the model, called r_b, which is the base altitude below which the (O^+) ion dominates and above which (H^+) dominates. The lower ionosphere is characterized by scale height (H_{bot}). The plasmapause is characterized by its magnetic shell parameter L_p, width (W_p), and density fall off outside the knee (n). The details of this program are described in Burtis (1974). The raytracing simulation covered in this thesis is confined to two dimensions. Three dimensions would have included the effect of longitudinal variation on propagation. Three dimensional ray tracing studies at 15 kHz by Sonwalkar et al., (1994) have discussed that in a smooth magnetosphere, rays injected in the magnetic meridional plane spread about $5-10°$ in longitude and those injected in the plane normal to the magnetic meridional plane spread about 30° in longitude (Sonwalkar et al., 2011b). The expression of f_{lh} in terms of the f_{pe}, and f_{ce} can be written as:

$$\frac{1}{f_{lh}^2} = \left(\frac{m_p}{m_e}\right)\left(\frac{1}{f_{ce}^2} + \frac{1}{f_{pe}^2}\right) \tag{3.22}$$

where $\frac{m_p}{m_e} \approx 1836$ is the ratio of the proton mass to electron mass.

The ion effective mass (m_{eff}) is defined as:

$$\frac{1}{m_{eff}} = \frac{\alpha_{H+}}{1} + \frac{\alpha_{He+}}{4} + \frac{\alpha_{0+}}{16} \tag{3.23}$$

where $\alpha_H^+ = N_H^+/N_e$, $\alpha_{He}^+ = N_{He}^+/N_e$ and $\alpha_O^+ = N_O^+/N_e$ are the fractional ion abundances and N_e, N_H^+, N_{He}^+, and N_O^+ are the number density for electron and ions, respectively. Total fractional ion densities should be one, so:

$$\alpha_{H+} + \alpha_{He+} + \alpha_{O+} = 1 \tag{3.24}$$

The electron density $N_e(r, L)$ (r is the geocentric distance (in km) and L is the L-shell of the point where the density is calculated) at any point depends on N_b (reference electron density at the base of the diffusive equilibrium model inside the plasmasphere), and N_{DE} (factor due to the diffusive equilibrium model) and is given by (Sonwalkar et al., 2011b):

$$N_e(r, L) = N_b N_{DE}(r) N_{LI}(r) N_{PL}(r, L) \tag{3.25}$$

The expression for N_{DE} is given as:

$$N_{DE}(r) = \sqrt{\left[\sum_{i=1}^{3} \alpha_i e^{\frac{(r-r_b)}{H_i}}\right]} \tag{3.26}$$

where r_b is the geocentric distance in km at the base of the diffusive equilibrium model; α_i is the relative ion composition at r_b, where i = 1, 2, 3 represent H^+, He^+, and O^+, respectively, and $\alpha_H^+ + \alpha_{He}^+ + \alpha_O^+ = 1$ (Sonwalkar et al., 2011b).

The scale height H_i for i = 1, 2, 3 is given as

$$H_i = 1.1506(T)\left(\frac{r_b}{7370}\right)^2 \left(\frac{r}{r^b}\right)\frac{1}{4^{(i-1)}} \tag{3.27}$$

where T is the temperature at the base of the diffusive equilibrium model.

N_{LI} is the factor due to the lower ionosphere and is given as:

$$N_{LI}(r) = 1 - e^{-\left(\frac{r-r_0}{H_{Bot}}\right)^2} \tag{3.28}$$

61

where r_o is the geocentric distance in km to the level of the bottom of the ionosphere, and H_{bot} is the scale height of the bottom of the ionosphere.

N_{PL} is the factor due to the plasmapause and L_P is the location of the plasmapause. This factor is unity for $L \leq L_P$. For $L > L_P$, (Sonwalkar et al., 2011b):

$$N_{PL}(r, L) = e^{-\frac{(L-L_p)^2}{(W_p)}} + \left(1 - e^{-\frac{(L-L_p)^2}{(W_p)}}\right) \left(\frac{r_c}{r}\right)^n \left(1 - \left(\frac{r_c}{r}\right)^n\right) e^{-\left(\frac{r-r_e}{H_s}\right)^2} \qquad (3.29)$$

where L is the L-value defining the particular field line, W_p is the half width (in L) of the plasmapause boundary, r_c is the geocentric distance to the level at which density outside the plasmapause field line is equal to the density inside, n is the exponent decrease outside the plasmapause, r^{-n}, and H_s is the scale height of the radial density decrease for $r \geq r_c$ and outside the plasmapause (Sonwalkar et al., 2011b).

The ion densities are given by:

$$N_i = N_e \frac{\alpha_i e^{\frac{-(r-r_b)}{H_i}}}{\sum_{i=1}^{3} \alpha_i e^{\frac{-(r-r_b)}{H_i}}} \qquad (3.30)$$

where N_e, $N_1 = N_H^+$, $N_2 = N_{He}^+$, $N_3 = N_O^+$ are electron, hydrogen, helium, and oxygen ion densities, respectively.

$$N_e = N_H^+ + N_{He}^+ + N_O^+ \qquad (3.31)$$

The diffusive equilibrium factor, $N_{DE}(r)$, determines the altitude variation of the relative concentration of three ions. The relative concentration of each ion as a function of altitude vary with a scale height H_i, which is proportional to T, r_b, and r, and inversely proportional to ion mass (Sonwalkar et al., 2011b).

3.5   Method for determining electron and ion density from WM cases

The methods used to determine electron and ion density from WM echoes have been discussed in Sonwalkar et al., (2011b). The steps for determining electron and ion densities from a given case of WM echoes observed with MR and OI-SR echoes, are as follows:

Step one: Measure time delays, f_{lh} resonance frequency and cutoffs of observed echoes on binbrowser with the proper settings to see the echo in the best possible way. There are cases where the MR echo is very diffuse on the X-antenna but a discrete pattern is observed on Y-antenna (example shown in Figure 2.11). In such cases, the time delays and cut-offs were measured from the Y-antenna. For some cases, echoes are best observed on combined antenna representation in

62

binbrowser. f_{ce} at the satellite location is measured from the IGRF model. $f_{ce,Eq}$ can be calculated from f_{ce}. MR echoes observed at low altitudes are accompanied by proton-cyclotron (PC) echoes. f_{ce} at the satellite location can also be determined from the time period of these PC echoes (as described in Chapter two) and can be compared with the calculated f_{ce} from the IGRF model. The dynamic spectrogram shows upper hybrid (f_{uh}) emissions. f_{pe} at the satellite location is measured from the f_{uh} emissions of the dynamic spectra corresponding to the time of echo observation. If f_{uh} emissions are not available at the time of echo observation, the f_{uh} emissions from the earlier or later times are taken for reference. The plasmapause (L_{pp}) is measured from the f_{uh} emissions. This method is described in detail in Chapter two.

Step two: Choose the input parameters of the model. If L_{pp} is not available from dynamic spectra, it is calculated from Carpenter and Anderson's (1992) model using K_p index. The width of the plasmapause, W_p, is chosen to be 0.1. We assume an $r^{-4.5}$ density variation outside the plasmasphere. Since the satellite was well inside the plasmasphere when most of the WM echoes were observed, the results are not sensitive to the values of L_{pp}, W_p, and the exponent in the r^{-n}. We start with an initial values for the diffusive equilibrium model parameters taking $r_b = 1000$ km, $T = 1800$ K, $H_{Bot} = 140$ km, $\alpha_{H+} = 0.33$, $\alpha_{He+} = 0.33$, and $\alpha_{O+} = 0.34$. These input parameters and the electron density $N_{e,sat}$ (calculated from f_{pe}) are adjusted to satisfy the measured cut-offs ($f_{lh,sat}$, $f_{lh,max1} > f_{MR,max}$). Increasing r_b or the heavier ion concentration (α_{O+}) decreases $f_{lh,max1}$ and increases foF2 (plasma density at F2 peak). Increasing of T decreases $f_{lh,max1}$ and foF2. Increasing $N_{e,sat}$ increases both $f_{lh,sat}$ and $f_{lh,max1}$.

Step three: Using the specified input parameters (in step one and two), ray tracing simulation is carried out at frequencies covering the range of frequencies of the observed MR and OI echoes. For MR echoes rays are injected at higher wave normal angle close to θ_{res}. For SR echoes rays are launched at initial wave normal angles from $0°$ to θ_{res} and the rays going below the satellite altitude reflect at the Earth-ionosphere boundary (OI-SR, NI-SR) depending on their frequency and the initial wave normal angle. NI-SR echoes have lower wave normal angles. The rays at given frequency should pass either side of the satellite while reflecting back is considered as the criteria for echo formation for both MR and SR echoes. The ray tracing calculations provide time delay (tg) as a function of frequency for the MR, OI, and NI echoes. The calculated time delays are compared with the measured ones (in cases with no NI-SR echo, the time delay for the NI-SR echo is calculated along with OI-SR echo's time delay with the model matching the time delay for the OI-SR echo). If the calculated and measured delays do not agree, the process is repeated with

different input parameters until agreement is found within experimental uncertainty of observed cut-offs and time delays. At any given frequency, two thirds of the MR echo time delay is gathered around the region where $f_{lh} \geq f$ and the refractive index surface is closed (near the reflection region of the MR echo). The time delays of MR echoes depend on both Ne and m_{eff}. Both OI- and NI-SR echoes have dependence on the electron density at the F2 peak, however, OI-SR echoes gather a big portion of their time delay near $R_{flh,max1}$ (altitude corresponding to $f_{lh,max1}$) and near R_{F2} (F2 peak altitude). NI-SR echoes gather almost half of their time delay above $f_{lh,max1}$ altitude and about half below. NI-SR echoes propagate at low wave normal angles compared to OI-SR echoes and deviate from the satellite field line.

These steps are shown in a flow diagram in figure 3.3
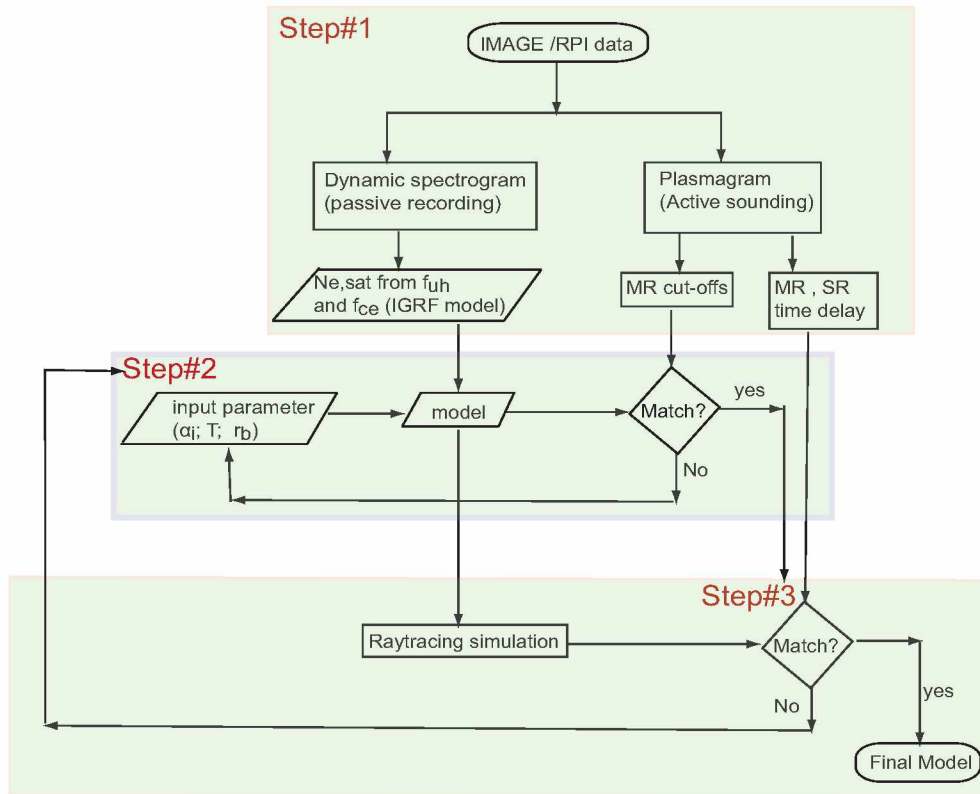
Figure 3.3 Flow diagram showing the methods for electron and ion density determination. Step#1 is for measurement from the data, Step#2 is for finding the suitable model, and Step#3 is for raytracing simulations with the model found in Step#2.

Table 3.1 Input parameters for raytracing simulation of 6 December 2005, 01:27:16 UT case.

Ne,sat	α_{H^+}	α_{He^+}	α_{O^+}	r_b	T	H_{bot}	$f_{ce,Eq}$
5256 /cc	0.739	0.039	0.222	990 km	1568 K	170 km	811 kHz
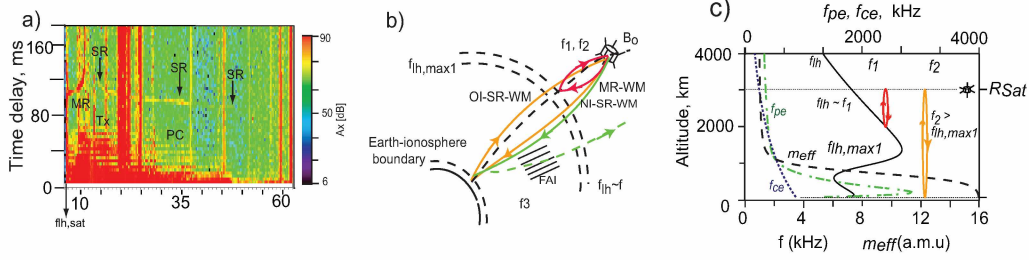
Figure 3.4 6 December 2005 07:27:16 UT case. a) Plasmagram showing observed MR and OI-SR echoes, b) schematic showing the echo formation, c) plasma parameters along satellite L-shell from the model satisfying the observed time delay in the plasmagram.

Figure 3.4 shows the case of 6 December 2005 07:27:16 UT with discrete MR and OI-SR echoes. The representation of raytracing simulation result of this case here is similar to 22 October 2005, 20:04:42 UT case included in Sonwalkar et al., (2011b). MR $\sim$(7.2-11.1 kHz) and OI-SR $\sim$(14.4-48.3 kHz) echoes were observed with time delay dispersion ranging from $\sim$100-170 ms and $\sim$110-90 ms, respectively. From the observed MR and OI echoes we measured $f_{lh,res} = f_{lh,sat} = 6.6$-6.9 kHz, $f_{MR,min} = 7.2$ kHz, $f_{MR,max} = 11.1$ kHz, and $f_{OI,min} \geq 14.4$ kHz. No NI-SR echoes were observed in this case. These cut-offs and time delay measurements are considered for finding the model satisfying the observation. The input parameters of the final model are shown in Table 3.1. Figure 3.5 shows the results of the raytracing simulations from the best fit model with observations for electron and ion density distribution along Earth's magnetic field line for this case. Figure 3.5a shows the altitudinal profile of N_e (green), O^+ (cyan), He^+ (brown), and H^+ (magenta) along the satellite L-shell from the model. The green dot at $\sim$3080 km indicates the electron density at the satellite at this time from RPI passive measurements (f_{uh} emissions from dynamic spectra and f_{ce} from IGRF model). The black arrow at $\sim$839 km indicates the O^+/H^+ transition height from the model. Figure 3.5b shows the model result of different plasma parameters along the satellite L-shell. The red curve represents f_{lh}. The two black vertical dashed lines at $\sim$3080 km indicate the $f_{lh,sat}$ resonance (6.6-6.9 kHz; shown with uncertainty of $\pm$0.15 kHz, so plotted for the range 6.45-7.05 kHz) observed on the plasmagram. The dotted vertical line at 11.25 kHz is the $f_{MR,max}$ frequency (upper cut-off of MR is 11.1 kHz; shown with uncertainty of 0.15 kHz). $f_{lh,max1}$ calculated from the model is 12.02 kHz. The black curve is for effective ion mass (m_{eff}), which is $\sim$1 at altitude above 2000 km. The blue curve is the dipole model f_{ce} along the satellite L-shell. The green curve is for f_{pe}. The model has foF2 (plasma frequency at F2 peak) $\sim$3.26 MHz. Figure 3.5c shows the plot of MR and NI-SR echo ray paths on Earth's meridional plane for the frequency 7.2 kHz (no NI-SR echo is observed). L-shell 1.88 (satellite L-shell) is drawn to show that MR echoes travel

65
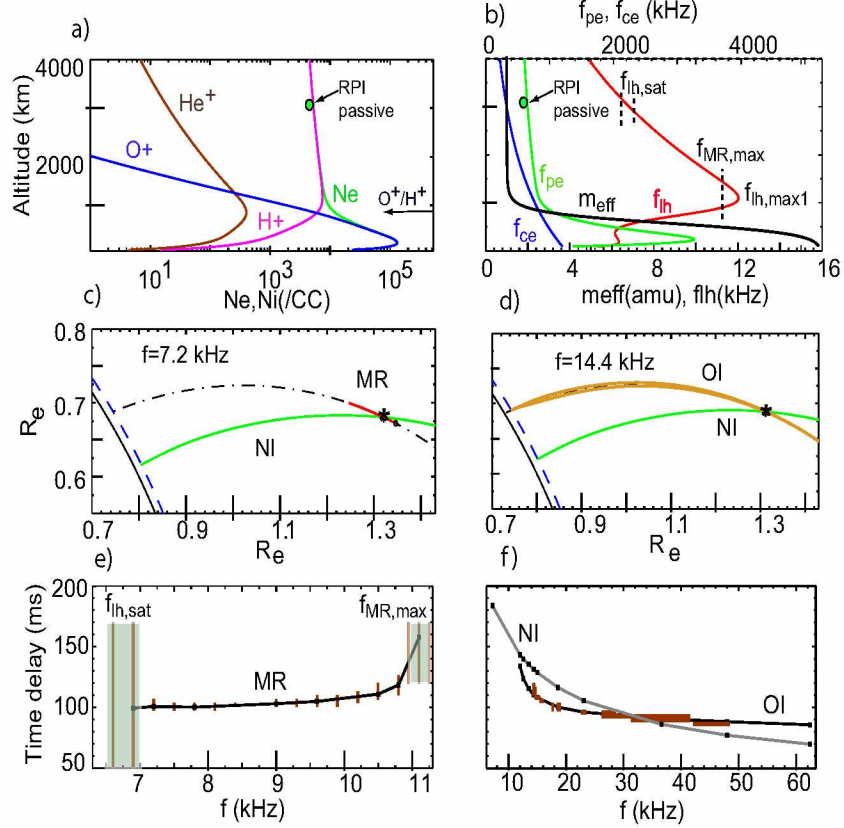
Figure 3.5 Raytracing results of 6 December 2005 07:27:16 UT case study. a) Altitudinal profile for Ne, O^+, H^+, He^+ along satellite L-shell. b) Altitudinal profile for plasma parameters along satellite L-shell. c) Ray path plot on magnetic meridional plane for MR with NI-SR echo at 7.2 kHz. d) Raypath plot on magnetic meridional plane for OI-SR with NI-SR echo at 14.4 kHz. e) Time delay plot of observed and calculated MR echo. f) Time delay plot of observed, calculated OI-SR echo and calculated NI-SR echo.

along the L-shell whereas NI-SR rays deviate more than 0.14 of L. Figure 3.5d shows the ray paths for OI-SR and NI-SR echoes on Earth's meridional plane at frequency 14.4 kHz (no NI-SR echo is seen). OI-SR travels along the Earth's L-shell, and NI-SR deviates from the satellite L-shell. Figure 3.5e shows the plot of the MR echo time delay calculated from rayracing simulation using the model shown in Figure 3.5a, b over the measured time delay on the plasmagram. The light blue highlighted regions are the range of $f_{lh,res}$ and the upper cut-off of MR, respectively, with experimental uncertainty. The next Figure 3.5f plots the NI-SR and OI-SR time delay calculated from raytracing simulations over the measured OI-SR time delays from the plasmagram. No NI-SR echo is seen on the plasmagram for this case, but we get NI-SR echoes from the raytracing simulations. It is seen from the results that the calculated time delay and cut-offs of both types of echoes match very well with those of the observed echoes.

3.6 Newly developed analysis tools

There are two very important tools developed as a part of this thesis project. These two tools are discussed briefly in this section.

3.6.1 Incorporating the Stanford 2D raytracing FORTRAN simulation code in MATLAB

The Stanford 2D raytracing FORTRAN simulation code is run through MEX-file from MATLAB on a stand-alone PC. MEX stands for MATLAB executable. These files can be written in either C or FORTRAN language as subroutines to be called from MATLAB as if they were built-in functions. It is a better way to connect the FORTRAN code with MATLAB without managing any parameters. Ray path plotting and other sorts of data analysis were done on MATLAB after transferring the output files. Running the FORTRAN code from MATLAB through MEX-files made it very convenient in terms of the time required. Also, the whole analysis including the raytracing simulations can be done from a single MATLAB script file. The MEX-file connects MATLAB with FORTRAN without exchanging the input output variables (the MATLAB MEX-file is called without any input/output argument).

3.6.2 Application of graphical user interface (GUI) with MATLAB for visualizing the input and output of Stanford 2D raytracing simulation code

A graphical user interface (GUI) on MATLAB was developed for the ray parameters of the Stanford 2D tracing simulation code along the ray path by clicking on any point of the ray. A GUI is a pictorial interface to a program. A good and consistent GUI can make programs easier to use by providing them with a consistent appearance. Component, figure, and callback are the three principal elements to create a MATLAB graphical user interface. With the help of MATLAB GUI and handle graphics, the data cursormode is activated and display window is set. The function handle is given to a function ('labeldata') with all the required parameters to display on the path of the ray in Earth's meridional plane. Then, by clicking it set, the event object position corresponding to the clicking index displays the parameters of this index in the display window. Enabling data cursormode with setting display style and figure handle gives a very quick and efficient way to understand ray propagation. The output of the GUI is shown in the Figure 3.6
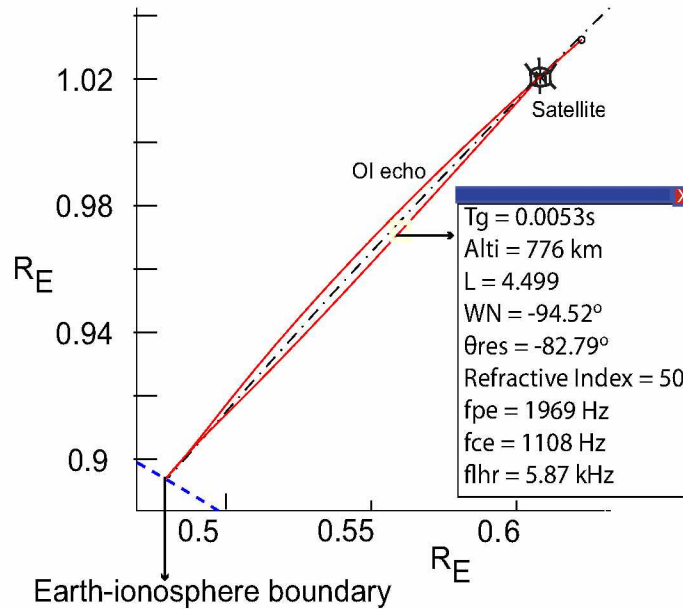
Figure 3.6 Ray parameters of the OI-SR echo ray path in the inset of the figure using MATLAB GUI. The small pop-up window (inset) is activated up by clicking any point on the ray path.

3.7 Electron and ion density data used from other satellites, ionosonde stations and models for comparison

The results of the analyses included in Chapter four will be compared to other sources of data from in-situ measurements by satellites, ionosonde measurements, and empirical models. In this section those different data sources are discussed briefly.

3.7.1 DMSP satellite

The Defense Meteorological Satellite Program (DMSP) is a series of polar orbiting satellites at an altitude of about 840 km operated by the United States Department of Defense (DOD). The spacecraft is in a 96 degree inclination orbits. The first DMSP spacecraft was launched January 19, 1965 and the DOD keeps at least two in operation at any one time. DMSP-F13 is in a roughly dawn-dusk orientation while DMSP-F12, DMSP-F14, and DMSP-F15 are all in a 0930-2130 local time orientation. Starting with DMSP-F8 (launched in 1987), the DMSP spacecraft carried the Special Sensors-Ions, Electrons, and Scintillation (SSIES) for thermal plasma analysis package (built by the Center for Space Sciences at the University of Texas at Dallas). This thermal plasma analysis package includes a Retarding Potential Analyzer (RPA), an Ion Drift Meter (IDM), a scintillation meter, and a Langmuir probe instrument. RPA can measure the thermal ion flow speed in the

direction of the spacecraft (v_x), the ion temperature (T_i), and the fractional composition of the plasma (fH^+, fHe^+, and fO^+). The main drawback of RPA is in the region of relatively high (more than 15%) concentration of light ions (H^+ and He^+) in the plasma. The RPA and IDM were designed to operate in a O^+ dominant environment, therefore, if the composition of light ions increases, the quality of the data is degraded. It takes 4 seconds ($\sim$28-30 km) for the RPA to complete a single sweep and for the analysis it is assumed that the thermal plasma is uniform during that period. However, if there is a significant variation in the plasma either in density or velocity on a scale smaller than this, then the current variation is erratic during the sweep and data are not suitable for analysis. This happens often in the auroral region. In these cases, the RPA data flag is set to 3 (bad). The quality flag for the IDM is based in part on the RPA data, the associated IDM quality flag where RPA data flag is 3, is set to 4 (undetermined). The DMSP satellite data are available at http://cindispace.utdallas.edu/DMSP/.

3.7.2 CHAMP satellite

CHAMP (CHAllenging Minisatellite Payload) is a German small satellite mission for geoscientific and atmospheric research and applications, managed by GFZ (Geo Forschungs Zentrum). It was launched on July 15 2000 into a circular, near polar orbit (87.3 degrees inclination) with an initial altitude of 456 km. By the end of 2009, it had decreased to 310 km. The local time of the orbit changes by 1 hour in 11 days, requiring about 130 days for covering all local times. CHAMP completed its mission and re-entered the Earth's atmosphere on 19 September 2010 after 10 years. It had highly precise, multifunctional, and complementary payload instruments (magnetometer, accelerometer, star sensor, GPS receiver, laser retro reflector, and ion drift meter). The Planar Langmuir Probe (PLP) on board the satellite took in-situ measurements of the electron density. The PLP voltage was swept for 1 sec in every 15 sec typically between -2.5 V and +2.5 V. By interpreting the measured current/voltage characteristic the plasma parameters can be determined. An error of 0.1 V in PLP was equivalent to an along-track velocity of 75 m/s. The PLP was designed to measure currents drawn from the ambient plasma down to 5 nA. The data are available at http://isdc.gfz-potsdam.de/

3.7.3 Alouette 2 satellite

Alouette 2 was a small ionospheric observatory launched on 29 November 1965, into an elliptical orbit (500-3000 km) with an inclination of 79.8 degrees. The life time of the satellite was 10 years

and it was terminated on August 1 1975. Its payload included a topside sounder, a VLF receiver, an energetic particles experiment, a cosmic noise experiment, and the Cylindrical Electrostatic Probe (CEP) experiment. The topside Sweep-Frequency Sounder measured the electron density distribution in the ionosphere by measuring the time delay between the emission and return of radio pulses. The data from Alouette 2 is very rich in information about the topside region of the ionosphere. This dissertation uses topside sounder data from Alouette for comparison of results. This data is available at

http://omniweb.gsfc.nasa.gov/ftpbrowser/atmoweb.html

3.7.4 ISIS satellite

ISIS-1 (International Satellites for Ionospheric Studies) was launched on 30 January 1969 into an elliptical orbit (500-3500 km) with an inclination of 88.4 degrees. ISIS 1 operations were terminated on March 9 1984. Its payload included sweep- and fixed-frequency ionosondes, a VLF receiver, energetic and soft particle detectors, an ion mass spectrometer, an electrostatic analyzer, a beacon transmitter, a cosmic noise experiment, and the Cylindrical Electrostatic Probe (CEP).

ISIS-2 was launched on 1st April 1971 into a circular orbit at about 1400 km with an inclination of 88.1 degrees. Its payload included sweep- and fixed-frequency ionosondes, a VLF receiver, energetic and soft particle detectors, an ion mass spectrometer, a retarding potential analyzer, a radio beacon, a cosmic radio noise experiment, photometers (3914, 5577, and 6300 Angstrom) and the CEP. The ISIS program spawned numerous scientific papers. Scientists learned about the physical processes of the upper atmosphere and ionosphere: densities, temperatures, magnetic field strengths, and ionospheric structures, as well as charge, density and energy of energetic particles.

The data for ISIS-1, 2 are available at

http://omniweb.gsfc.nasa.gov/ftpbrowser/atmoweb.html

3.7.5 OGO-6 satellite

Orbiting Geophysical Observatory (OGO) satellites refers to six satellites launched by the United States that were in operational mode from 1964 to 1972 to study Earth's magnetosphere. OGO-6 was a lower polar orbit satellite, which carried a Bennett Ion Mass Spectrometer (BIMS) experiment for the time period from June 12 1969 to December 31 1970. The instrument measures the ion densities of seven ion species (H^+, He^+, N^+, O^+, N_2^+, NO^+, O_2^+) at an altitude range of $\sim$400-1100 km. The data can be found at

http://omniweb.gsfc.nasa.gov/ftpbrowser/atmoweb.html.

3.7.6 AE satellites

The Atmosphere Explorer C spacecraft was launched in 1973 with orbit inclination of 68°. The Atmosphere Explorer D and E were launched in 1975 with 90° and 19.7° of orbit inclination respectively. All three satellites were intended to be placed in initial orbits with perigees near 150 km and apogees of 3000 to 4000 km. These satellites carried Retarding Potential Analyzer (RPA) and Ion Drift Meters (IDM). Atmosphere Explorers (C, D, and E) were capable of dipping into the atmosphere, provided significant measurements for studying composition and processes within the thermosphere, such as ion and neutral composition and reaction rates, energetics of the ionized atmosphere, processes that control low energy electrons, and processes of airglow excitation. Another objective of the satellites was to provide measurements for studying the global structure and dynamics of the neutral atmosphere and ionosphere. The data for these satellites can be found at http://omniweb.gsfc.nasa.gov/ftpbrowser/atmoweb.html.

3.7.7 Ionosonde

Ionosonde is a kind of radar (high frequency transmitter) used to study the ionosphere. Ionograms are recorded tracings of reflected high frequency radio pulses generated by an ionosonde. Unique relationships exist between the sounding frequency and the ionization densities that can reflect waves of that frequency. As the sounder sweeps from lower to higher frequencies, the signal rises above the noise of commercial radio sources and records the return signal reflected from the different layers of the ionosphere. These echoes form characteristic patterns of traces that comprise the ionogram. Radio pulses travel more slowly within the ionosphere than in free space; therefore, the apparent or virtual height is recorded instead of a true height. For frequencies approaching the level of maximum plasma frequency in a layer, the virtual height tends to infinity, because the pulse must travel a finite distance at effectively zero speed. The frequencies at which this occurs are called critical frequencies. Characteristic values of virtual heights are designated as h'E, h'F, and h'F2, and so on and critical frequencies are designated as foE, foF1, and foF2, and so on (Ref:http://www.ngdc.noaa.gov/stp/iono/ionogram.html). Table 3.2 lists ionosonde stations with geophysical locations whose F2 peak values have been used for comparison in our analysis. Ionosonde station data are available at

http://spidr.ngdc.noaa.gov/spidr/dataset.do?view=ionospheric

Table 3.2 List of ionosonde stations data used for comparison.

Station code	Station name	Mlat	Mlong	L-shell
$SN437$	Osan AB	37.1	127	1.267
$PRJ18$	Puerto Rico	18.5	247.2	1.299
$TQ241$	Tashkent	41.3	69.6	1.423
$AT138$	Athens	38	23.5	1.542
$KB548$	Khabarovsk	48.5	135.1	1.665
$VT139$	San Vito	40.6	17.8	1.698
$EG931$	Eglin AFB	30.5	273.5	1.721
$EA036$	EL Arenosollo	37.1	353.3	1.744
$PA836$	PT Arguello	34.8	293.5	1.763
$DS932$	Dyess AFB	32.4	260.2	1.77
$RO041$	Rome	41.9	12.5	1.815
$RV149$	Rostov	47.2	39.7	1.849
$EB040$	Roquetes	40.8	0.5	1.878
$NS355$	Novosibirsk	54.6	83.2	2.01
$PK553$	Petropavlovsk	53	158.7	2.063
$TK356$	Tomsk	56.5	84.9	2.144
$WP937$	Wallop IS	37.9	284.5	2.242
$BC840$	Boulder	40	254.7	2.254
$BL841$	Bear Lake	41.9	291.5	2.358
$PQ052$	Pruhonice	50	14.6	2.376
$MO155$	Moscow	55.5	37.3	2.534
$DB049$	Dourbes	50.1	4.6	2.571
$TZ362$	Podkamennaya	61.6	90	2.61
$MG560$	Magadan	60	151	2.628
$MHJ45$	Millstone Hill	42.6	288.5	2.738
$RL052$	Chilton	51.5	359.4	2.851
$FF051$	Fairford	51.7	359.4	2.851
$JR055$	Juliusruh	54.6	13.4	2.918
$LD160$	Leningrad	60	30.7	3.267
$KS759$	King Salmon	58.4	203.6	3.538
$SD266$	Salekhard	66.5	66.5	3.594
$GSJ53$	Goose Bay	53.3	299.7	4.937

3.7.8 International Reference Ionosphere model

The International Reference Ionosphere (IRI) is the international standard for the specification of ionospheric densities and temperatures. It was developed and is being improved and updated by a joint working group of the International Union of Radio Science (URSI) and the Committee on Space Research (COSPAR) (Bilitza, 1990, 1998, 2001, 2011). IRI consists of different sets of models at different regions of the ionosphere and plasmasphere. Figure 3.7 shows the models used in different region of ionosphere. IRI is a global empirical model which describes the average behavior of ionospheric electron density, electron and ion temperatures and ion composition (Bilitza, 1990, 2003; Bilitza et al., 2004), and references therein). IRI predictions make use of a 12 month running average of the solar sunspot number Rz12 and of the IG12 index (IG12 is based on F2 region plasma peak frequencies measured by ionosonde stations around the world and linear regressions with respect to solar activity). IG12 is used by IRI to estimate the F2 region peak density and Rz12 is used to estimate F2 region peak altitude (Bilitza, 2001). The model has undergone various modifications/improvements over the years. The most recent version is IRI-2012, which undergoes modifications in bottomside electron density, auroral boundaries, storm time models for auroral E-regions, electron temperature and ion composition (Bilitza et al., 2014).

IRI-2012

Electron Density

D region

Friedrich & Torkar 1992 empirical model based on rocket borne wave propagation data

E region

URSI, CCIR maps

Bottomside
F region

URSI, CCIR maps for Ne; bottom side thickness (B0, B1) from Altadill, Blanch and Torta 2009 model (ABT-2009 model)

Top side

NeQuick formula based on ISIS-2, TOPIST data

Ion Density/composition

Molecular ion

DY-85 model: Danilov and Yaichnikov empirical model for molecular ion

Atomic ion

RBV-10 model: Ion Density Calculator (IDC) model (Richard et al. 2010) up to ~300 km altitude above that TTS-03 model: Triscova, Truhlik, Smilauer (2003) empirical model

Electron (Te), ion (Ti), neutral (Tn) atom temperature

Te

Truhlik et.al 2012; global empirical model for Te

Ti

Global Ti model based on all available satellite data

Tn

CIRA model (COSPAR International Reference Atmosphere)

Figure 3.7 Sets of models used by IRI-2012 for different regions and different parameters.

3.7.9 Global Core Plasma Model

The Global Core Plasma Model (GCPM) developed by Gallagher et al., (2000) provides empirically derived core plasma density and ion composition as a function of geomagnetic and solar conditions throughout the inner magnetosphere. It consists of separate models for the ionosphere, plasmasphere, plasmapause, trough, and polar cap. For plasmasphere and plasmapause, this model modified the co-efficients of Carpenter and Anderson's 1992 model based on DE1/RIMS data. In the low altitude topside region ($\sim$600 km) it uses the IRI model. For polar cap density it uses a model similar to Persoon et al., (1983). The relative concentrations of He^+ and H^+ are obtained from Craven et al., (1997) empirical formula from DE1/RIMS data during solar minima. Relative O^+ concentrations are derived from DE1/RIMS measurements by Comfort et al., (1998).

3.7.10 Ozhogin et al., (2012) Model

Ozhogin et al., (2012) developed an empirical model for electron densities covering L-shells 1.6 to 4 (within the plasmasphere) and all MLTs from IMAGE/RPI at altitudes of 2000 km and above. The model is based on the remote sensing measurements in the active mode of IMAGE/RPI. It consists of two parts: equatorial density, which decreases as a function of L-shell, and field aligned dependence on magnetic latitude or L-shell. The model does not have any dependence on magnetic local time, geomagnetic or solar activity, or season. The performance of the model is tested against the in-situ measurements by the RPI passive mode. For 76% of the measurements the relative error is found to be within 50%.

Chapter 4 Electron and ion density distribution along Earth's magnetic field line

The plasma density distribution along the magnetic field has been of great interest for a long time because it is a test bed for various theoretical models involving different physical processes of Sun-Earth interaction. The main source of the plasma is the ionosphere. The ionization rate in the ionosphere depends mainly on latitude, longitude, solar activity, and magnetospheric precipitations.

This chapter discusses raytracing simulations of 82 cases within the plasmasphere, and results for N_e and ion densities along Earth's L-shells compared with other in-situ data and models.

4.1 Magnetic meridional plane and histogram representation of the raytracing cases

Out of the 82 cases of raytracing simulations presented here, there are 62 total MR cases in the day side region in this L-shell range, of which 45 are observed simultaneously with SR echoes. In the night side, there are a total of 20 cases, of which 10 are observed with SR echoes. Figure 4.1 shows all 82 cases in the magnetic meridional plane categorized in day- and night sides. The MR echoes can provide N_e and ion densities up to the reflection altitude of the wave, where the frequency of the wave is equal to the local lower hybrid frequency (f_{lh}). The SR echoes can provide N_e up to the Earth-ionosphere boundary. Therefore, the blue lines are the L-shell of the satellite, drawn from the satellite location (red dots) up to Earth-ionosphere boundary (90 km) region where density profiles are available. L-shells 1.6, 2, 2.5, 3, and 4 are shown with red dashed lines as reference lines. Altitude 5000 km is also shown with red dashed lines. All these cases are below 5000 km. The day side region covers an MLT range of 7 to 16 and the night side region covers an MLT range of 20 to 4. There are no night side MR echoes observed in L-shell ~1.6-1.9 due to limited transmissions of frequencies suitable for MR echoes in these L-shells and altitude range because of the projection of the IMAGE orbit. These cases are in quiet to disturbed geomagnetic conditions (K_p 0+ to 7). Section 2.7 of chapter two have shown that these echoes do not show any dependence

on geomagnetic activity (K_p index). The F10.7 of these cases lies in the range of 70-120 (low solar activity).

To present those cases relative to total observed cases of MR echoes, they are shown in histograms in Figure 4.2 for the observed MR echoes and raytracing analysis cases for MR echoes in day side and night side (the same cases are plotted in the magnetic meridional plane in figure 4.1) for different L-shell ranges. The spacing of the L-shells is not uniform due to uneven distribution of echo observations. By varying the length of the L-shell range, we can have a comparable number of cases in each range. Many of the cases in these L-shell ranges are repeated in similar locations with similar tg-f (time delay-frequency) dispersions, so raytracing analysis was not carried out for all those repetitive cases.
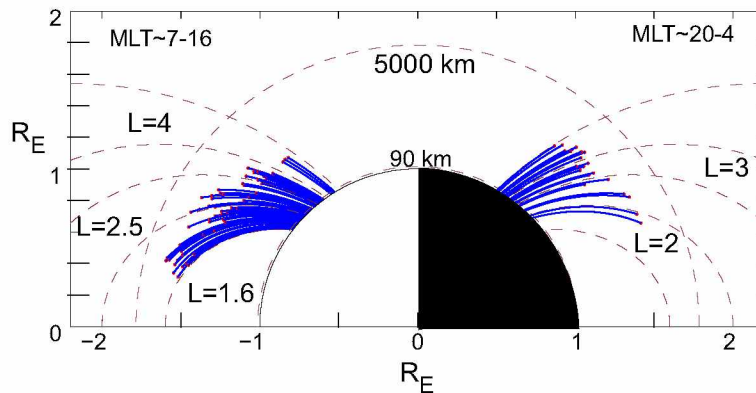
Figure 4.1 Cases analyzed below altitude 5000 km for the year 2005 are plotted in the magnetic meridional plane with field lines. Blue color represents the field lines drawn from satellite locations (red dots) to Earth-ionosphere boundary (90 km). MLT and reference field lines at L-shell 1.6, 2, 2.5, 3, 4 are also shown.

4.2 Time delay dispersion of the MR and SR echoes

The frequency-time delay dispersion characteristics of MR and SR echoes are opposite. The time delay of MR echoes increases with frequency while time delay of SR echoes decreases with frequency. The change in time delays of these echoes can provide an estimate of the change in electron density. Figure 4.3 shows time delay (normalized with altitude) of the MR and SR echoes versus frequency for day- and night side. These are all the cases shown in Figure 4.1 and 4.2 (all are observed on pr#38). The red color represents the MR echoes observed in the frequency covering 6 kHz to ~13 kHz for both day- and night side. The blue color represents the SR echoes observed in the frequency covering ~8.1 kHz to 63 kHz. For day side the group velocity for SR echoes changes by
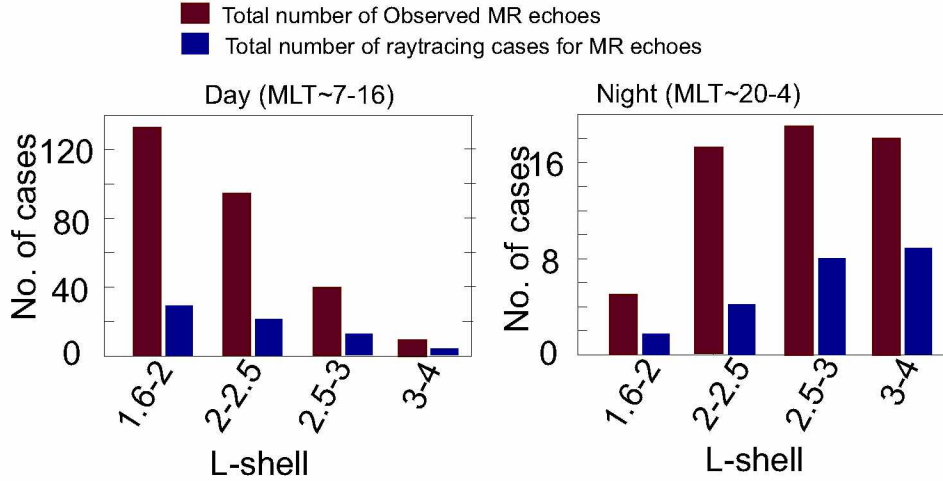
Figure 4.2 Histogram representation of the observed (black) and raytracing analyzed (grey) cases in day- and night side of the magnetosphere. These histograms are plotted as a function of L-shells below altitude 5000 km for the year 2005 (August-December).

a factor of ~5, which means electron density changes by a factor of 25 (Li, 2004). For night side, the average time delay changes by a factor of ~2 to 3, which means the electron density changes by a factor of 4 to 9. It is also seen that the average upper cut-off of the MR echo is ~1.5-2 kHz higher on the night side than day side. For both types of echoes, the average time delay for day side is higher than night side. This is better understood from the upper panel of Figure 4.4 which shows average time delays of the sets of cases at similar L-shells and altitudes but at day sides (red) and night sides (black). Plasmagrams of these cases are not shown; only date, time, and positions are given. The locations of each set of cases are plotted on the magnetic meridional plane in the bottom panel of the figure. The actual upper cut-off of the MR echoes at night side is generally 2-3 bins of frequency (each frequency bin is of 0.3 kHz in pr#38) higher than the observed since the rise in time delay near the upper cut-off is not observed. Each set of cases shows that the time delay at day side is higher than at night side, even though they are at similar L-shells and altitudes. The upper cut-off of the MR echo at night side is higher than that of day side because increased lighter ion concentration at night time causes higher f_{lhmax1} at night side.
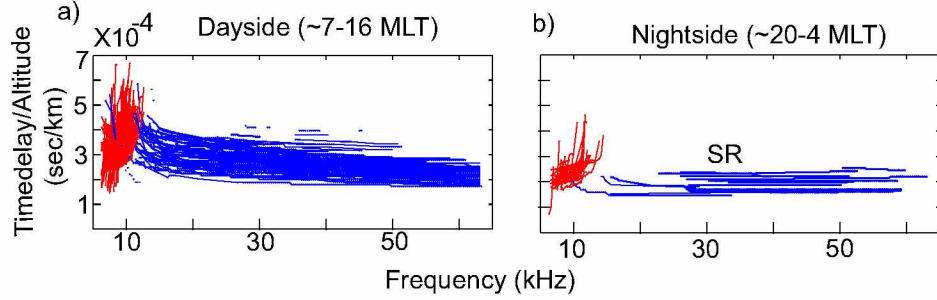
Figure 4.3 Dispersion of MR (red) and SR (blue) echoes on day side (a) and night side (b) of the magnetosphere. The variation of average time delay/altitude as a function of frequency for MR and SR echoes (August-December 2005) for which raytracing analysis have been done. The red lines show dispersion of the MR echoes (62 cases for day side and 20 cases for night side) and blue lines show the dispersion of the SR echoes (45 cases for day side and 10 cases for night side).
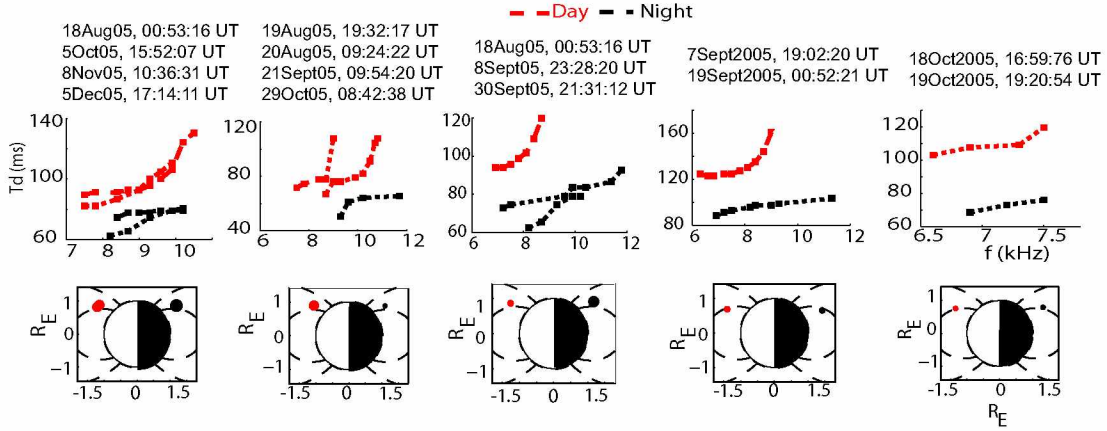
Figure 4.4 Sets of MR echo average time delay plot observed at similar location but at day and night side. First row shows average time delay plot of the sets of cases at similar L-shell and altitude but of day- (red) and night (black) sides, second row shows the locations of the cases on magnetic meridional plane.

4.3 Raytracing simulation of WM cases

This section briefly summarizes the input parameters of raytracing simulation, uncertainty in WM sounding method for ion composition measurements, and different models for the same case of different types of WM cases. For night side cases the models satisfying all the observed time delays are considered (these models have higher MR echo cut-offs than observed). The models of the cases observed only with MR echo (no SR echo) to find Ne and ion density up to Earth-ionosphere boundary are included here.

4.3.1 Input parameters for raytracing simulation
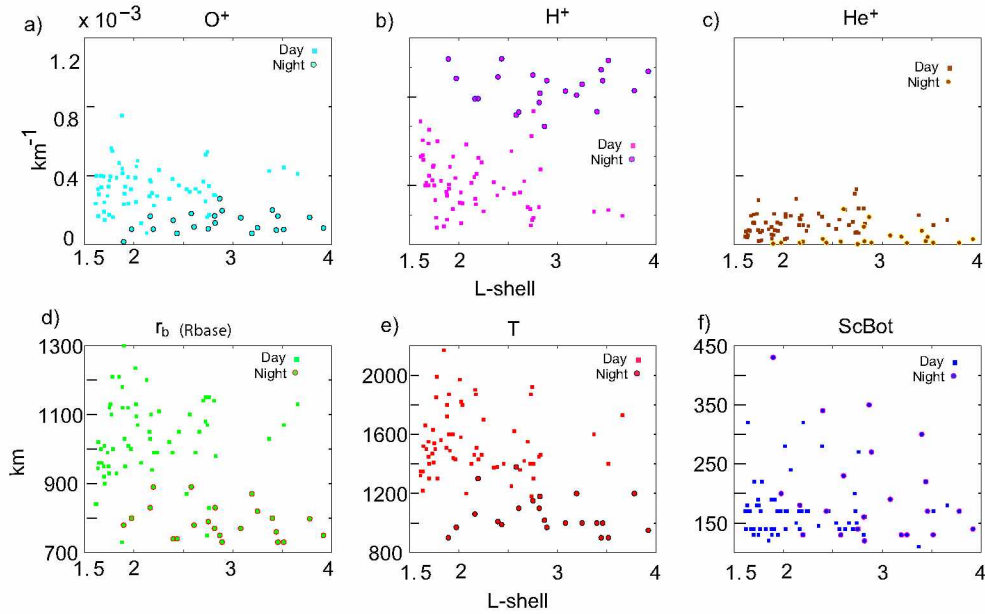
Figure 4.5 Input parameters for the raytracing simulations for day and night side of the magnetosphere. Ion densities plotted on Figure a), b), c) are normalized with respect to the R_b plotted on Figure d).

The methods described in Section 2.3.1 of Chapter three have applied to 82 cases for determination of electron density (N_e) and ion composition along the Earth's magnetic field line in the L-shell range of 1.6 to 4. The time delay measurements of each case is done carefully with the best possible settings of the plasmagram on binbrowser on the X-, Y-, or the combined antenna amplitude representations. Chapter two describes in detail how those echoes are identified. As discussed in Chapter three, finding the model satisfying the average time delay and echo cut-offs is an iterative process. The time delay for the simultaneous MR and SR echoes also should match with the same model. Electron density at the satellite location ($N_{e,sat}$), fractional ion compositions (α_{H+}, α_{He+}, α_{O+}), base altitude of diffusive equilibrium model (r_b), temperature (T), and scale height at the bottom of the ionosphere (S_{cbot}) are all adjusted for the model for the raytracing simulations to find the best matching with the observations. Figure 4.5 shows the input parameters with respect to L-shells of the raytracing simulations for day- and night side of the cases. The ion densities are given in the input file at the Rbase (r_b) altitude. They are plotted on the first row and are normalized with Rbase to determine the dependence on L-shell and MLT (day, night). The circles with colored borders represent the night side cases for all the parameters. O$^+$ density (cyan) plotted on Figure

4.5a does not show any L-shell dependence, but for most of the night side cases it is almost half of that of day side cases. H^+ ion concentration (magenta; Figure 4.5b is higher at night side than day side. The range of H^+ at day side decreases with L-shell. This pattern is not observed in night side cases. H^+ has a higher concentration than any other ions in night side. He^+ (brown; Figure 4.5c has a lower concentration than any other ions for both day and night sides and is negligible at night side as compared to other ions. Observations from the ISIS-2 and OGO satellites also reported H^+ as the dominant ion above altitude 800 km followed by O^+ and He^+ at night time (Chandra et al., 1970; Breig and Hoffman, 1975). Charge exchange is the principal chemical source and sink for H^+ in the topside ionosphere. During the day, O^+ ions created by solar photoionization are converted to H^+ through the reaction $O^+ + H \leftrightarrow H^+ + O$. H^+ ions so created can be lost locally either via the reverse reaction or by flow upward to higher altitudes. The subsequent nighttime decay of ambient O^+ is partially countered by the same reverse reaction that transforms H^+ back in to O^+. Figure 4.5d is the plot for Rbase in km. Rbase for those cases varies from $\sim$700 km to $\sim$1200 km. Temperature in K is plotted in figure 4.5e. As discussed in Chapter three, the ions and electrons have the same model temperature for a given case due to limitations of the diffusive equilibrium model. The temperature varies between $\sim$800 K and $\sim$2200 K. Scale height at the bottom of the ionosphere is plotted in Figure 4.5f. For most of the cases it is less than 200 km. The other main input parameters for the simulation are: electron density at the satellite ($N_{e,sat}$), gyro frequency at Earth's equator (f_{ceEq}), plasmapause L-shell (L_{pp}), plasmapause width (W_p), and fall-off factor (n). $N_{e,sat}$ is taken from the range of measured $f_{pe,sat}$ from f_{uh} emissions of the dynamic spectra. For cases where the measurement is not available, the simulation starts with a reference of $N_{e,sat}$ at a similar location for other cases, and then adjusts to fit the model with observations. $f_{ce,Eq}$ is calculated for each case using f_{ce} at the satellite location. f_{ce} at the satellite location is calculated using the IGRF model, then the dipole model is used to get the $f_{ce,Eq}$. $f_{ce,Eq}$ varies between $\sim$760 kHz and $\sim$1030 kHz. L_{pp} is taken from the measurements of f_{uh} from dynamic spectra. For cases for which measurements are not available, L_{pp} from Carpenter and Anderson's (1992) models are used. All these cases are within the plasmapause and W_p for all of them is taken as 0.1. The fall factor n outside the plasmapause is taken as 4.5. The precise location of the plasmapause is not very important at low altitudes because below 5000 km altitude, the plasmapause boundary merges with the background. The altitude for the Earth-ionosphere boundary is set at 90 km. The details of the input parameters for each case are included in table in Appendix of the dissertation.

4.3.2 Sample of N_e, ion composition variations along different L-shells
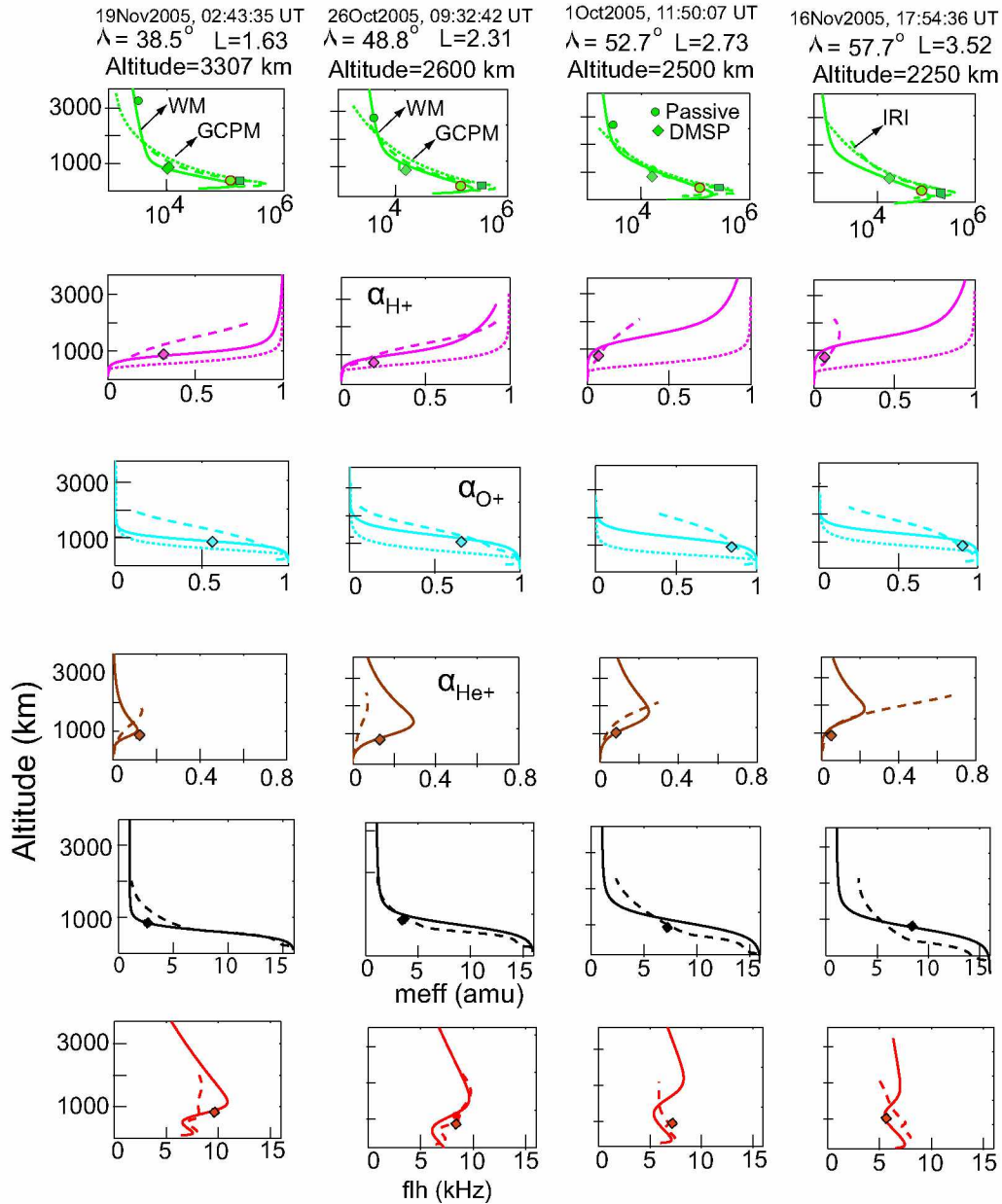
Figure 4.6 Sample of N_e, ion compositions along different L-shells. Variation of electron density (green; 1st row), ion composition (2nd, 3rd, fourth row), m_{eff} (fifth row) and f_{lh} (6th row) along geomagnetic field lines covering different invariant latitudes. along geomagnetic field lines covering different invariant latitudes. Also shown is the comparison of WM sounding results with those obtained from DMSP (shown with green square at 850 km for electrons and magenta square for H^+, cyan square for O^+ and brown square for He^+, black square for m_{eff}, red square for f_{lh}), CHAMP (shown with green square at 350 km for electrons) spacecraft in situ measurements, bottom side sounding results (ionosonde data shown with green circles at F2 peak) and IRI-2012 (green dashed curve for electrons, magenta dashed for H^+, cyan dashed for O^+ and brown dashed for He^+, black dashed for m_{eff}, red dashed for f_{lh}) and GCPM-2009 (green dotted curve for electrons, magenta dotted for H^+, cyan dotted for O^+) empirical model calculations.

In the past, people have measured field aligned plasma distribution by using statistical analyses (Persoon et al., 1983; Horwitz et al., 1990; Carpenter and Anderson, 1992; Gallagher et al., 2000; Goldstein et al., 2001; Denton et al., 2001). Large numbers of MR and SR echoes observed over wide ranges of L-shells on IMAGE/RPI have given the opportunity to deduce N_e and ion densities along those L-shells. WM sounding method for N_e and ion density measurements is different from past methods discussed in the literature. Therefore, to check the validity, the results of the WM sounding method are compared with significant past satellite measurements over the past few decades and with widely used empirical models. During dynamic magnetospheric events like geomagnetic storms, the plasma distribution may vary substantially both in space and time, compromising the value of statistical models. This dissertation does not discuss the plasma density distribution controlled by loss refilling and other dynamic processes.

Figure 4.6 shows electron density (N_e) and ion compositions of four cases along different L-shells (1.63, 1.9, 2.73, 3.52) deduced from WM sounding using the Stanford 2D raytracing simulation code. The plasmagrams of these cases are not shown, only date, time, and locations are given at the top of the Figure. The first row shows N_e variation (green) compared with in-situ N_e measurements on passive recordings on IMAGE/RPI (f_{uh} emissions on dynamic spectra at satellite altitude), DMSP ($\sim$850 km), CHAMP ($\sim$350 km), and ionosonde stations (F2 peak). The dashed line is the N_e from the IRI-2012 model which goes up to 2000 km. The dotted line is the N_e from the GCPM-2009 model (which uses the IRI model for N_e below 600 km altitude). The second row shows H^+ variation (magenta) along the L-shell, which decreases with increasing L-shell. At $\sim$850 km, it is compared with measurements from the DMSP satellite, and IRI-2012, and GCPM models. The third row (cyan) is for the O^+ variation, which increases with increase of L-shell. Fourth row (brown) is for He^+ variation in comparison with in-situ measurements from the DMSP satellite ($\sim$850 km) and the IRI-2012 model. The GCPM model contains the composition of H^+ and O^+ only. Fifth row represents m_{eff} (black lines). m_{eff} increases with L-shell for a given altitude below $\sim$1000 km due to increase of heavier ions (O^+) with L-shell. Above this altitude m_{eff} is $\sim$1 due to the dominance of H^+ ion. The sixth row shows the variation of f_{lh} (red lines) from WM sounding (solid) and compared with that of the IRI-2012 model (dashed line), and the DMSP satellite (850 km; red square with black border; calculated from N_e and ion density). f_{lhmax1} (maximum lower hybrid frequency) increases with decreasing L-shell and $R_{flhmax1}$ (altitude corresponding to f_{lhmax1}) and decreases with decreasing L-shell. This is because of an increase in m_{eff} and decrease of N_e with L-shells. f_{lh} from the DMSP data is higher towards lower L-shells. The L-shell differences

for DMSP, CHAMP and ionosonde data with respect to WM sounding are within 0.05. MLT lies within 2-4 hours and UT is within half an hour.

4.3.3 Uncertainty associated with WM sounding method

The uncertainty in this analysis could be both from the experimental technique and the method used to determine electron and ion densities. Each bin of frequency of the plasmagram for pr#38 of IMAGE/RPI has a width of 0.3 kHz. So, the frequency measurements have an uncertainty of ± 0.15 kHz. Each pulse had a duration of 3.2 ms, therefore, the time delay measurements have an uncertainty of 3.2 ms. The propagation of MR-WM rays depends on N_e and m_{eff}, not the details of ion composition (Equation 3.22, 3.23). Since we have two equations connecting three fractional ion compositions, we require a third equation. In the absence of a third equation the fractional ion compositions cannot be determined, but certain conclusions can be drawn. For example, if m_{eff} is not equal to 4.0, then either O^+ or H^+ must be present. If m_{eff} is less than 4.0, H^+ is required; if m_{eff} is greater than 4.0, O^+ is required. Hence, for a given value of m_{eff}, narrow limits can be put on the possible fractional H^+ and O^+. But He^+ has great precision (Barrington et al., 1969). Therefore, any combination of fraction of ion composition satisfying Equation 3.23, with calculated time delay matching observed time delay, can be possible estimates of m_{eff}. This leads to uncertainty in the ion composition estimates, as for a given value of m_{eff} more than one combination of ions is possible. Multiple models with different input and output parameters satisfying the observed time delays for a given case can be found. Figure 4.7 (taken from Sonwalkar et al., 2011b) shows values of m_{eff} obtained from radio sounding (black curve) in Equation (3.23) and solve it subject to the constraints given by Equation (3.24). The ranges of fractional abundances (α_i) calculated for each species are consistent with the particular values of m_{eff}. Ranges of possible ion fractions for H^+ (magenta), He^+ (brown), and O^+ (cyan) are shown. Uncertainty is minimum for H^+ and maximum for He^+. The uncertainty in He^+ is maximum when $m_{eff} = 4$. This uncertainty in ion densities gives uncertainty in transition heights (height at which lighter and heavier ion densities are equal).

From Equation 3.23 and equation 3.24 the uncertainty in O^+/H^+ transition height is given as: $1.882 \leq m_{eff} \leq 4$

and the uncertainty in $O^+/(H^++He^+)$ transition height is given as: $1.882 \leq m_{eff} \leq 6.4$
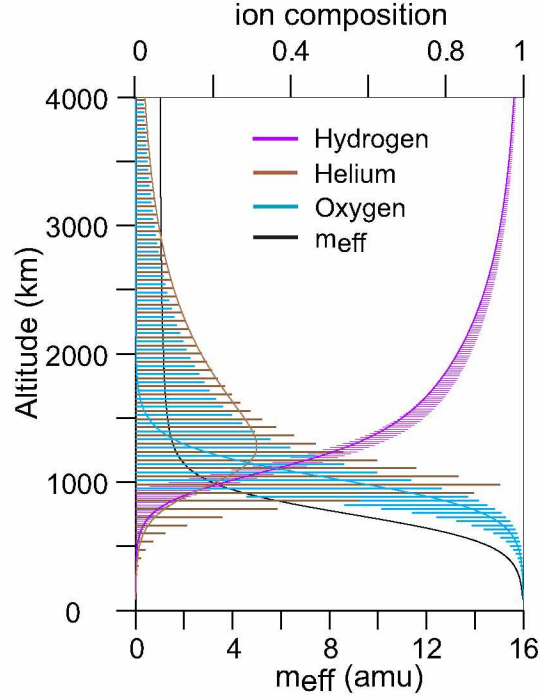
Figure 4.7 Uncertainty in the measurement of relative ion compositions. Black curve shows the m_{eff}, the solid curves show hydrogen (pink), helium (brown), and oxygen (cyan) ion relative concentrations with uncertainty [Courtesy: Sonwalkar et al., 2011b].

4.3.4 Certain aspects of raytracing simulation of the night side cases

One of the major uncertainties associated with the analysis of the night side cases are the cut-off measurements. Almost 90% of the plasmagrams of the night side cases are noisy, particularly on the X-antenna. There is a noise band observed in the whole frequency range of MR echoes on the X-antenna in most of the cases. On the Y-antenna, the echo is discrete, with only one bin spread of time delay, but the lower cut-off ($f_{lh,sat}$) and upper cut-off are not clear. 3-4 bins of resonances are observed near $f_{lh,sat}$ and the MR echoes near the upper cut-off frequency do not show any rise in time delay. Based on our observations on day side cases, we see that the MR cut-offs on the Y-antenna are generally 1-2 bins less than those of the X-antenna. As those echoes of night side are discrete on Y-antenna with only bin spread, it is difficult to match the time delay exactly as observed on the Y-antenna near the upper cut-off. When the models were found using the cut-off observed on the Y-antenna as the $f_{MR,max}$, the time delay of the echoes near the upper cut-offs was higher by ~15 ms. For the same cases, another model is also found taking upper cut-offs as 2-3 bins higher than the observed cut-off on the Y-antenna. The time delay from these models matches well with the observed time delay near upper cut-offs. Figure 4.8 shows the plasmagram observed

on 14 Oct 2005, 13:19:51 UT at 23.6 MLT. The X-antenna plasmagram is very noisy and does not show any echoes. The Y-antenna shows f_{lh} resonance covering three bins from 7.8 kHz to 8.4 kHz. An MR echo is observed from 8.7 kHz to 11.4 kHz. The time delay of the MR echo near the upper cut-off does not show any sharp rise which shows that the actual cut-off can be 2-3 bins higher than this. The SR echo is overlapped with noise and is seen in patchy form (very faint) only on the combined amplitude antenna in the frequency range of 26.1 kHz to 31.2 kHz.
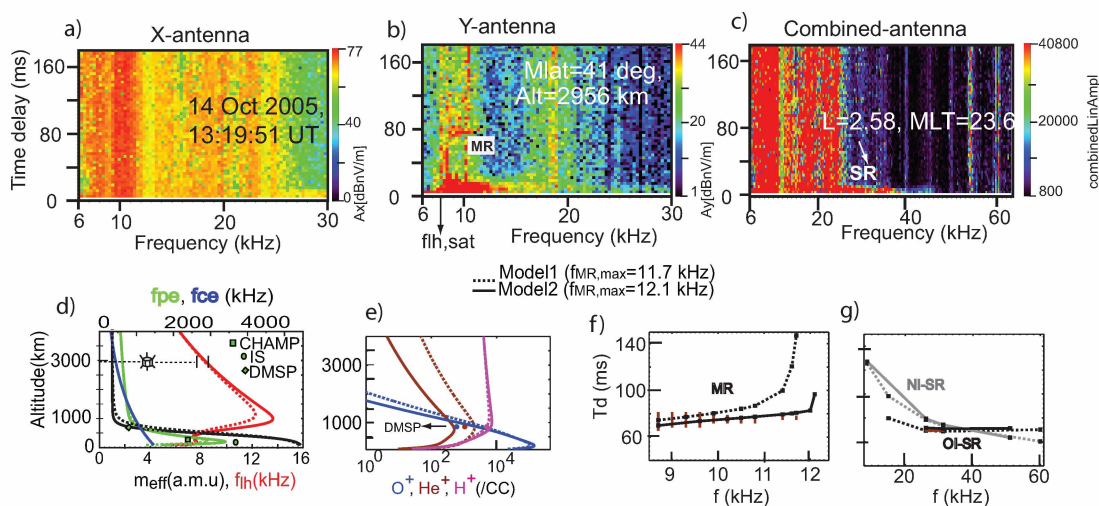
Figure 4.8 Night side plasmagram of 15 October 2005 at 13:19:51 UT showing different cut-offs on X- and Y-antenna. Figure a), b), c) show the plasmagrams of 15 October 2005 at 13:19:51 UT for X-, Y- and combined amplitude antenna. Figure d), e) show the plots of plasma parameters and densities. Figure f), g) show time delays for MR and SR echoes for Model- 1, 2.

Figure 4.8 (2nd row) shows the two models for the 14 Oct 2005 13:19:51 UT case. Figure 4.8 shows Model 1 with $f_{MR,max}$ 11.7 kHz (observed). The calculated time delay with Model 1 from raytracing simulation analysis is ~6-10 ms higher than the measured time delay near 10.2 kHz to 10.8 kHz and ~40-70 ms higher than the measured time delay at 11.4 kHz and 11.7 kHz. Therefore, Model 2 was developed, wherein the calculated time delay matches with the observed time delay up to 11.7 kHz. Model 2 has $f_{MR,max}$ as 12.3 kHz and it shows the rise in time delay at ~12 kHz. Figure 4.8d, e show the plasma parameter comparison of both models. The f_{lhmax1} from Model 1 and Model 2 differs by ~ 1.2 kHz. The foF2 (F2 peak plasma frequency magnitude) with Model 1 is 2.93 MHz and with Model 2 it is 3.11 MHz. Model 1 has higher electron density near 1000 km than model 2. Both models satisfy the observed SR echo time delay. Both models have a similar $f_{lh,sat}$. The O^+/H^+ transition height from Model 1 is 856 km, with 688 km to 892 km of uncertainty limits. The O^+/H^+ transition height from Model 2 is 748 km, which lies within the

uncertainty limit of transition height of Model 1. Model 2 is considered the final model for this case as it matches the time delay for all the observed frequencies of the MR echo. Similar assumptions are considered (upper cut-off 2-3 frequency bins higher than observed) for all cases in night side where there is no higher rise in time delay near the upper cut-off of the MR echo.

Table 4.1 Parameters of Model 1 and 2 for 14 October 2005 13:19:51 UT case.

Model no.	f_{lhmax1} (kHz)	$R_{flhmax1}$ (km)	$f_{lh,sat}$ (kHz)	O^+/H^+ (km) (Uncertainty)	$O^+/(H^++He^+)$ (km) (Uncertainty)	foF2 (MHz)	hmF2 (km)
1	12.4	1142	8.23	856 (688, 892)	808 (952, 1354)	2.93	229
2	13.85	992	8.32	748 (610, 754)	736 (532, 754)	3.11	239
Input Parameters							
Model no.	$N_{e,sat}$ (/cc)	O^+	H^+	He^+	r_b (km)	T (K)	S_{cbot} (km)
1	4800	0.3	0.5	0.2	930	1700	150
2	4800	0.15	0.84	0.01	930	1320	200

4.3.5 Raytracing analysis of the cases with different upper cut-off of MR echo in X- and Y-antenna on day side

There are a number of cases on the day side where either the MR echo is discrete on both the X- and Y-antennas, or the MR echo is multipath on the X-antenna and discrete on the Y-antenna or the MR echo is diffuse on the X-antenna and discrete on the Y-antenna. In most of these cases the upper cut-off of the Y-antenna is one frequency bin less than that of the X-antenna. If the amplitude of the upper cut-off of the MR echo is low on the X-antenna, as the Y-antenna was partially broken in September 2004 (discussed in Chapter two) the echo may not be observed on the Y-antenna. In this case, there can be two models satisfying the cut-offs for both the X- and Y-antennas. The plasmagram of 14 October 2005 at 12:52:51 UT shown in Figure 4.9 is an example. The upper cut-off of the MR echo on the X-antenna is 8.4 kHz and the upper cut-off observed on the Y-antenna is 8.1 kHz. No SR echo is observed for this case. There are two models satisfying two different cut-offs. The SR echo time delays for both of these models are found using the criteria described in Section 4.3.8. Figure 4.9 shows the plasmagrams of the X- and Y-antennas of this case, plasma parameters, ion density profiles along satellite L-shell, and time delays for MR and both types of SR echoes. Model 1 satisfies the upper cut-off of the Y-antenna and Model 2 satisfies the upper cut-off of the X-antenna. The calculated time delay for the MR echo from both the models

satisfies the average observed time delay. Table 4.2 shows the key parameters from both these models. For both models, N_e at the satellite differs by 270/cc, $f_{lh,sat}$ varies by 0.1 kHz and $f_{lh,max1}$ varies by 0.2 kHz. Model 2 has higher $f_{lh,max1}$ for which it has MR upper cut-off one bin (0.3 kHz) higher than Model 2. The O^+/H^+ transition height from Model 1 is 1294 km, with 1084 km to 1354 km of uncertainty limits. The O^+/H^+ transition height from Model 2 is 1126 km, which lies within the uncertainty limit of Model 1. The foF2 of both the models differs by $\sim$20%. Model 2 is considered the final model for these types of cases included in this dissertation.
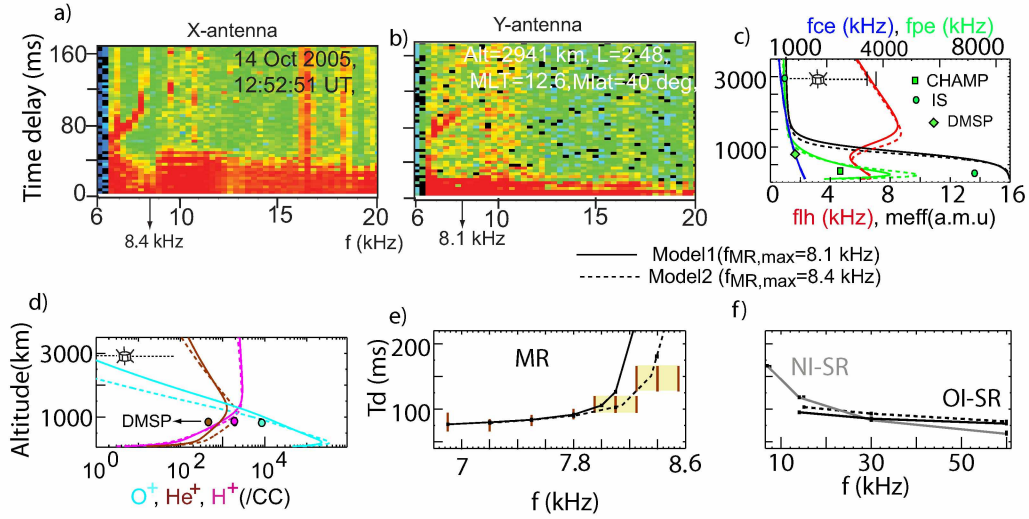
Figure 4.9 Day side plasmagram observed on 14 October 2005 at 12:52:51 UT showing different cut-offs on X- and Y-antenna and raytracing analysis results. Figure a), b) show the plasmagrams of 14 October 2005 at 12:52:51 UT for X-, Y-antenna. Figure c), d) show the plots of plasma parameters, ion density variation and time delays for MR and SR echoes for Model 1 and 2.

Table 4.2 Parameters of Model 1 and 2 for 14 October 2005, 12:52:51 UT case.

Model no.	f_{lhmax1} (kHz)	$R_{flhmax1}$ (km)	$f_{lh,sat}$ (kHz)	O^+/H^+ (km) (Uncertainty)	$O^+/(H^++He^+)$ (km) (Uncertainty)	foF2 (MHz)	hmF2 (km)
1	8.5	1590	6.6	1294 (1084, 1354)	1222 (952, 1354)	4.24	218
2	8.7	1400	6.5	1126 (964, 1210)	1036 (856, 1210)	5.22	205
Input Parameters							
Model no.	$N_{e,sat}$ (/cc)	O^+	H^+	He^+	r_b (km)	T (K)	S_{cbot} (km)
1	2970	0.62	0.23	0.15	1150	1890	130
2	2700	0.4	0.3	0.3	1100	1500	130

4.3.6 Raytracing analysis with multiple models for same case with discrete MR and SR

There are a number of cases where observed MR and SR echoes are discrete (time delay spreads over 1-2 bins). In this type of category there can be multiple models with different input parameters satisfying the average observed time delay for both MR and SR echoes. Figure 4.10 shows such an example. The plasmagram on 22 October 2005 at 20:04:42 UT has discrete MR and SR echoes. Model 1 and Model 2 satisfy the average observed time delays of the MR and SR echoes. From Table 4.3 N_e at the satellite differs by $\sim$18%, the $f_{lh,sat}$ varies by 0.12 kHz, and f_{lhmax1} varies by 0.02 kHz for the two models. The O^+/H^+ transition height from Model 1 is 1360 km, with uncertainty limits of 1132 km to 1372 km. The O^+/H^+ transition height from Model 2 is 1144 km, which lies within the uncertainty limits of Model 1. The foF2 for both the models differs by $\sim$8.5%. Since both the models agree very well with observations, for this type of cases, the model which agrees best with the DMSP and CHAMP satellite data are considered as final model.
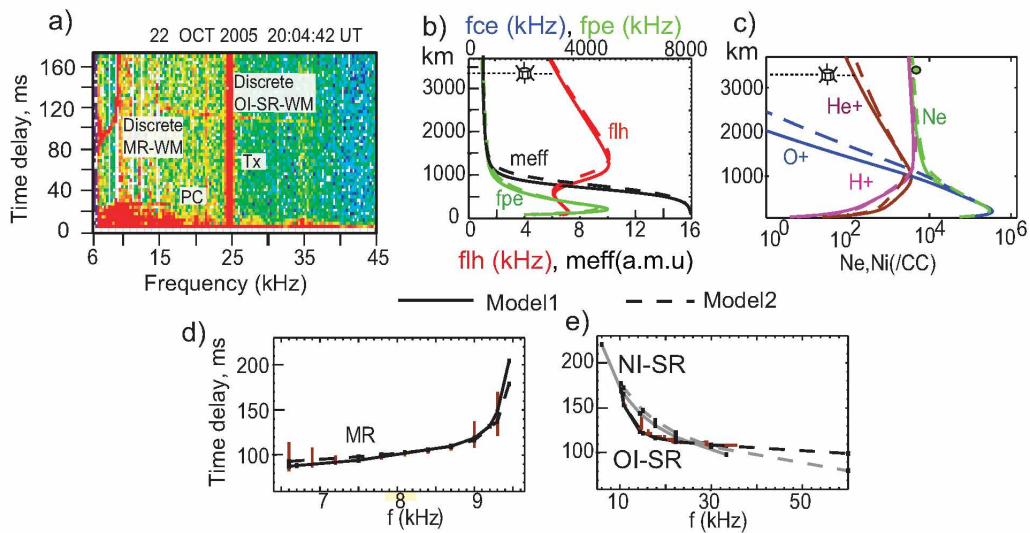
Figure 4.10 Plasmagram of 22 October 2005 at 20:04:42 UT showing discrete MR and SR echoes and raytracing analysis results. Figure a), b), c) show the plasmagrams of 22 October 2005 at 20:04:42 UT for X-antenna and plot of plasma parameters and densities. Figure d), e) show the plots time delays for MR and SR echoes for Model- 1, 2.

Table 4.3 Parameters of Model 1 and 2 for 22 October 2005, 20:04:42 UT case.

Model no.	f_{lhmax1} (kHz)	$R_{flhmax1}$ (km)	$f_{lh,sat}$ (kHz)	O^+/H^+ (km) (Uncertainty)	$O^+/(H^++He^+)$ (km) (Uncertainty)	foF2 (MHz)	hmF2 (km)
1	10.06	1270	6.28	1360 (1132,1372)	1348 (1006, 1372)	5.3	215
2	10.08	1425	6.4	1144 (958, 1204)	1066 (844, 1204)	4.87	228
Input Parameters							
Model no.	$N_{e,sat}$ (/cc)	O^+	H^+	He^+	r_b (km)	T (K)	S_{cbot} (km)
1	3320	0.1	0.5	0.4	1200	1400	150
2	4000	0.49	0.29	0.22	1080	1680	150

4.3.7 Raytracing analysis of cases of SR which could be either NI or OI

From raytracing analysis it is seen that the slope of the NI and OI echoes are very different. The OI echo has steeper slope at higher frequencies than the NI echo, whereas the NI echo has steeper slope than the OI echo at lower frequencies near the upper cut-off of the MR echo. If the SR echo is observed for a very short range (5-10 kHz) near higher frequencies, then, for some cases, there could be more than one model satisfying the observed time delay either with an OI or an NI-SR echo. The OI echo gathers time delay above $R_{flhmax1}$ altitude and at F2 peak, while the NI echo gathers most of its time delay near the F2 peak. Therefore, it is not possible for all the cases with a short range of SR echoes near higher frequencies to have models matching time delays for NI and OI echoes, because the time delay for the MR echo needs to be matched too. Since the OI echo also gathers time delay above $R_{flhmax1}$, changing the model above $R_{flhmax1}$ can change the time delay of the MR echo. Figure 4.11 shows an example of MR echoes observed simultaneously with a short range of SR echoes (observed 45-55 kHz). Model 1 has a lower F2 peak than Model 2 and satisfies the average observed time delay of the MR echoes and the SR echoes (OI-SR). The time delay for the NI-SR echo for this model is 20 ms lower than the OI-SR echo at the observed range. In the case of Model 2 at satellite altitude, N_e is 500/cc higher than Model 1 and F2 peak is 2.3 MHz higher than Model 1. This increases the time delay for both the NI-SR and OI-SR echoes at the observed range. The time delay of the NI-SR echoes increases more than that of the OI-SR echo because they gather more time delay at the F2 peak. The time delay for the NI-SR echoes matches with the lower part of the observed SR echo the (within the limit of uncertainties for time delay). MR echo time delay matches with Model 2 at the upper part of the observed echo. Since both the

MR and SR echoes are discrete so the Model 2 can also be considered as a suitable model.
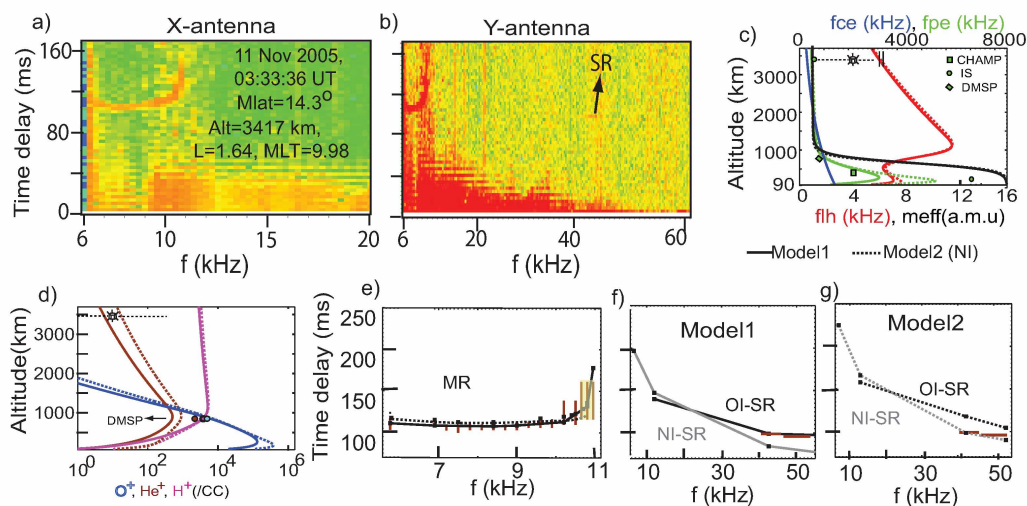
Figure 4.11 Plasmagram of 11 November 2005 at 03:33:36 UT and raytracing analysis results. Figure a), b) show the plasmagrams of 11 November 2005 at 03:33:36 UT for X-, Y-antenna. Figure c), d) show the plots of plasma parameters, ion density variation. Figure e), f), and g) show time delays for MR and SR echoes for Model- 1 and 2.

Table 4.4 Parameters of Model 1 and 2 for 11 November 2005, 03:33:36 UT case.

Model no.	f_{lhmax1} (kHz)	$R_{flhmax1}$ (km)	$f_{lh,sat}$ (kHz)	O^+/H^+ (km) (Uncertainty)	$O^+/(H^++He^+)$ (km) (Uncertainty)	foF2 (MHz)	hmF2 (km)
1	11.73	1126	6.06	898 (772, 904)	886 (700, 904)	3.25	230
2	11.78	1163	6.18	922(784,934)	898 (700, 934)	5.56	220
Input Parameters							
Model no.	$N_{e,sat}$ (/cc)	O^+	H^+	He^+	r_b (km)	T (K)	S_{cbot} (km)
1	3008	0.21	0.72	0.07	1020	1220	320
2	3500	0.4	0.5	0.1	950	1350	110

Form Table 4.4 for both models, N_e at the satellite differs by ~15%, $f_{lh,sat}$ varies by 0.12 kHz, and, f_{lhmax1} varies by 0.05 kHz. The O^+/H^+ transition height from Model 1 is 898 km, with uncertainty limits of 772 km to 904 km. The O^+/H^+ transition height from Model 2 is 922 km, which lies within the uncertainty limits of Model 1. The foF2 of both the models differs by ~52%. These types of cases are not included in the electron and ion density results in this chapter.

4.3.8 Raytracing analysis of the cases of MR only (no SR echo is observed) to find N_e up to Earth-ionosphere boundary
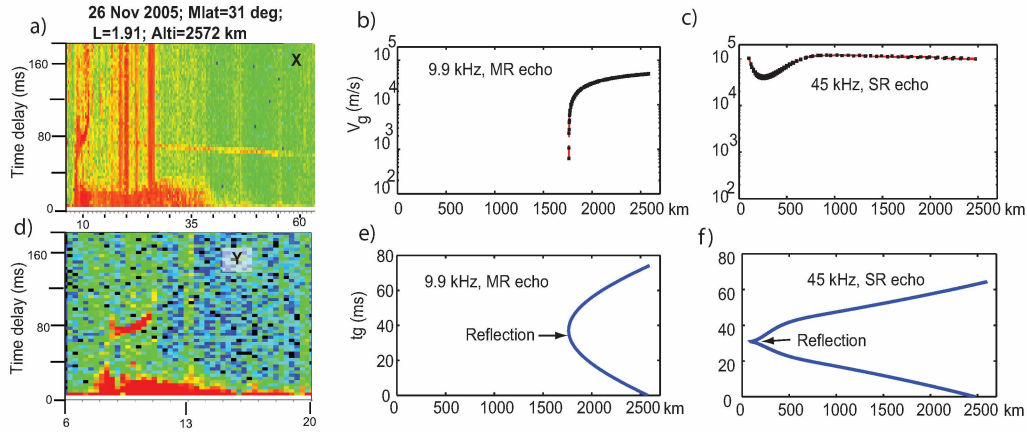
Figure 4.12 Plasmagrams of X- and Y-antenna observed on 26 November 2005 at 05:34:27 UT and raytracing analysis results. Figure a), d) show the plasmagrams of X- and Y-antenna observed on 26 November 2005; Figure b) and c) show the group velocity of MR echo at 9.9 kHz and SR echo at 45 kHz with respect to altitude; figures e), f) show the time delay gathered by the MR echo at 9.9 kHz and SR echo at 45 kHz with respect to altitude.

Out of 82 cases included for raytracing analysis, there were 27 cases where only MR echoes were observed (SR echo was not observed). The method can only give N_e up to the reflection altitude of MR echoes, which is about 1000 km. However, there are a few ways to predict the N_e up to the Earth-ionosphere boundary for those types of cases. For the cases where MR is observed simultaneously with SR echoes, the time delay of the SR echoes in the frequency range ∼40 kHz-60 kHz (the ranges where the time delay does not show much of dispersion, remains almost constant) is within ∼5-15 ms range of the middle frequency range of MR echoes (the range where the time delay of the echoes does not show much dispersion). This is better understood with the example shown in Figure 4.12. The plasmagrams shown in Figure 4.12a, d are for the X, Y-antenna on 26 November 2005 at 05:34:27 UT. The average time delay of the MR echo in the frequency range 9.3-9.9 kHz is ∼70 ms and the average time delay of the SR echo in the frequency range ∼45-60 kHz is ∼60-65 ms. So, the time delay difference is ∼5-10 ms. This can be explained in terms of the group velocity and total time delay of the ray.

4.3.8.1 Group velocity and time delay accumulation for MR and OI-SR echo ray path

The group velocity (Vg) of a WM ray can be given in terms of is the local electron cyclotron frequency (f_{ce}) and local electron plasma frequency (f_{pe}) as:

$$Vg = 2c\frac{\sqrt{ff_{ce}cos\theta}}{f_{pe}} \tag{4.1}$$

where f is the frequency of the ray and θ is the wave normal angle of the ray. The total time delay can be given in terms of Vg and path length as:

$$Tg = \int \frac{ds}{v_g} \tag{4.2}$$

where ds is the element of the path and the total time delay is obtained by integrating over the whole ray path.
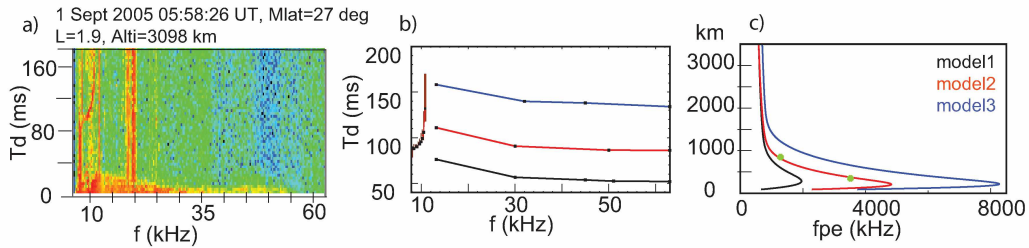

Figure 4.13 Plasmagram of September 1 2005 at 05:58:26 UT and raytracing analysis results. Figure a) shows the plasmagram of September 1 2005 at 05:58:26 UT where only MR echo is observed; b) shows the time delay calculated for MR and SR echoes from three models with similar time delay for MR echo but different time delay for SR echo; c) shows the altitudinal profile of electron plasma frequency for all the models.

Figure 4.12b, c shows the group velocity (Vg) and Figure 4.12e and 4.12f show the time delay of the 9.9 kHz frequency of the MR echo and the 45 kHz frequency of the SR echo obtained from raytracing simulation with a model satisfying the observed time delay. Throughout the path, the Vg of the MR echo is less than the Vg of the OI-SR echo. The MR echo has minimum Vg near the point of reflection where the wave normal angle is ~90°. This makes the term cosθ very small. The SR echo has minimum Vg near the F2 peak because at this region the f_{pe} is maximum. The path length of the MR ray is smaller than that of the SR ray. The MR ray gets reflected at an altitude of ~2000 km (satellite altitude ~2600 km), whereas the SR ray gets reflected at an altitude of 90 km (Earth-ionosphere boundary). The time delay acquired by the SR ray up to the reflection altitude of the MR ray (~2000 km) is less than the time delay of the MR ray, as the SR ray has higher Vg than the MR ray. The SR ray gathers more time delay near the F2 peak where it has minimum

Vg. Thus the net time delay gathered by the SR ray is ~10 ms lower than the MR time delay. For the same reason, we do not observe cases in pr#38 plasmagrams where the SR time delay at a higher frequency (~40 ms and higher) is greater than the observed MR time delay.

4.3.8.2 Best model for the SR echo

For cases where no SR echo is observed, we can have multiple models with similar MR time delays but different SR time delays. Based on the analysis discussed, we can choose the model where the SR time delay in the higher frequency range is comparable to the MR time delay in the middle frequency range. Figure 4.13a shows the the MR echo observed without the SR echo on 1 September 2005 at 05:58:26 UT. At this time the satellite was at L-shell 1.9 and MLT 15. Figure 4.13b shows the time delay obtained from all three models. The average time delay of the MR echo in the middle frequency range is ~90 ms. All three models have similar MR time delays but different SR time delays. Model 1 has a ~60 ms time delay at higher frequencies (OI-SR), which is ~30 ms lower than the middle frequency range of the MR echo. Model 2 has an OI-SR echo time delay at higher frequencies comparable to the middle range of the MR echo. Model 3 has time delay ~40 ms higher than the middle frequency range of the MR echo. Figure 4.13c shows the plasma frequency plot of the three models. Model 3 has the highest N_e (f_{pe}) throughout the ray path. The green dots at altitudes 850 km and 350 km are the in-situ N_e from the DMSP and CHAMP satellites, respectively. The L-shell of these satellites lie within a 0.03 difference. The MLT of the DMSP satellite is 18 and the MLT of the CHAMP satellite is 12. The N_e from both satellites agrees best with Model 2. Model 2 also agrees with the theoretical predictions for the best possible time delay for the OI-SR echo (time delay at higher frequency of the OI-SR echo is comparable to the time delay of the middle range of MR echo). The F2 peak from the ionosonde data can also be used for comparison, but on this day for this case no nearby ionosonde data was available.

Table 4.5 Parameters of Model 1, 2, and 3 for September 1 2005, 05:58:26 UT case.

Model no.	f_{lhmax1} (kHz)	$R_{flhmax1}$ (km)	$f_{lh,sat}$ (kHz)	O^+/H^+ (km) (Uncertainty)	$O^+/(H^++He^+)$ (km) (Uncertainty)	foF2 (MHz)	hmF2 (km)
1	11.49	1212	7.48	904 (688, 940)	856 (562, 940)	1.95	285
2	11.47	1297	7.5	1024(856, 1066)	964 (748, 1066)	4.82	209
3	11.38	1745	7.94	1438(1222, 1438)	1438 (1096, 1438)	8.27	217
Input Parameters							
Model no.	$N_{e,sat}$ (/cc)	O^+	H^+	He^+	r_b (km)	T (K)	S_{cbot} (km)
1	4500	0.4	0.45	0.15	930	2120	200
2	4570	0.36	0.42	0.22	1050	1600	130
3	6430	0.861	0.138	0.001	1160	1870	130

From Table 4.5 it is seen that N_e at the satellite differs by $\sim$35%, $f_{lh,sat}$ varies by 0.46 kHz, and f_{lhmax1} varies by 0.11 kHz. The O^+/H^+ transition height from Model 2 (best model) is 1024 km with uncertainty limits of 856 km to 1066 km. The O^+/H^+ transition height from Model 1 is 904 km which lies within the uncertainty limits of Model 1, but the O^+/H^+ transition height from Model 3 is 1438 km, which is $\sim$400 km higher than the upper uncertainty limits of Model 2. Model 3 has highest O^+ and Rbase, which is why it has the highest O^+/H^+ transition height. The foF2 of the models differs by $\sim$120%. So, the cases where no SR echo is observed can have the highest rate of uncertainty at the F2 peak, but it can be reduced by choosing a suitable model based on observations from other cases of MR with OI-SR echoes.
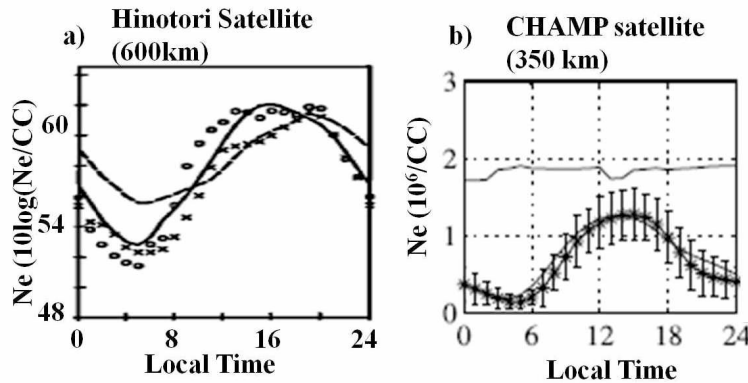
Figure 4.14 Diurnal variation of electron density at from Hinotori and CHAMP satellites. Figure a) shows the diurnal variation of N_e at from Hinotori satellite at 600 km [courtesy: Su et al., 1996], b) shows the diurnal variation of N_e from CHAMP satellite at 350 km [courtesy: Liu et al., 2007].

4.3.9 Model for the SR echo based on DMSP, CHAMP and ionosonde data

We can also say that when an SR echo is not observed with an MR echo, N_e from DMSP ($\sim$850 km), CHAMP ($\sim$350 km), and ionosonde stations (at the F2 peak) can be used to construct the N_e profile along the satellite L-shell at lower altitudes. There are three main parameters that need to be checked for comparison: UT (universal time), MLT (magnetic local time), and LT (local time), as well as L-shell and great circle distance (GCD) for ionosonde stations. Figure 4.15 shows the diurnal variation of the F2 peak from ionosonde stations located at different latitudes (figure taken from Luan et al., (2008)). When the local time (or MLT) is in the range of 0-8, 12-16, and 20-24, the F2 peaks are comparable. But if LT or MLT are in of the range of 9-12 or 17-20, the F2 peaks can change by 3-4 MHz. For comparison with the WM sounding F2 peak, this factor should be considered (even if the L-shell is nearby). Figure 4.14 shows the diurnal variation of N_e from the CHAMP (350 km) and Hinotori satellites (600 km) (figures taken from Liu et al., 2007 and Su et al., 1996). For cases where MR is observed with SR, the F2 peak from the WM sounding results is $\sim$1.5-3 MHz lower than the ionosonde F2 peak for day side cases (Figure 4.16). In this case, using the ionosonde F2 peak as a reference for cases without SR echoes will not be consistent with other cases where the F2 peak is calculated from observed SR echoes. McNamara (2006) has discussed the quality figures and error bars associated with autoscaled ionograms (scaling of the ionograms done using the ARTIST method (Reinisch et al., 2005). Ionogram autoscaling is a complex and difficult process that will never be perfect because of the complexities of the ionosphere. Depending on the various conditions of the quality of the echo observed on the ionograms, the uncertainty in estimating foF2 could be 0.1 MHz to 1.4 MHz. McNamara et al., (2007) have found that the average discrepancy for the CHAMP satellite passing above the peak of the F2 layer has a standard deviation of 0.8 MHz (or 13.3%).
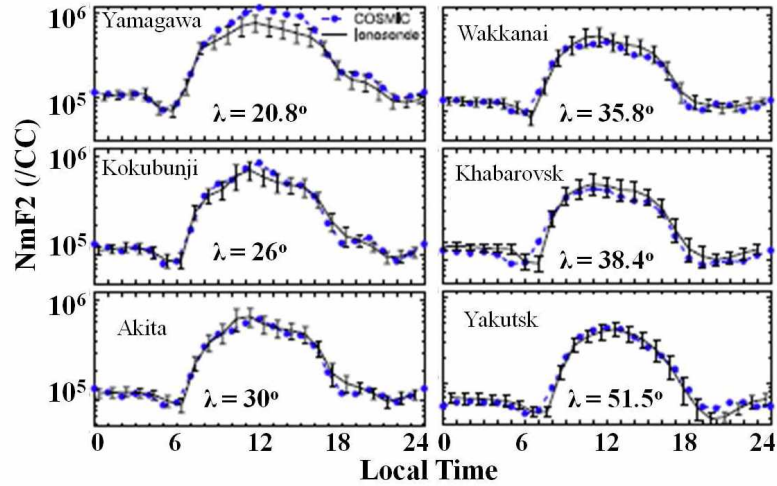
Figure 4.15 Diurnal variation of F2 peak at different latitudes [Courtesy: Luan et al., 2008].
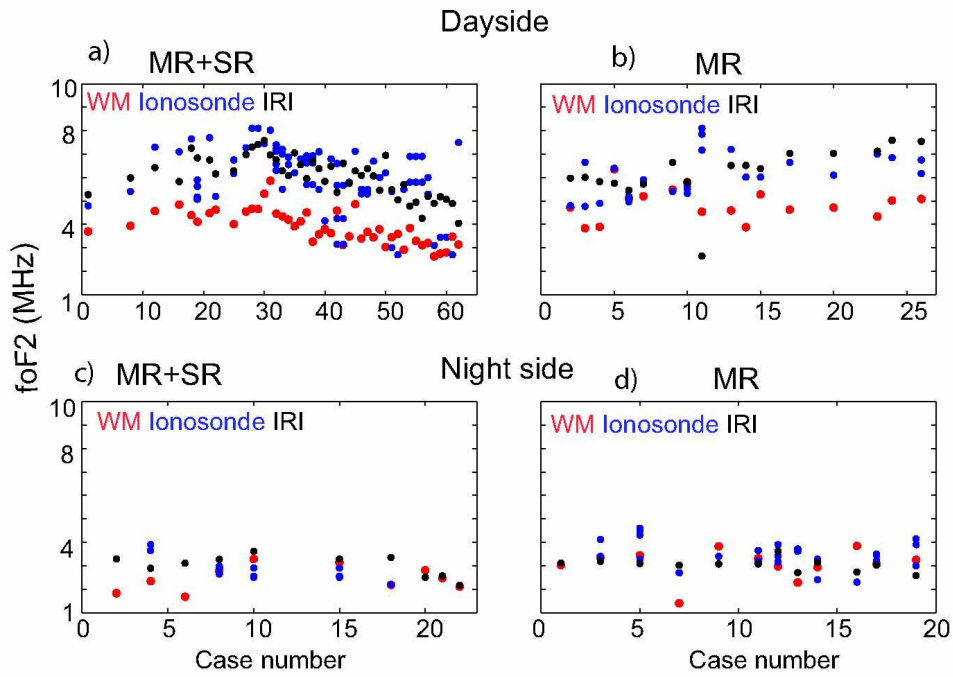
Figure 4.16 Comparison of foF2 from the WM sounding, IRI-2012 model and ionosonde for day and night sides. Figure a), b) show the comparison of foF2 from the WM sounding, IRI-2012 model and ionosonde for the cases where MR and SR are observed simultaneously and for cases where only MR is observed for day side. Figure c), d) show the same for night side.

4.3.10 MLT variation of IMAGE, DMSP, CHAMP satellite from August to December 2005

Table 4.6 shows the MLT variation of the IMAGE, DMSP (F13, F15), and CHAMP satellites for 2005 August-December. For night side cases of October, November, December the MLT of the CHAMP data is very different from the IMAGE MLT, so it can not always be used for construction of N_e at low altitude (below the reflection altitude of MR echoes). The N_e from CHAMP can be used as a reference, e.g., for the cases of November where CHAMP data have MLT $\sim$15 and IMAGE has MLT $\sim$22, we expect the N_e from WM sounding should be $\sim$3 times lower than the CHAMP data at 350 km altitude (Figure 4.14b. Similarly, for the case of DMSP data, other than for the month of November, day side the MLT difference is more, however, we can have an estimate in general from Figure 4.14a of N_e variation with local time (or MLT) at those altitudes. For the case of September day side, where IMAGE MLT is $\sim$14 and closest MLT for DMSP data is 17-18, in that case with reference to Figure 4.14a we can estimate that the N_e at those two MLTs should be within $\sim$15-30%.

Table 4.6 MLT variation of IMAGE, DMSP, CHAMP satellite August to December 2005.

Month	IMAGE MLT	DMSP F13 MLT	DMSP F15 MLT	CHAMP MLT
Aug	$\sim$15, $\sim$3-4	7-8, 17-18	9-10, 19-20	$\sim$12-13, $\sim$0.5
Sept	$\sim$14, $\sim$3-4	7-8, 17-18	9-10, 19-20	$\sim$11, $\sim$23
Oct	$\sim$12, $\sim$3-4	7-8, 17-18	9-10, 19-20	$\sim$7.5, $\sim$19
Nov	$\sim$9-10, $\sim$21-22	7-8, 17-18	9-10, 19-20	$\sim$4-5, $\sim$15.5-16.5
Dec	$\sim$8, $\sim$20	7-8, 17-18	9-10, 19-20	$\sim$2.5-3.5, $\sim$14-15

For the results of electron and ion densities for all the night side cases (20 cases) included in this chapter, models satisfying all the observed time delays are considered (e.g. Model 2 shown in Section 4.3.4 for the case). For cases where the upper cut-off has one bin frequency of uncertainty, the model can have 10-20% of difference in N_e from satellite altitude up to 1000 km. For cases observed with only MR (cases for day side and night side) the models are found based on the criteria discussed in Section 4.3.8. For cases with discrete MR and SR echoes, there is a $\sim$5-20% difference between models satisfying the observed echo best. The model that agrees best with DMSP and CHAMP satellite data is chosen for electron and ion density measurements.

4.4 Electron density along different L-shells from WM sounding and comparison with other models

Day (MLT~7-16), L-shell~1.6-4   Night (MLT~20-4), L-shell~1.8-4
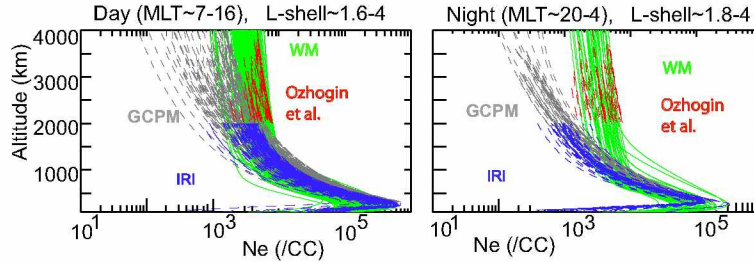
Figure 4.17 N_e from WM sounding, GCPM, IRI-2012, and Ozhogin et al., (2012) model. Comparison of electron density along the magnetic field line from WM sounding with that obtained from GCPM-2009, IRI-2012, and Ozhogin et al., (2012) model for day and night side of the magnetosphere.

Figure 4.17 compares of N_e from the WM sounding, Ozhogin and others, (2012) model, IRI-2012 model (blue), and GCPM (grey) for all the cases included in Figure 4.1 for day and night side of the magnetosphere along different L-shells. GCPM underestimates N_e relative to WM sounding in day and night side above ~1500 km. The slope of N_e variation along the L-shell from WM sounding and Ozhogin et al., (2012) model is steeper than that of GCPM and IRI-2012. The behavior of density fall-off with altitude from WM sounding, above 2000 km is similar to Ozhogin et al., (2012) model, which represents the plasma density from RPI active sounding and passive measurements. Since the GCPM uses the IRI model below 600 km, they seem to overlap at low altitude. The disagreements of these two models relative to WM sounding results are discussed later in this chapter.

4.4.1 Electron density from WM sounding at different altitudes and comparison with other models, in-situ measurements
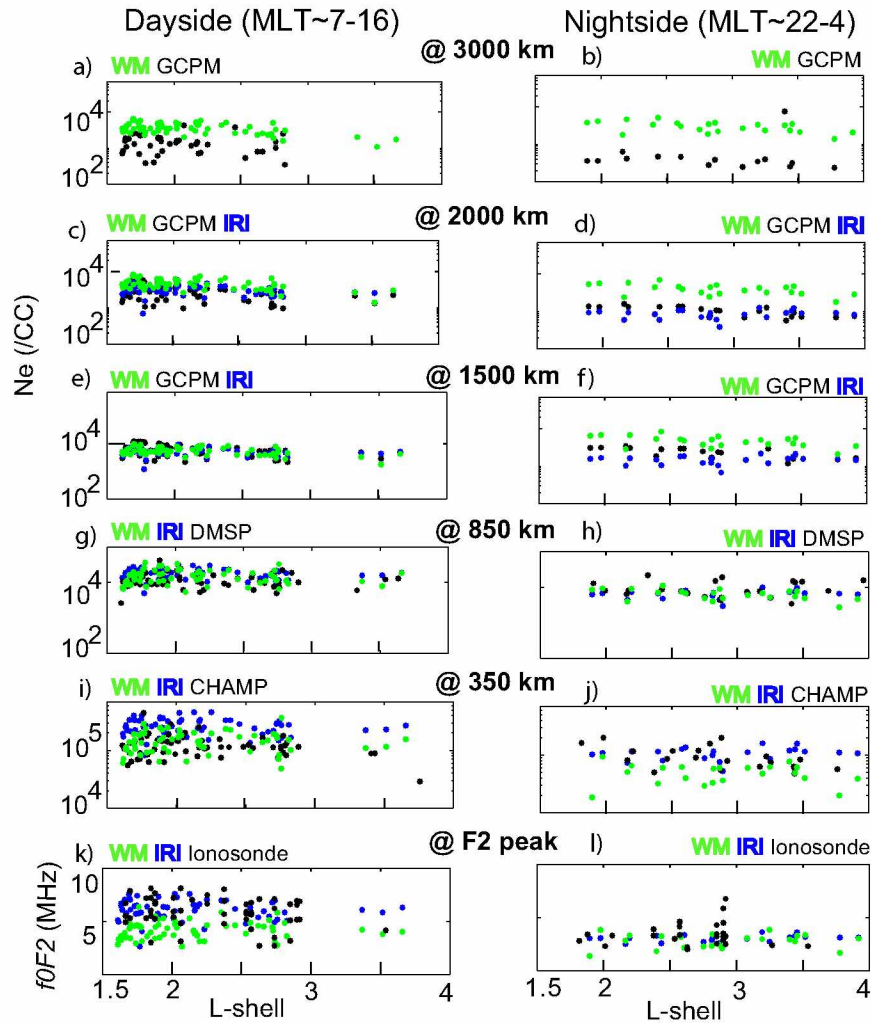
Figure 4.18 N_e from WM sounding, GCPM, IRI-2012 model, and in-situ measurements from CHAMP, DMSP satellites. Comparison of N_e at different altitudes from WM sounding with in-situ measurements from DMSP, CHAMP satellites and IRI-2012, GCPM model for day and night side of the magnetosphere.
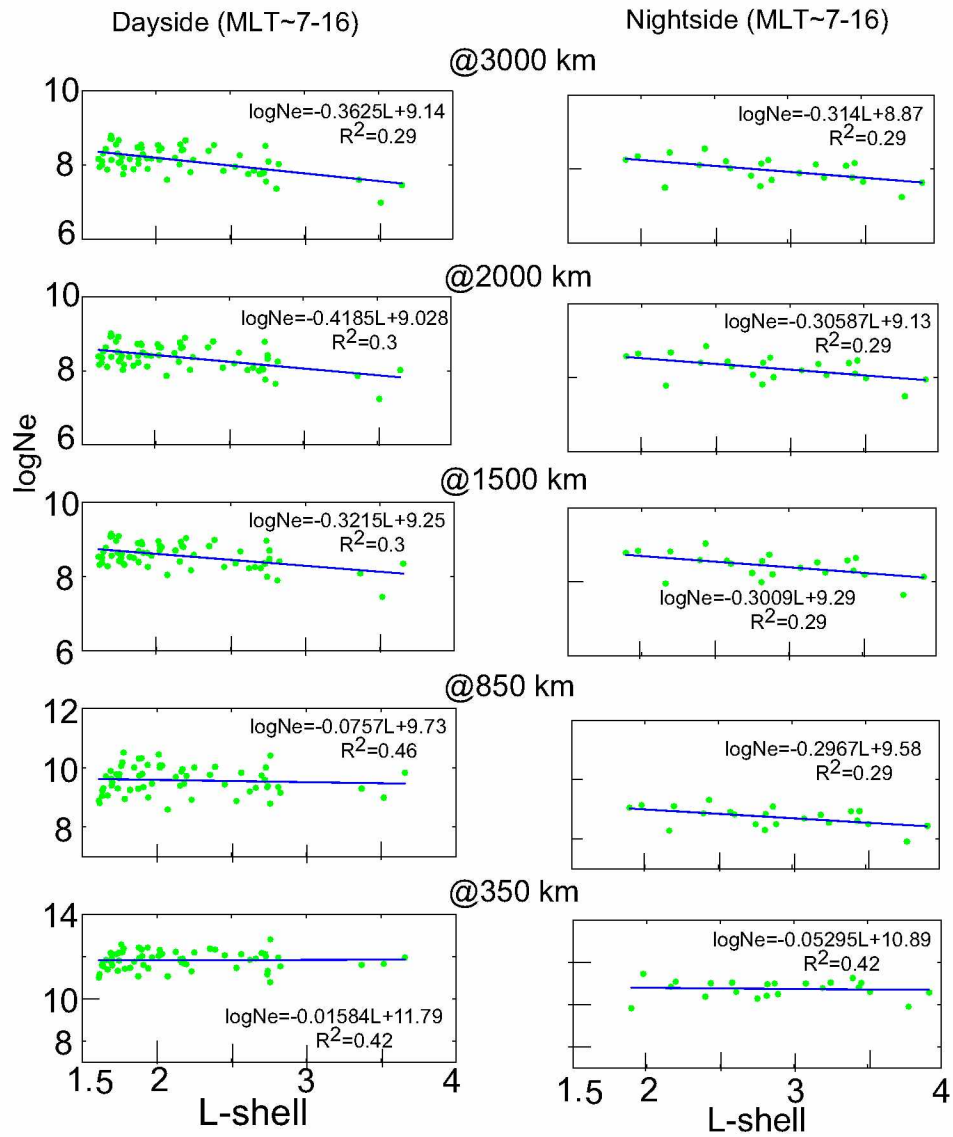
Figure 4.19 Linear fit to the N_e from WM sounding at different altitudes.

Figure 4.18 compares N_e from the WM model (green) for all the cases at different altitudes with model values and in-situ measurements up to the F2 peak. The underestimation of N_e by the GCPM (black) relative to the WM model is greater during night side than day side up to 2000 km. In day side the GCPM (black) underestimates N_e by ~50%, and at night side it underestimates N_e by ~90% relative to the WM sounding. Above 850 km altitude, N_e for day- and night side from the WM sounding is comparable, which means the N_e above this altitude range does not have MLT dependence. Ozhogin et al., (2012) model plotted above 2000 km in Figure 4.17 also does not have any MLT dependence. At lower altitudes (below 1000 km) from the WM sounding, the difference in the N_e for both day- and night sides increases with decrease of altitudes showing MLT dependence of N_e at lower altitudes. From the GCPM model N_e at night side is ~30-40% lower than N_e at day side. N_e values from WM sounding and GCPM both show decrease trend with respect to L-shells. Up to altitude 850 km (4.18c,e,g), N_e values at day side from WM sounding (green) and IRI-2012 model (blue) are comparable. Both show a decreasing trend of N_e with respect to L-shells. At night side, at up to 1500 km (4.18d,f) IRI-2012 underestimates N_e by ~60-90% relative to the WM sounding model. Both models show a decreasing trend with respect to L-shells, which is also confirmed from WM sounding results at those altitudes. Theoretically, if the plasma is considered to follow the diffusive equilibrium model, its plasma density distribution falls off logarithmically with distance from the center of the Earth. Results from the whistler measurements, ISEE, DE-1/RIMS, CRRES satellites, and the IMAGE/RPI data have shown that the electron density in the equatorial region is well approximated by a linear relation between the log of N_e and L-shell (Carpenter and Anderson, 1992; Gallagher et al., 1988). Tarcsai et al., (1988) have shown from whistler data that inside L~2.5 the N_e profile has been found to fall off more steeply, approximately at L-4. From Figure 4.19c it is seen that even though there is a decreasing trend in N_e observed with respect to the L-shells, the quality of this linear fit is low ($R^2 < 0.4$) for all altitudes. In the altitude ranges of 3000 km, 2000 km, and 1500 km for both day and night side, N_e shows a better decreasing trend. However, the quality of fit is low ($R^2 < 0.5$). The power law factor at these altitudes varies between 0.47 and 0.39 for day side and it varies between 0.37 and 0.31 for night side. The quality of fit is calculated with 95% of confidence level. The reason for this is that the data are widely scattered, 4.19b. Below altitude 1500 km, the N_e almost does not show any L-shell dependence (no significant decreasing trend). At 850 km $\log(N_e)$ from the DMSP satellite and at 350 km $\log(N_e)$ from the CHAMP satellite, shows similar R^2 (quality of linear fit) as WM sounding for both the day and night sides. The IRI-2012 model shows ~30-60% lower N_e at night side than day side at similar

L-shells, but N_e from the WM sounding model do not show this trend. At altitude 850 km, both at day- and night side of the magnetosphere, N_e values from the WM sounding model, IRI-2012 model, and DMSP are comparable. At 850 km at night side N_e is ~15-25% lower than the N_e at day side from WM sounding model, IRI-2012 model and DMSP data. For day and night side of the magnetosphere, N_e shows a slightly decreasing trend with respect to L-shells at this altitude. At 350 km, the N_e values from WM model, and the CHAMP satellite, are ~20-30% lower than those from the IRI-2012 model for day side. foF2 (F2 peak plasma frequency in MHz) from the IRI-2012 overestimates foF2 from the WM model by ~30-80%. foF2 does not show any dependence on L-shell in the WM model or the IRI-2012 model in day- or night side. The comparison of the F2 peak from WM sounding, IRI-2012, and ionosonde data is discussed in detail in Figure 4.20.

4.4.2 F2 peak from WM sounding and comparison with IRI-2012 model
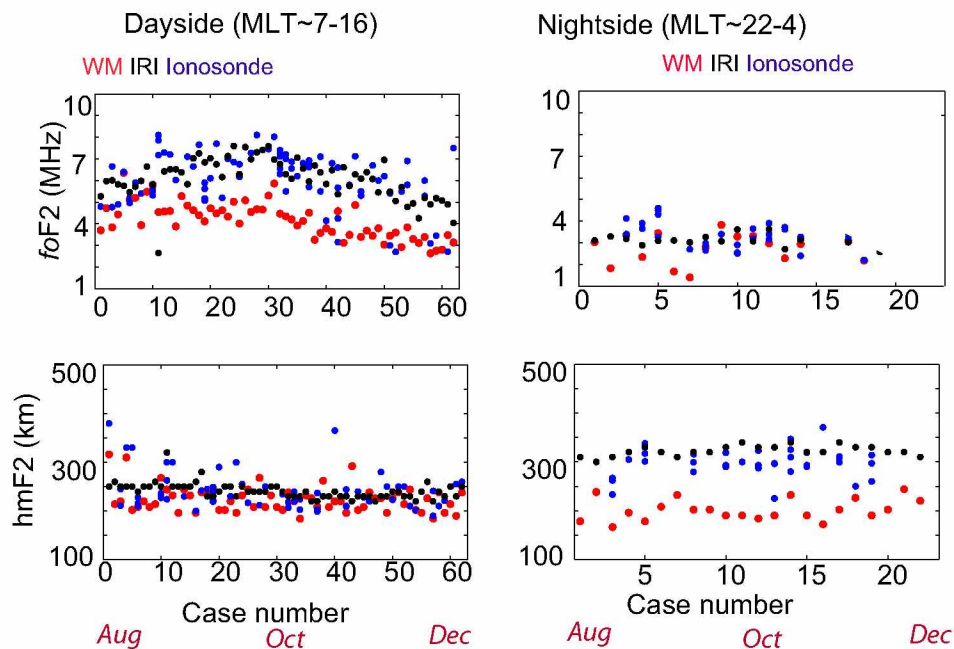
Figure 4.20 F2 peak from WM sounding, ionosonde stations and IRI-2012. Comparison of F2 peak magnitude and altitude from WM sounding (green) with measurements from ionosonde data (blue) and IRI-2012 (black) model with respect to case numbers (Aug-Dec 2005) for day and night side of the magnetosphere.

Figure 4.20 (1st row) shows, at day side, foF2 from the WM (green) varies mostly between ~2-5.5 MHz and foF2 from the IRI-2012 model (black) varies mostly ~4-8 MHz. At night side foF2 values from the WM sounding and the IRI-2012 model are comparable and ~2 MHz lower than the foF2 at day side from the WM sounding. At day side, hmF2 (height of F2 peak in km shown in Figure

4.20 2nd row) from the WM sounding is ∼30-70 km lower than the hmF2 from the IRI-2012 model. At both day and night side the average hmF2 from the WM sounding is ∼200 km. At night time, hmF2 from the WM sounding is ∼100-150 km lower than the hmF2 from the IRI-2012 model. The hmF2 from the IRI-2012 model does not show much variation. At day side it is almost constant at ∼230 km, and at night side it is higher than day side and is almost constant at ∼350 km. Different experiment techniques have reported that, at day time, the average hmF2 is ∼200 km and at night time, ∼300 km (Kim et al., 2011; Liu et al., 2007; Luan et al., 2008; Nsumei et al., 2010). The results from the ionosonde foF2 peak and the IRI-2012 model are comparable most of the time because the IRI-2012 model uses nearby ionosonde station data.

Based on the data of the GPS TEC, COSMIC, CHAMP, and GRACE satellites, it is found that the IRI overestimated N_e in the ionosphere during the 23rd/24th solar minimum years (Liu et al., 2011a, b; Luhr and Xiong, 2010; Yue et al., 2013). To solve this problem during the extreme solar minimum, a new version of the IRI had been updated in 2012 (Bilitza et al., 2014). Zhang et al. (2014) have compared N_e from the IRI-2012 model with DEMETER data at altitude ∼650-700 km for the years of solar minima 2006, 2007, and 2008. They found that the IRI-2012 model overestimated N_e by up to ∼80% at this altitude during solar minima time. We also found overestimation of N_e below altitude 850 km relative to the WM sounding. The correlation co-efficient for N_e from WM sounding and N_e from the IRI-2012 along L-shell (as shown in Figure 4.17) for individual cases varies from 0.85 to 0.97.

4.4.3 Electron density from WM sounding along L-shells and comparison with other in-situ measurements from satellites
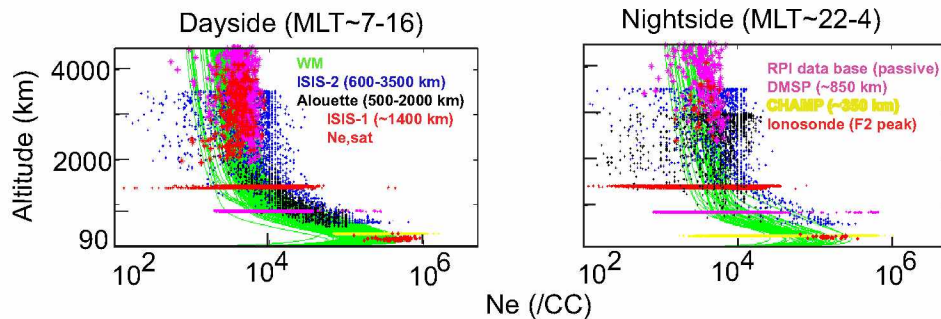
Figure 4.21 N_e from WM sounding and other in-situ measurements. Comparison of electron density along the magnetic field line from WM sounding (green) with in-situ measurements from RPI passive (magenta), ISIS-2 (blue), ISIS-1 (red), Alouette (black), CHAMP (yellow), ionosonde (red) for day and night side of the magnetosphere.

Figure 4.21 shows the results of N_e measurements from the WM sounding compared with in-situ measurements from the ISIS-2 (blue; 600-3500 km), Alouette (black; 500-2000 km), ISIS-1 (red; ~1400 km), DMSP (magenta; ~850 km), and CHAMP (yellow; ~350 km) satellites. Bottom side sounding data (F2 peak magnitude) from ionosonde stations are also shown in red. The data from ISIS-1 were collected during the period of August-December 1969. During this time F10.7 varied between ~170-110. The data from ISIS-2 were collected during the period August-December 1971, August-December 1972 and during this time F10.7 varied between ~120-90. The time period covered by the Alouette satellite data set is August-December 1966. The months covered in this data set are the same as IMAGE in order to eliminate any seasonal dependence. The F10.7 during this time varied between ~90-120 and F10.7 during August-December 2005 (95% of the MR echoes were observed during this time) varied between ~90-120. The reason for using older data or comparison is to show the performance of WM sounding results in a wide range of altitudes and L-shells, and to confirm that the results from WM sounding are in agreement with previous in-situ measurements. The DMSP, CHAMP, and ionosonde data plotted here are from the same time as the IMAGE/RPI data (August-December 2005). The magenta dots above 2000 km are the N_e values from passive measurements from the RPI database for the months August-December 2005 at L-shells 1.6-4 (this database uses f_{ce} from the T96-01 model and upper hybrid frequency emissions or continuum edge in the dynamic spectra. The data can be found at http://www.dartmouth.edu/rdenton/Data/RPIDensity.d). The red dots above 2000 km are N_e measurements at the satellite locations from the dynamic spectra and f_{ce} from the IGRF model for all MR cases. N_e from the WM sounding seems to be comparable among all these datasets.

4.5   Ion density measurements along different L-shells

One of the most important results of this dissertation is the ion composition analysis along different L-shells. This is the first study of ion composition covering along this many L-shells and altitude ranges. In previous satellite or ground experiments, the availability of ion composition measurements at different geophysical locations and conditions was narrow. For this reason the ion composition models are not so reliable. Our study has provided a new scope of ion composition measurements. To show the validity of these results, they are compared with all the available past ion measurements.

4.5.1 Ion density variations from WM sounding along different L-shells comparison with GCPM, IRI-2012 model and DMSP satellites
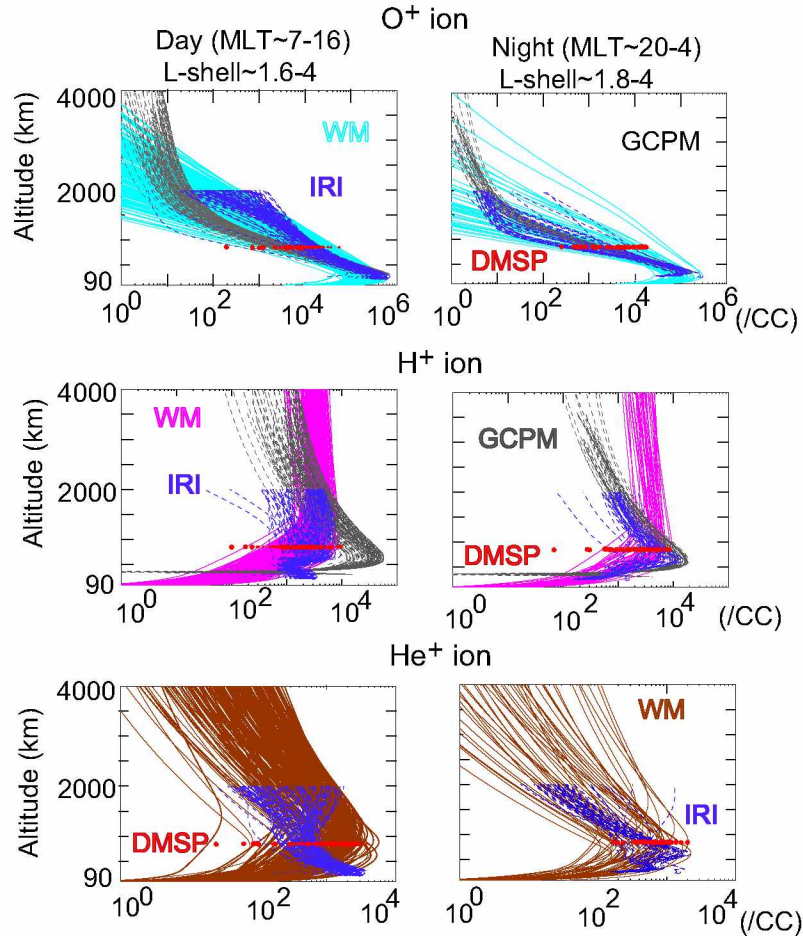
Figure 4.22 Comparison of ion density from WM sounding, DMSP satellite, GCPM-2009 and IRI-2012 model for day and night side of the magnetosphere.

The first row of Figure 4.22 shows O^+ (cyan) ion density variation for day and night side, second row represents the H^+ (magenta) density variation, and the third row is for He^+ (brown) density from the WM sounding of IMAGE/RPI data using the raytracing simulation code. The results are compared with the GCPM (grey dashed), and IRI-2012 (blue dashed) models and DMSP (red circles) in-situ measurements. The GCPM model uses Craven et al., (1997) empirical model for ion densities derived from DE1 data. The IRI-2012 model uses the empirical model for ion densities from the Atmospheric explorer and Intercosmos satellites (Triskova et al., 2003, 2006) and at low altitude it uses the ion density calculator (IDC) model, which is based on chemical equilibrium to determine all ion concentrations (Richards et al., 2010). The O^+ density at day side from the IRI-

2012 model is comparable to that of the WM sounding model. The GCPM model shows a very slow decrease of O^+ above 1000 km for both day- and night side. In the WM sounding, O^+ decreases very rapidly at high altitude. At night side, the O^+ from the IRI-2012 model is comparable to the GCPM model, and they tend to underestimate O^+ relative to the WM sounding. At day side for H^+ ion, it is comparable to the IRI-2012 model but the GCPM model tends to overestimate at low altitude and underestimate at high altitude. On the night side, the overestimation of H^+ by the GCPM relative to the WM sounding and the IRI-2012 model is less compared to the day side, but at altitude above 1000 km both the GCPM and IRI-2012 tend to underestimate H^+ relative to the WM model. Craven et al., (1997) considered minimum He^+ during solar minima, therefore, the GCPM model for He^+ for the year 2005 shows almost zero He^+ and the WM sounding results are compared with the IRI-2012 models only. At night side the He^+ from the WM sounding model and the IRI-2012 model are comparable. The IRI-2012 model tends to underestimate He^+ at $\sim$1000 km relative to the WM sounding results. The range of all the ions (O^+, H^+, He^+) for both day- and night sides from the WM sounding are comparable to the ion density measurements from the DMSP satellite's in-situ measurements at 850 km.

4.5.2 H^+, O^+, and He^+ ion variations from WM sounding along different L-shells comparison with in-situ measurements by ISIS, AE satellites
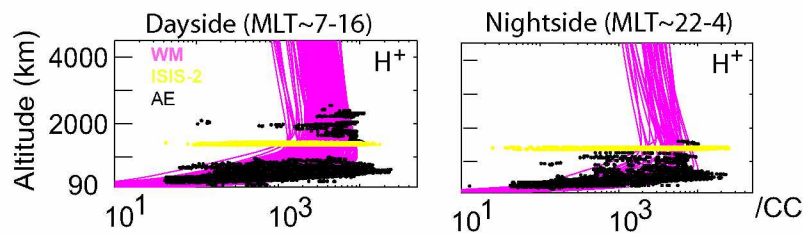
Figure 4.23 Comparison of H^+ density from WM sounding with in-situ measurements from ISIS-2 and AE satellites.
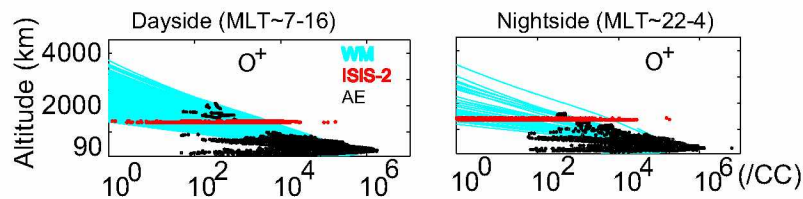
Figure 4.24 Comparison of O^+ density along the magnetic field line from WM sounding with in-situ measurements from ISIS-2 and AE satellites.
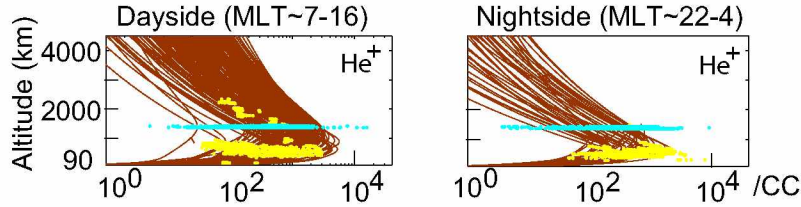
Figure 4.25 Comparison of He$^+$ density along the magnetic field line from WM sounding with in-situ measurements from ISIS-2 and AE satellites.

Figure 4.23, 4.24, 4.25 show density profiles for H$^+$(magenta), O$^+$ (cyan), and He$^+$ (brown) along the L-shells in the day- and night-side of the magnetosphere as derived from the WM sounding on IMAGE using raytracing simulations. Below 1000 km altitude, O$^+$ density is more than one order higher than H$^+$ density and almost two orders higher than He$^+$ density from WM sounding. Above 1000 km H$^+$ is the dominant ion, almost one order of magnitude higher than the He$^+$ ion. On the day side He$^+$ ion comprises 10-20% and at night side, less than 10% of the total ion density. These results also agree well with the previous observations from incoherent scatter radar covering altitude of the F2 peak up to 2000 km (Gonzalez and Sulzar, 1996), DE satellite data covering altitude 300-1000 km (Horwitz et al., 1990), and SROSS C2 and FORMOSAT-1 data covering altitudes ~500-600 km (Borgohain and Bhuyan, 2010). The results are compared with in-situ ion density measurements from the AE and ISIS-2 satellites covering low solar activity time (F10.7 ~ 70-100). These data sets cover the years 1971, 1973, and 1975 during the months of August-December, same as the months covered by the IMAGE/RPI WM data included in this chapter to eliminate the seasonal dependence of ion densities. The scale height of all the ions in AE data at altitude below 2000 km is comparable to the scale height from the WM sounding. The lower limit of H$^+$ density from the ISIS-2 at 1400 km is more than one order of magnitude lower than that from WM sounding. The maximum of O$^+$ ion densities from the WM sounding for both day- and night side occurs at 250 km which is comparable to O$^+$ from AE data. The range of O$^+$ densities from the WM sounding is comparable to ISIS-2 satellite data at ~1400 km. For both day- and night side from WM sounding the maximum of He$^+$ ion densities occurs near about 700-800 km altitude. The range of He$^+$ densities from WM sounding at 1400 km lies within the range from ISIS-2 satellite. He$^+$ ions are produced by photoionization of neutral He and lost chemically by reaction with molecular nitrogen. At high altitudes He$^+$ may also be lost through reaction with atomic oxygen.
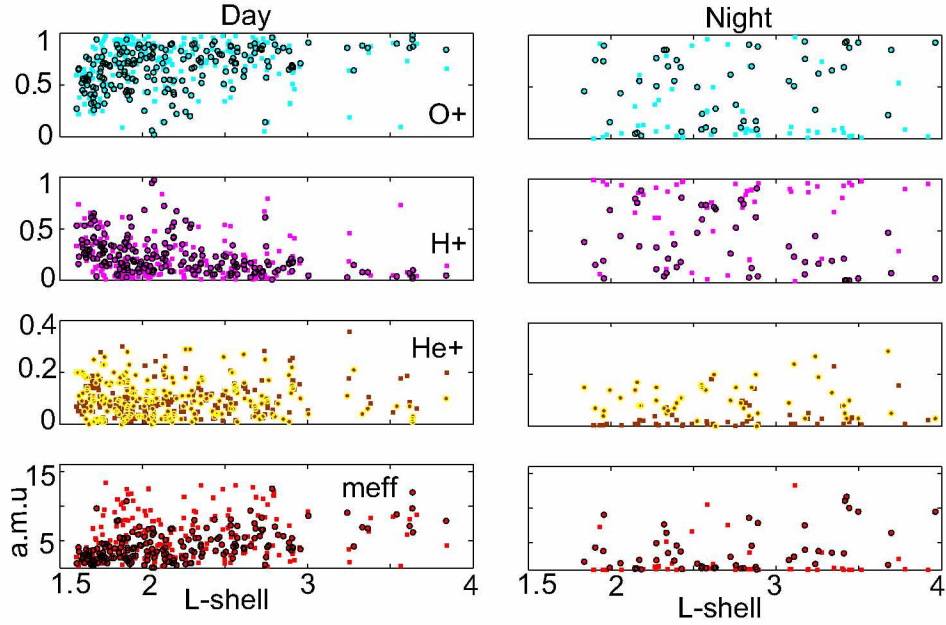
Figure 4.26 Comparison of ion density, m_{eff} from WM sounding with in-situ measurements from DMSP satellite.

The first row of figure 4.26 shows O^+ (cyan), the 2nd row shows H^+, the 3rd row shows He^+ and the 4th row shows m_{eff} from WM sounding in comparison with in-situ measurements from DMSP satellite (circles with colored borders) at 850 km for the day- and night side. From WM sounding most of the cases in night side have lower O^+ and He^+ than day side. H^+ is higher in night side than day side from WM sounding. H^+ decreases with L-shells from both WM sounding and DMSP satellite data. O^+ is the dominant ion at day side and He^+ is the minor ion at day side. At night side, He^+ still remains the minor ion but has more H^+ than O^+. m_{eff} varies between ~ 1.5 to ~ 13 for day side and ~ 1 to ~ 5 for night side for most of the cases from WM sounding. These values are comparable to those m_{eff} calculated from the DMSP ion density data.

4.5.3 m_{eff} variations from WM sounding along different L-shells for day and night side cases
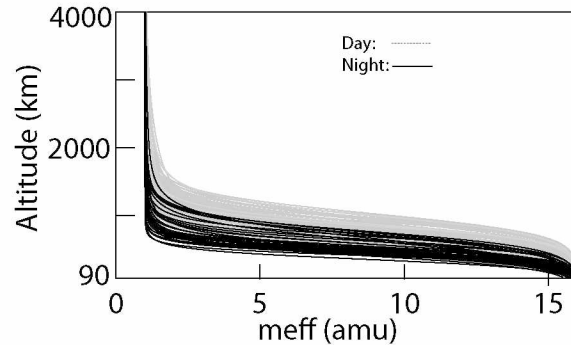
Figure 4.27 Comparison of m_{eff} along L-shells (1.6-4) from WM sounding for day (grey) and night (black) side of the magnetosphere.

Figure 4.27 shows the effective ion mass (m_{eff}) variation along the satellite L-shells covering an altitude range of 90 km to 4000 km for all the cases plotted on Figure 4.1 for both day side (grey) and night side (black) of the magnetosphere from WM sounding of IMAGE/RPI data using raytracing simulation code. At altitudes of 2000 km and above, m_{eff}~1. At altitudes below 2000 km, the m_{eff} at night side is almost half of that on day side due to reduction of heavier ions (O^+) in night side. At altitudes greater than 2000 km O^+ ions are lost by charge exchange with hydrogen atoms at an appreciable rate.

4.5.4 m_{eff} variations from WM sounding at different altitudes and comparison with IRI-2012 model and DMSP satellites
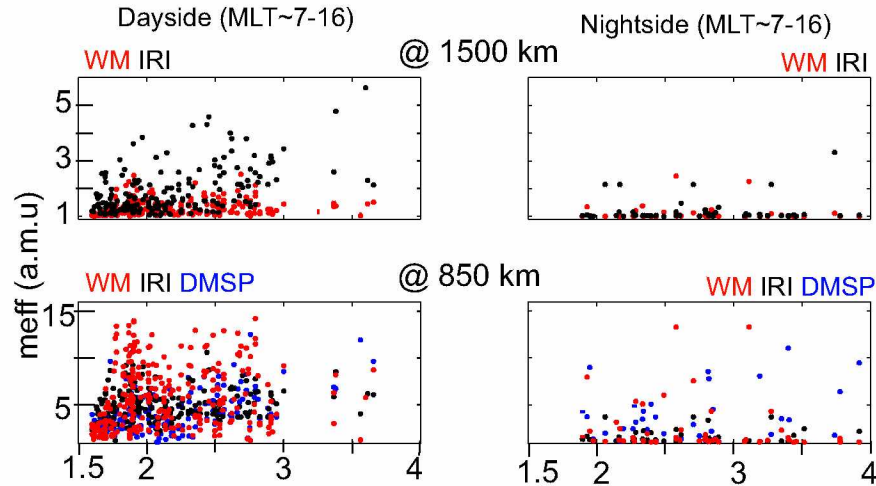
Figure 4.28 Comparison of m_{eff} at altitudes 1500 km, 850 km from WM sounding with DMSP satellite and IRI-2012 model.

From the WM sounding model the m_{eff} is ~1-2.5 which could require maximum H^+ 1 to 0.36 and maximum O^+ 0 to 0.64 (estimated from Equations 3.22, 3.23) in all L-shells in day side, at night side it is ~1. The 1st row of the figure 4.28 shows effective ion mass (m_{eff}) from the WM sounding (red) and the IRI-2012 model (black) with respect to L-shell at altitude 1500 km for day and night side of the magnetosphere. m_{eff} from the IRI-2012 model is ~1-2.5 a.m.u at L-shell below 2.5 for most of the cases. Above L-shell 2.5 there is a sudden increase in m_{eff}. It goes up to 4, which could require maximum H^+ of 0.2 and maximum O^+ of 0.8, at night side. However, the m_{eff} from the IRI-2012 model is comparable to that from the WM sounding for most of the cases. At altitude 850 km (2nd row), the m_{eff} from the WM sounding varies from ~1.5 to ~13 at day side and does not show any dependence on L-shell. This is comparable to the m_{eff} from the IRI-2012 model and the DMSP satellite data. At night side the m_{eff} from WM sounding generally varies between 1-5 and is comparable to m_{eff} from the IRI-2012 model and DMSP satellite data. The m_{eff} at this altitude at night side does not show any dependence on L-shell.

4.5.5 Transition height variations from WM sounding for different L-shells, comparison with IRI-2012 model
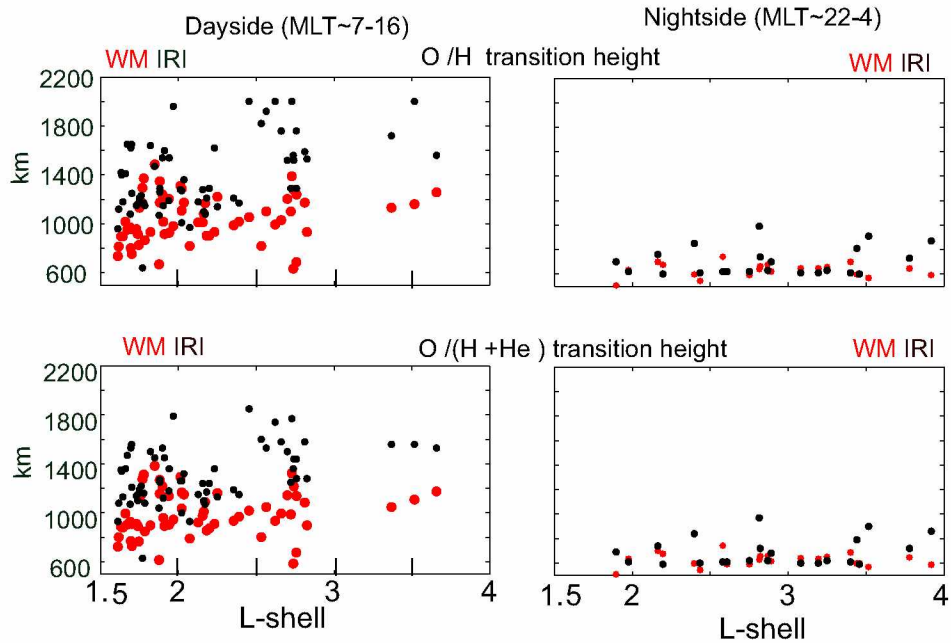
Figure 4.29 Transition height comparison of from WM sounding and IRI-2012 model. Comparison of O^+/H^+ transition height (1st row), $O^+/(H^++He^+)$ transition height (2nd row) from WM sounding model (red) and IRI 2012 (black) model with respect to L-shells for day and night side of the magnetosphere.

The transition height is defined as the height where the mass of the lighter ionic constituents is equal to the mass of the heavier ionic constituents. It is one of the parameters used to characterize electron density distribution. This transition height of the dominant ions corresponds to the transition of the main ionosphere to the plasmasphere (Lemaire and Gringauz, 1998). It is also a sensitive indicator of solar EUV ionizing flux and the dynamics of the topside ionosphere (MacPherson et al., 1998). Figure 4.29 plots two types of transition heights, O^+/H^+ (1st row) and $O^+/(H^++He^+)$ (2nd row) from the WM sounding (red) and the IRI-2012 model (black). O^+/H^+ and $O^+/(H^++He^+)$ transition heights from WM sounding vary between $\sim$700 km and $\sim$1400 km for day side and $\sim$500-800 km for night side. For day side, L-shells below $\sim$2.5, both types of transition heights from the IRI-2012 model are $\sim$100-300 km higher than those from WM sounding. Above L-shells $\sim$2.5, there is a sudden enhancement of both types of transition heights from the IRI-2012 model. This trend is not seen in the transition heights from the WM sounding. Above these L-shells, the IRI-2012 model overestimates the transition heights by $\sim$800-1000 km relative to the WM

sounding. At night side, both types of transition heights from the IRI-2012 model and the WM sounding are comparable and both are lower than the transition heights from day side. Previous measurements of O^+/H^+ transition heights during solar minima from C/NOFS, COSMIC, and GPS-TEC satellites showed that the O^+/H^+ transition height resides near 450-500 km at night and rises to only 650-850 km during the day (Heelis et al., 2009; Tulsi Ram et al., 2010). He^+/O^+ is ~1 order of magnitude lower than H^+/O^+ during the solar minimum and ~0.5 order lower at nighttime. A higher He^+/O^+ ratio indicates a lower O^+/He^+ transition altitude compared to the O^+/H^+ transition altitude (Borgohain and Bhuyan, 2010). During night time, ion temperature is low because of the absence of solar radiation. The low ion temperature will result in the small scale height and thus lower transition height (Liu et al., 2008; MacPherson et al., 1998; Titheridge, 1976). The neutral wind can drag the ions along the field line and influence the transition height also (Yue et al., 2010). Another important parameter, $R_{flh,max1}$ (altitude corresponding to $f_{lh,max1}$) varies between ~900 km to ~1800 km for day side, between ~700 km to ~1000 km at night side from WM sounding. $R_{flh,max1}$ is related to transition height, the higher the transition height, the higher is the $R_{flh,max1}$.

The transition heights in Figure 4.30 are plotted with respect to case numbers which are given according to occurrence time. In this case, all the cases are from August 2005 to December 2005. We see a decreasing trend in both the types of transition heights at day side from the WM sounding (red dots) with respect to case numbers, which means with respect to occurrence time August to December 2005. The reason for this is that the heavier ion O^+ decreases from the month August to December 2005. During winter, lower day time O^+ concentration was observed by the OGO satellite (Brinton et al., 1969) and AE satellites (Craven et al., 1995). Yue et al., (2010) have shown from C/NOFS satellite data that the O^+/H^+ transition height is higher in summer than in winter during solar minima.
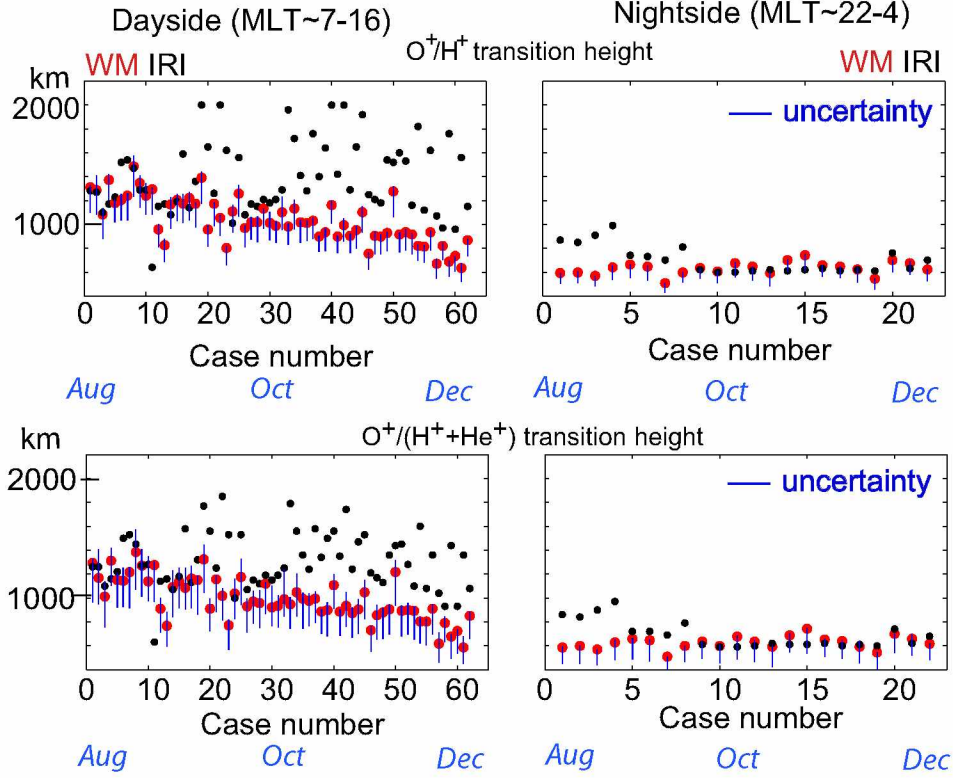
Figure 4.30 Transition height from WM sounding with uncertainty limits. Comparison of O^+/H^+ transition height (1st row), $O^+/(H^++He^+)$ transition height (2nd row) from WM sounding model (red) and IRI-2012 model (black) with respect to case numbers for day and night side of the magnetosphere.

Based on the Equations 4.3.3, 4.3.3 uncertainty of transition height is calculated for all 82 cases for which raytracing analysis was done (shown in Figure 4.1). Figure 4.30 shows uncertainty in O^+/H^+ and $O^+/(H^++He^+)$ transition heights (blue lines) with respect to case numbers. Uncertainty in transition height lies in the range of ~200-500 km in day side, for night side cases it is ~150-300 km. The uncertainty at night side is lower than at day side due to lower concentration of heavier ions. The black dots represent the transition heights calculated from the IRI-2012 model. For day side cases for L-shell<~2.5, both types of transition heights from the IRI-2012 model lie with the uncertainty limits of the WM sounding, but for L-shell>~2.5 the transition heights from IRI-2012 model is ~2 times higher than the transition heights from WM sounding model. For most of the cases on the night side, the transition heights from the IRI-2012 model are within the uncertainty limit of the WM sounding.

Chapter 5 Conclusions and future work

5.1 Summary and conclusion

WM sounding by the IMAGE/RPI satellite has allowed us to explore the plasmaspheric density at low altitude (below 5000 km) with the help of several features of WM echoes. The achievement of this thesis is that many new features of WM echoes were found for the first time. This includes double SR echoes, overlapping NI-SR and MR echoes, simultaneous occurrence of MR, OI-SR and NI-SR echoes. For the first time, we have been able to find electron and ion density (O^+, H^+ and He^+) profiles along Earth's magnetic field lines (covering L-shells 1.6 to 4) within the plasmasphere up to the Earth-ionosphere boundary. These results are very important in terms of space plasma studies and space weather predictions. Previous empirical models of plasma densities in the inner magnetosphere have been developed by statistical, time-dependent averaging of a large set of in situ measurements. In-situ measurements of ions are available from past satellites (AE, OGO, ISIS, Alouette, DMSP) below 1500 km altitude. But field aligned ion densities covering a wide range of L-shells (1.6-4) and altitudes (90-5000 km) are not available. The ion densities along the field line play a vital role in plasma depletion and refilling during geomagnetic storm times. Geomagnetic storms can cause damage to geosynchronous satellites, communication satellites and temporary loss of electrical power over a large region. The O^+, He^+ ions are important constituents for storm time ring currents, which consist of the order of keV of energy trapped in Earth's magnetic field. Ion composition measurements can provide information about the acceleration and transport mechanism up to the energy range of ring current (Williams 1985, Keika et al., 2013). The peak of He^+ density layer is near O^+/H^+ transition height, which is the transition from heavier ion dominated region of the ionosphere to lighter ion dominated region of the plasmasphere and hence important for ionosphere-plasmasphere coupling (Gonzalez and Sulzar, 1996). Solar EUV radiation at 30.4 nm is scattered by the He^+ in the plasmasphere and is a good source for imaging the plasmasphere (Sandel et al., 2001). The empirical models of ion densities in IRI-2012 and GCPM do not agree with experimental in-situ ion composition studies. For the first time with IMAGE/RPI data, this

dissertation has added to previous efforts by providing nearly instantaneous measurements of the field-aligned ion and electron densities. These new sets of results provide a very good database for future improvements of empirical models at low altitudes for electron and, most importantly, for ion densities. Further exploration of the RPI sounding data for WM echoes along with the echoes of other modes (Z-mode, R-X mode, L-O mode) and in combination with in situ data provided by the passive measurements of RPI and other satellite instruments can be expected to yield even more comprehensive empirical density models of the plasmasphere, with dependence on geophysical location, geomagnetic activity, and solar wind parameters.

As part of this dissertation, a detailed statistical data survey has been performed for whistler mode echoes during the IMAGE satellite's lifetime (2000 to 2005). A total of 10 programs suitable for whistler mode observation (below altitude 5000 km and frequency range 6 kHz to 1000 kHz) have been surveyed. This consists of surveys of ~21,000 plasmagrams. There are ~450 cases of MR-WM echoes, ~2500 cases of SR-WM echoes, ~160 cases of MR-WM echoes observed simultaneously with SR-WM echoes, and ~30 cases of double SR echoes. These echoes include discrete, multipath, and diffuse echoes. Most of the diffuse SR-WM echoes are observed in high latitude regions (above 60°). The observed occurrence rate of WM echoes is ~20% of transmissions. The main types of combination of WM echoes include 1) MR+OI-SR WM echoes; 2) MR+NI+OI-SR echoes; 3) MR+NI-SR echoes, only one of which is observed; 4) OI-SR+NI-SR echoes, and 5) NI-SR echoes from both hemispheres. The other examples shown are successive MR echoes, successive SR echoes along the orbit, MR echoes-, and SR echoes observed near the plasmapause. MR echoes observed at different geomagnetic conditions and SR echoes observed at different geomagnetic and solar conditions. MR echoes are observed in all MLTs and only in the northern hemisphere due to the limitation of program transmissions by the IMAGE/RPI. SR echoes are observed in all MLTs and latitudes. The double SR echoes are observed at altitude below 2000 km. The occurrence of MR echoes is higher in quiet times than in moderate or disturbed times, whereas more SR echoes are observed in disturbed times than moderate and quiet times. SR-WM echoes do not show any dependence on solar activity.

The Stanford 2-D raytracing program which was used to simulate whistler mode wave propagation has been improved to run from MATLAB using MEX files. A MATLAB based graphical user interface (GUI) tool has been developed to calculate ray parameters along ray paths.

Ray tracing simulations have been performed for 82 WM cases lying in the L-shell range 1.6-4, below 5000 km altitude for both day and night side of the magnetosphere over a wide range of

geomagnetic conditions (Kp 0+ to 4+) during solar minima. The electron and ion density profiles obtained from this analysis were compared with in situ measurements on the IMAGE (passive sounding; N_e), DMSP ($\sim$850 km; N_e and ions), CHAMP ($\sim$350 km; N_e), Alouette ($\sim$500-2000 km; N_e and ions), ISIS ($\sim$600-3500 km; N_e), and AE ($\sim$130-2000 km; ions) satellites, bottom side sounding from nearby ionosonde stations (N_e), and those by the GCPM and the IRI-2012 models.

Based on this analysis we found that:

1. Electron density (N_e) shows a decreasing trend from L-shell 1.6 to 4 on both day and night side of the plasmasphere up to an altitude $\sim$850 km. However, the quality of the linear fit (R) to the log of N_e is less than 0.5. The reason is that N_e is widely scattered for a given L-shell.

2. Below 1500 km the electron density is higher at day side than night side MLT (Magnetic Local Time). Above this altitude, significant MLT dependence of electron density is not seen. The GCPM and IRI models show MLT dependence above 1500 km. N_e values from those models are $\sim$15-25% higher in day side than night side. Ozhogin et al., (2012) model, derived from IMAGE/RPI free space mode data, does not show MLT dependence and is in good agreement with the N_e values from the WM sounding above 2000 km.

3. At an altitude of 850 km, for both at day side and night side of the magnetosphere, N_e values from the WM sounding, IRI-2012 model, DMSP satellites are comparable. Above $\sim$2000 km altitude, the GCPM underestimates N_e by $\sim$30-90% relative to RPI passive measurements and WM sounding results.

4. The method (used in this dissertation for electron and ion density determination) calculates the effective ion mass (m_{eff}), and for a given value of m_{eff}, there can be more than one combination of ion compositions. Hence, there could be more than one model fitting the observed data of WM echoes. This gives rise to the uncertainty in ion composition.

5. Ion density measurements from the AE, ISIS-2, DMSP satellites are within $\sim$10-35% of the ion densities from WM sounding. Since ISIS-2 and AE satellites are not of the same time period as IMAGE, the data are chosen according to same season and solar activity as the IMAGE satellite data used for the analysis. ISIS-2 data are available for the altitude 1400 km and AE data are available in the altitude range from $\sim$100-1000 km and $\sim$1500-2500 km.

6. For day side, from WM sounding results, O^+/H^+ transition heights lie in the range of 800 to 1500 km, $O^+/(H^++He^+)$ transition heights lie in the range of $\sim$500-1200 km. Both the transition heights from the IRI-2012 model lie in the range of $\sim$1200-2000 km for day side. For night side from the WM sounding results, both types of transition heights are in the range of $\sim$500-1200 km,

117

which is comparable to that of the IRI-2012 model. The calculated uncertainty for both transition heights is ~250-400 km.

7. m_{eff} on the day side is more than two times higher than on the night side below altitude 1500 km. Above this altitude, the m_{eff} is ~1. The range of m_{eff} at 1500 km is ~1.5 to 2.8, whereas at night side it is ~1. At 850 km the range is widely spread (~1.8-13) at day side and is comparable to DMSP data. On the night side, the range lies within ~1.2-5 in most cases.

8. The F2 peak for day side from the WM sounding results lies in the range of ~2-5 MHz, from ionosonde and IRI-2012 model the F2 peak lies in the range of ~5-8 MHz. At night side the F2 peak from the WM sounding results lies in the range of ~2-4 MHz and are comparable to the ionsonde data and the IRI-2012 model. The hmF2 (height of F2 peak) at day side from the WM sounding lies between ~180-300 km. This range is comparable to that of the ionosonde data, but the IRI-2012 model shows almost constant hmF2 at ~250 km. On the night side, the hmF2 from the WM sounding lies between ~180-250 km, while the IRI-2012 model shows nearly constant hmF2 at ~350 km.

5.2   Future work

This research has led to the following recommendations for future work:

The database developed for N_e and ion densities covering L-shells 1.6-4 below altitude 5000 km can be used for empirical model development and also for future versions of the IRI model. The IRI model has limitations in the ion densities as there are not sufficient data available for ions from previous satellites and other sources. Our database can be a great advantage here.

The analysis of a large number of SR echoes (~2500) observed over the years 2000 to 2005 and covering a wide range of solar activity can provide the N_e database over a wide L-shell range and the dependence of N_e on solar activity. Raytracing analysis shows two types of NI-SR echoes at low altitude in the equatorial region, but we do not observe them in our data. Further analysis can give more information in this regard.

The plasmagrams on the night side of the magnetosphere are in general more noisy than day side. This led to difficulty in measurements of echo cut-offs and time delays. Most of the MR echoes in the night side do not show the high rise in time delay near upper cut-offs. This is because the echoes near the upper cut-off are not observed on night side plasmagrams. The FAIs scatter the signal away from the satellite and also show noise on the plasmagrams. The analysis of these FAIs present in the night side is another recommendation for future work.

The diffuse SR echoes mostly lie in the high latitude region above an altitude of 1500 km. Below this altitude, the echoes are discrete in the high latitude regions. The presence of field aligned irregularities (FAIs) in the high latitude region scattered the WM signal causing the echoes to be diffuse. Further analysis of diffuse echoes can give ranges for locations, size, and density changes of FAIs.

The occurrence of SR echoes shows a seasonal dependence. Greater numbers are observed in the winter than in summer. Hence, further analysis of these echoes can lead to the understanding of seasonal dependence of N_e.

The study of WM natural emissions observed on dynamic spectra in relation to the WM echoes observed from the plasmagrams can provide a better understanding of reflection and scattering of the WM signals and also their generation mechanisms. These studies can also lead to the understanding of wave particle interaction and population in the radiation belt.

These ion density measurements are very important, as the ion density profile along the magnetic field line is poorly known, and can provide better understanding of global cold plasma distribution inside the plasmasphere at low altitudes and bridge the gap between high topside ionosphere/plasmasphere measurements. These results can serve as a framework for future advancement in empirical descriptions of regional and global plasma. The results will provide a vital resource in the engineering design and operation of future sounders on spacecraft for the WM range in terms of frequency and the virtual range to cover more ion density measurements in the low altitude region in a wide range of MLTs and solar and geophysical conditions.

References

Altadill, D., J.M. Torta, E. Blanch (2009), Proposal of new models of the bottomside B0, B1, parameters for IRI, *Adv. Space Res.*,43, 1825.

Angerami, J. J., and J. O. Thomas (1964), Studies of planetary atmosphere: 1. The distribution of electrons and ions in the Earth's exosphere. *J. Geophys. Res.*, 69, 4537.

Aponte, N., C. G. M. Brum, M. P. Sulzer, and S. A. Gonza lez (2013), Measurements of the O+ to H+ transition height and ion temperatures in the lower topside ionosphere over Arecibo for equinox conditions during the 20082009 extreme solar minimum, *J. Geophys. Res.*, 118, 44654470, doi:10.1002/jgra.50416.

Barrington, R. E., J. S. Belrose, and G. L. Nelms (1965), Ion composition and temperature at 1000 km as deduced from simulataneous observations of a VLF plasma resonance and topside sounding data from the Alouette I satellite, *J. Geophys. Res.*, 70, 1647-1664.

Barrington, R. E. (1969), Ionospheric ion composition deduced from VLF observations, *Proc. of the IEEE*, 57(6), 1036.

Bartels, J., N. H. Heck, and H. F. Johnston (1939), The three-hour-range index measuring geomagnetic activity, Terr. Magn., *Atmos. Elec.*, 44, 411.

Bauer, S. J. (1969), Diffusive Equilibrium in the topside Ionosphere, *Proceedings of the IEEE*, 57,6.

Benson, R. F., V. A. Osherovich, J. Fainberg, and B. W. Reinisch (2003), Classifcation of IMAGE/RPI-stimulated plasma resonances for the accurate determination of magneto- spheric electron-density and magnetic field values, *J. Geophys. Res.*, 108(A5), 1207.

Benson, R. F., P. A. Webb, J. L. Green, L. Garcia, and B. W. Reinisch (2004), Magnetospheric electron densities inferred from upper-hybrid band emissions, *Geophys. Res. Lett.*, 31, L20803, doi:10.1029/2004GL020847.

Benson, R. F., Four Decades of Space-Borne Radio Sounding (2010), *The Radio Science Bulletin*, 333.

Berube, D., M. B. Moldwin, S.F. Fung and J. L. Green (2005), A plasmaspheric mass density model and constrains on its heavy ion concentration, *J. Geophys. Res.*, 110, A04212.

Bilitza, D. (1990), International Reference Ionosphere 1990, *Science Application Research*.

Bilitza, D. (1998), The E-and D-region in IRI, *Adv. Space Res.*, 21, 6, 871.

Bilitza, D. (2001), International Reference Ionosphere 2000, *Radio Sci.*, 36, 2, 261.

Bilitza, D. (2003), International Reference Ionosphere 2000: Examples of improvements and new features, *Adv. Space Res.*, 31, 3, 757.

Bilitza, D., X. Huang, B. W. Reinisch, R. F. Benson, H. K. Hills, and W. B. Schar (2004), Topside Ionogram Scaler With True Height Algorithm (TOPIST): Automated processing of ISIS topside ionograms, *Radio Sci.*, 39, RS1S27, doi:10.1029/2002RS002840.

Bilitza, D., B. W. Reinisch, S. M. Radicella, S. Pulinets, T. Gulyaeva, and L. Triskova (2006), Improvements of the International Reference Ionosphere model for the topside electron density profile, *Radio Sci.*, 41, RS5S15, doi:10.1029/2005RS003370.

Bilitza, D., B. W. Reinisch (2008), International Reference Ionosphere 2007: Improvements and new parameters, *Adv. in Space Res.*, 42, 599609.

Bilitza, D. (2011), The international reference ionosphere toaday and in the future, *J. Geod.*, 909.

Bilitza, D., D. Altadill, Y. Zhang, C. Mertens, V. Truhlik, P. Richards, L.A. McKinnell, and B. Reinisch (2014), The International Reference Ionosphere 2012 a model of international

collaboration, *J. Space Weather Space Clim.*, 4, A07.

Binsack, J.H. (1967), Plasmapause observations with the M.I.T. experiment on IMP 2., *J. Geophys. Res.*, 72(21), 52315237.

Borgohain, A., and P. K. Bhuyan (2010), Solar cycle variation of ion densities measured by SROSS C2 and FORMOSAT 1 over Indian low and equatorial latitudes, *J. Geophys. Res.*, 115, A04309, doi:10.1029/2009JA014424.

Brace, L. H., B. M. Reddy, and H. G. Mayr (1967), Global behavior of the ionosphere at 1000 kilometers altitude, *J. Geophys. Res.*, 72, 265-284.

Breig, E. L., J. H. Hoffman (1975), Variations in ion composition at middle and low latitudes from ISIS-2 satelliet, *J. Geophys. Res.*, 16, 2207.

Brinton, H. C., A. Pickett, H. A. Taylor Jr (1969), Diurnal and Seasonal Variation of Atmospheric Ion Composition; Correlation with Solar Zenith Angle, *J. Geophys. Res.*, 74, 16.

Burch, J. L. (2000), IMAGE mission overview, *Space Sci. Rev.*, 91,114.

Burtis, W. J. (1974), Users's Guide to the Stanford VLF Ray Tracing Program, RadioSci. Lab., Stanford Electr. Lab., Stanford University., Stanford, Calif., 1974.

Calvert, W., R. W. Knecht, and T. E. VanZandt (1964), Ionosphere Explorer I satellite: first observations from the fixed-frequency topside sounder Science1, *J. Geophys. Res.*, 46, 391-395.

Calvert, W. (1966), Steep Horizontal Electron-Density Gradients in the Topside F Layer, *J. Geophys. Res.*, 71, 15.

Carpenter, D. L. (1963a), Whistler evidence of a 'knee' in the magnetospheric ionization density profile, *J. Geophys. Res.*, 68, 1675.

Carpenter, D. L. (1963b), Whistler Measurements of Electron Density and Magnetic Field Strength in the Remote Magnetosphere, *J. Geophys. Res.*, 68, 12.

Carpenter, D. L. and R. L. Smith (1964), Whistler measurement of electron density in the magnetosphere, *Rev. Geophys.*, 2, 45.

Carpenter, D. L. (1981), A study of the Outer Limits of Ducted Whistler Propagation in the Magnetosphere, *J. Geophys.Res.*, 86, A2, 839.

Carpenter, D. L., R. R. Anderson, T. F. Bell, T. R. Miller (1981), A comparison of equatorial electron densities measured by whistlers and satellite radio technique, *Geophys. Res. Lett.*, 8, 1107.

Carpenter, D. L. (1988), Remote sensing of the magnetospheric plasma by means of whistler mode signals, *Rev. Geophys.*, 26, 535.

Carpenter, D. L., and R. R. Anderson (1992), An ISEE/whistler model of equatorial electron density in the magnetosphere, *J. Geophys. Res.*, 97(A2), doi:10.1029/91JA01548.

Carpenter, D. L., R. R. Anderson, W. Calvert, M. B. Moldwin (2000), CRRES observations of density cavities inside the plasmasphere, *J. Geophys.Res.*, 105, A10, 23,323-23338.

Carpenter, D. L., T. F. Bell, U. S. Inan, R. F. Benson, V. S. Sonwalkar, B. W. Reinisch, and D. L. Gallagher (2003), Z-mode sounding within propagation cavities and other inner magnetospheric regions by the RPI instrument on the IMAGE satellite, *J. Geophys. Res.*, 108, 1421, doi:10.1029/2003JA010025, A12.

Carpenter, D. L., T. F. Bell, D. Chen, D. Ng, C. Baran, B. W. Reinisch, and I. Galkin (2007), Proton cyclotron echoes and a new resonance observed by the Radio Plasma Imager instrument on the IMAGE satellite, *J. Geophys. Res.*, 112, A08208, doi:10.1029/2006JA012139.

Chandra, S., B. E. Tray, Jr., J. L. Dorley and R. E. Bourdeau (1970), OGO-4 observations of ion compositions and temperatures in the top side ionosphere, *J. Geophys. Res.*, 75, 3867.

Chappell, C. R., K. K. Harris, and G. W. Sharp (1971), The dayside of the plasmasphere, *J. Geophys. Res.*, 76(31), 76327647, doi:10.1029/JA076i031p07632.

Chen, Y., L. Liu, and H. Le (2008), Solar activity variations of nighttime ionospheric peak

electron density, *J. Geophys. Res.*, 113, A11306, doi:10.1029/2008JA013114.

Coisson, P., B. Nava, S.M. Radicella (2009), On the use of NeQuick topside option in IRI-2007, *Adv. in Space Res.*, 43, 1688-1693.

Comfort, R. H., I. T. Newberry and C. R. Chappell (1998), Preliminary Statistical Survey Of Plasmaspheric Ion Properties From Observations By DE 1/RIMS, Geophysical Monograph Series, 44.

Craven, P. D., R. H. Comfort, P. G. Richards, J. M. Grebowsky, (1995), Comparison of modeled N+, O+, H+ and He+ in the midlatitude ionosphere with mean density and temperatures from Atmospheric Explorer, *J. Geophys. Res.*, 100, 257.

Craven, P. D., D. L. Gallagher and R. H. Comfort (1997), Relative concentration of He+ in the inner magnetosphere as obtained by DE1 retarding ion mass spectrometer, *J. Geophys. Res.*, 102, 2279.

Darrouzet, F., D. L. Gallagher, N. A., D. L. Carpenter, I. Dandouras, P. M.E. Dcrau, J. De Keyser, R. E. Denton, J. C. Foster, J. Goldstein, M. B. Moldwin, B. Reinisch, B. R. Sandel, J. Tu (2009), *Space Sci Rev.*, 145: 55106 DOI 10.1007/s11214-008-9438-9.

Dent, Z. C., I. R. Mann, F. W. Menk, J. Goldstein, C. R. Wilford, M. A. Clilverd, and L. G. Ozeke (2003), A coordinated ground-based and IMAGE satellite study of quiet-time plasmaspheric density profiles, *Geophys. Res. Lett.*, 30(12), 1600, doi:10.1029/2003GL016946.

Denton, R. E., and D. L. Gallagher (2000), Determining the mass density along magnetic field lines from toroidal eigenfrequencies, *J. Geophys. Res.*, 105(A12), 27,717.

Denton, R. E., E. G. Miftakhova, M. R. Lessard, R. Anderson, and J. W. Hughes (2001), Determining the mass density along magnetic field lines from toroidal eigenfrequencies: Polynomial expansion applied to CRRES data, *J. Geophys. Res.*, 106, 29,915.

Denton, R. E., J. Goldstein, and J. D. Menietti (2002), Field line dependence of magnetospheric electron density, *Geophys. Res. Lett.*, 29(24), 2205, doi:10.1029/2002GL015963.

Denton, R. E., J. D. Menietti, J. Goldstein, S. L. Young, and R. R. Anderson (2004), Electron density in the magnetosphere, *J. Geophys. Res.*, 109, A09215, doi:10.1029/2003JA010245.

Denton, R. E., J. Goldstein, D. H. Lee, R. A. King, Z. C. Dent, D. L. Gallagher, D. Berube, K. Takahashi, M. Nose, D.Milling, and F. Honary (2006), Realistic magnetospheric density model for 29 August 2000, *J. Atmos. Sol. Terr. Phys.*, 68, 615.

Denton, R. E., Y. Wang, P. A. Webb, P. M. Tengdin, J. Goldstein, J. A. Redfern, and B. W. Reinisch (2012), Magnetospheric electron density long-term (>1 day) refilling rates inferred from passive radio emissions measured by IMAGE RPI during geomagnetically quiet times, *J. Geophys. Res.*, 117, A03221, doi:10.1029/2011JA017274.

Fallen, C. T., J. A. Secan, and B. J. Watkins (2011), In-situ measurements of topside iono-sphere electron density enhancements during an HF-modification experiment, *Geophys. Res. Lett.*, 38, L08101, doi:10.1029/2011GL046887.

Friedrich, M., K.M. Torkar (1992), An empirical model of the nonauroral D region, *Radio Sc.*, 27, 6, 945.

Fu, H. S., J. Tu, J. B. Cao, P. Song, B. W. Reinisch, D. L. Gallagher, and B. Yang (2010), IMAGE and DMSP observations of a density trough inside the plasmasphere, *J. Geophys. Res.*, 115, A07227, doi:10.1029/2009JA015104.

Galkin, I. A., (2004), A pre-attentive vision model for automated data elploration applied to space plasma remote sensing data, PhD thesis, University of Massachusetts Lowell.

Gallagher, D. L., P. D. Craven, and R. H. Comfort (1988), An empirical model of the Earths plasmasphere, *Adv. Space Res.*, 8, 1524, doi:10.1016/0273-1177(88)90258-X.

Gallagher, D. L., P. D. Craven, and R. H. Comfort (2000), Global core plasma model, *J. Geophys. Res.*, 105, 18,819.

Goldstein, J., R. E. Denton, M. K. Hudson, E. G. Miftakhova, S. L. Young, J. D. Menietti, and D. L. Gallagher (2001), Latitudinal density dependence of magnetic field lines inferred from Polar plasma wave data, *J. Geophys. Res.*, 106(A4), 61956201, doi:10.1029/2000JA000068.

Goldstein, J., M. Spasojevic, P. H. Reiff, B. R. Sandel, W. T. Forrester, D. L. Gallagher, and B. W. Reinisch (2003), Identifying the plasmapause in IMAGE EUV data using IMAGE RPI in situ steep density gradients *J. Geophys. Res.*, 108, 1147.

Gonzalez, S.A., M. P. Sulzar (1996), Detection of He+ Layering in the topside ionosphere over Arecibo during equinox solar minimum condition, *Geophys. Res. Lett.*, 23, 18, 2509-2512.

Green, J. L. and B. W. Reinisch (2003), An overview of results from RPI on IMAGE, *Space Sci. Rev.*, 109, 183.

Grew, R. S., F. W. Menk, M. A. Clilverd, and B. R. Sandel (2007), Mass and electron densities in the inner magnetosphere during a prolonged disturbed interval, *Geophys. Res. Lett.*, 34, L02108, doi:10.1029/2006GL028254.

Gringauz, K. I. (1963), The structure of the Earth's ionized gas envelop of Earth from direct measurements in the USSR of local charge particle concentration., *Planetary and Space Sc.*, 11, 281-96.

Gringauz, K. I. and Bezrukikh (1976), Asymmetry of the Earth's Plasmasphere in the direction noon-midnight from PROGNOZ-1 and PROGNOZ-2 data, *J. Atm. Sol. Terres. Phys.*, 38, 1071.

Guiter, S. M., T. E. Moore, and G. V. Khazanov (1995), Modeling of O+ ions in the plasmasphere, *J. Geophys. Res.*, 100(A11), 2192121928, doi:10.1029/95JA02224.

Gurnett, D. A. and U. S. Inan (1988), Plasma wave observations with the Dynamics Explorer 1 spacecraft, *Rev. Geophys.*, 26, 285.

Hamilton, D.C., G. Gloeckler, F.M. Ipavich, W. Stdemann, B. Wilken, and, G. Kremser (1988), Ring current development during the great geomagnetic storm of February 1986. *J. Geophys. Res.*, 93: doi: 10.1029/88JA03625. issn: 0148-0227.

Haselgrove, J. (1955), Ray theory and a new method for ray tracing, paper presented at Conference on the Physics of the Ionosphere, pp. 355364, Phys. Soc. of London, London.

Hayakawa, M. (1995), Whistlers, in: Handbook of Atmospheric Electrodynamics, H. Volland (Ed.), CRC Press, Boca Raton, Florida, USA.

Hazra, S., V.S Sonwalkar, A. Reddy (2011), Whistler Mode Radio Sounding from IMAGE: Measurement of Electron Density, Ion Effective Mass,and Ion Composition in the Plasmasphere at Low Altitude (90-3000 km) Along Bo, AGU-Fall.

Hazra, S., V.S Sonwalkar, A. Reddy (2012), Field aligned electron and ion density distribution inside the plasmasphere below 4000 km using whistler mode radio sounding by RPI on IMAGE, AGU-Fall2012.

Heelis, R. A., W. R. Coley, A. G. Burrell, M. R. Hairston, G. D. Earle, M. D. Perdue, R. A. Power, L. L. Harmon, B. J. Holt, and C. R. Lippincott (2009), Behavior of the O+/H+ transition height during the extreme solar minimum of 2008, *Geophys. Res. Lett.*, 36, L00C03, doi:10.1029/2009GL038652.

Helliwell, R. A., and N. Brice (1964), Very low frequency emission periods and whistler mode group delays, *J. Geophys. Res.*, 69, 4704.

Helliwell, R. A. (1965), Whistlers and related Ionospheric Phenomena, Stanford Press, Stanford, California.

Hoffman, J. H., W. H. Dodson, C. R. Lippincott, and, H. D. Hammack (1974), Initial ion composition results from the Isis 2 satellite, *J. Geophys. Res.*, 79, 4246-4251.

Horwitz, J. L., R. H. Comfort, and C. R. Chappell (1990), A statistical characterization of plasmasphere density structure and boundary locations, *J. Geophys. Res.*, 95, 7937.

Huang, X., B. W. Reinisch, D. Bilitza, R. F. Benson (2002), Electron density profiles of the topside ionosphere, *Ann. Geophys.*, 45, 1.

Huttunen, K. E. J., H. E. J. Koskinen, and R. Schwenn (2002), Variability of magnetospheric storms driven by different solar wind perturbations, *J. Geophys. Res.*, 107(A7), doi:10.1029/2001JA900171.

Inan, U. S., and T. F. Bell, The plasmapause as a VLF wave guide, *J. Geophys. Res.*, 82, 2819, 1977.

Istomin, V. G. (1961), Variation in the positive ion concentration with altitude from data of mass spectrometry on 3rd satellite, *Planet Space Sci.*, 8, 179.

Jackson, J. E., R. Erwin, J. H. Whitteker (1980), Mini-Review on Topside Sounding, *IEEE Transactions on antennas and propagation*, 28, 2.

Johnson, C. Y. (1966), Ionospheric composition and density from 90 to 1200 kilometers at solar minimum, *J. Geophys. Res.*, 71(1), 330332, doi:10.1029/JZ071i001p00330.

Johnston, W. R. (2007), The role of the plasmasphere in radiation belt particle energization and loss, Ph.D. research proposal, University Texas Dallas.

Kakinami, Y, S. Watanabe b, K.-I. Oyama (2008), An empirical model of electron density in low latitude at 600 km obtained by Hinotori satellite, *Adv. in Space Res.*, 41, 14951499.

Kane, R. P. (1992), Sunspots, solar radio noise, solar EUV and ionospheric foF2, *J. Atmos. Terr. Phys.*, 54, 463 466.

Kane, R. P. (2003), Solar EUV and ionospheric parameters: A brief assessment, *Adv. Space Res.*, 32(9), 17131718.

Kawamura, S., N. Balan, Y. Otsuka, and S. Fukao (2002), Annual and semiannual variations of the midlatitude ionosphere under low solar activity, *J. Geophys. Res.*, 107(A8), 1166, doi:10.1029/2001JA000267.

Keika, K., L. M. Kistler, and P. C. Brandt (2013), Energization of O+ ions in the Earths inner magnetosphere and the effects on ring current buildup: A review of previous observations and possible mechanisms, *J. Geophys. Res.*, 118, 44414464, doi:10.1002/jgra.50371.

Kelly, M.C. (2009), The Earth's Ionosphere, Volume 96, Second Edition: Plasma Physics and Electrodynamics., Academic Press.

Keyser De J., D.L. Carpenter, F. Darrouzet, D.L. Gallagher, J. Tu (2008), CLUSTER and IMAGE: New ways to study the Earths plasmasphere. *Space Sci. Rev.*, 145: 753 DOI 10.1007/s11214-008-9464-7.

Kim, E., J. K. Chung, Y. H. Kim, S. Hong, J. Cho (2011), A climatology study on ionospheric F2 peak over Anyang, Korea, *Earth, moon and planets*, 63, 335349.

Kimura, I. (1966), Effects of ions on whistler-mode ray tracing, *Radio Sci.*, 1, 269.

Lean, J. L., O. R. White, W. C. Livingston, and J. M. Picone (2001), Variability of a composite chromospheric irradiance index during the 11-year activity cycle and over longer time periods, *J. Geophys. Res.*, 106, 10,645 10,658.

LeDocq, M. J., Gurnett, D. A. and Anderson R. R. (1994), Electron number density fluctuations near the plasmapause observed by CEEES spacecraft. *J. Geophys. Res.*, 99, 23661-71.

Lei, J., L. Liu, W. Wan, and S.-R. Zhang (2005), Variations of electron density based on long-term incoherent scatter radar and ionosonde measurements over Millstone Hill, *Radio Sci.*, 40, RS2008, doi:10.1029/2004RS003106.

Lemaire, J. (1986), The plasma transport in the plasmasphere., *Ade. Space Res.*, 6, 3,157175.

Lemaire, J., K. I. Gringauz (1998), The Earth's Plasmasphere, Cambridge University Press.

Li, J. (2004), Measurement of electron density in the Earth's Magnetosphere using discrete whistler mode echoes observed on the IMAGE satellite, Master's thesis, University of Alaska Fairbanks, Fairbanks, Alaska.

Liu, J. Y., Y. I. Chen, and J. S. Lin (2003), Statistical investigation of the saturation effect in the ionospheric foF2 versus sunspot, solar radio noise, and solar EUV radiation, *J. Geophys. Res.*, 108(A2), 1067, doi:10.1029/2001JA007543.

Liu, L., X. Luan, W. Wan, J. Lei, and B. Ning (2004), Solar activity variations of equivalent winds derived from global ionosonde data, *J. Geophys. Res.*, 109, A12305, doi:10.1029/2004JA010574.

Liu, L., W. Wan, and B. Ning (2006), A study of the ionogram derived effective scale height around the ionospheric hmF2, *Ann. Geophys.*, 24, 851 860.

Liu, H., C. Stolle, M. Forster, and S. Watanabe (2007), Solar activity dependence of the electron density in the equatorial anomaly regions observed by CHAMP, J. Geophys. Res., 112, A11311, doi:10.1029/2007JA012616.

Liu, L.,He, M.,Wan, W.,Zhang, M.-L. (2008), Topside ionospheric scale heights retrieved from constellation observing system for meteorology, ionosphere, and climate radio occultation measurements, *J. Geophys. Res.*,113, A10304,doi:10.1029/2008JA013490.

Liu, L., Y. Chen, H. Le, V. I. Kurkin, N. M. Polekh, and C. C. Lee (2011a), The ionosphere under extremely prolonged lowsolar activity, *J. Geophys. Res.*,116, A04320, doi:10.1029/2010JA016296.

Liu, L., H. Le, Y. Chen, M. He, W. Wan, and X. Yue (2011b), Features of the middle and low latitude ionosphere during solar minimum as revealed from COSMIC radio occultation measurements, *J. Geophys. Res.*, 116, A09307, doi:10.1029/2011JA016691.

Luan, X., W. Wang, A. Burns, S. C. Solomon, and J. Lei (2008), Midlatitude nighttime enhancement in F region electron density from global COSMIC measurements under solar minimum winter condition, *J. Geophys. Res.*, 113, A09319,doi:10.1029/2008JA013063.

Luhr, H., and C. Xiong (2010), IRI2007 model overestimates electron density during the 23/24 solar minimum, *Geophys. Res. Lett.*, 37, L23101, doi:10.1029/2010GL045430.

MacPherson, B., S. A. Gonzalez, G. J. Bailey, R. J. Moffett, and M. P. Sulzer (1998), The effects of meridional neutral winds on the O+H+ transition altitude over Arecibo, *J. Geophys. Res.*, 103, 29,183 29,198, doi:10.1029/98JA02660.

Masson, A., O. Santolk, D. L. Carpenter, F. Darrouzet, P. M. E. Dcrau, F. El-Lemdani Mazouz, J. L. Green, S. Grimald, M. B. Moldwin, F. Nemec, V. S. Sonwalkar (2009), Advances in Plasmaspheric Wave Research with CLUSTER and IMAGE Observations, *Space Sci Rev.*, 145: 137191, DOI 10.1007/s11214-009-9508-7.

Marinov, P. I. Kutievb, S. Watanabe (2004), Empirical model of O+H+ transition height based on topside sounder data, *J. Adv. Space Res.*, 34, 9, 20212025.

Matsui, H., J. C. Foster, D. L. Carpenter, I. Dandouras, F. Darrouzet, J. De Keyser, D. L. Gallagher, J. Goldstein, P. A. Puhl-Quinn, C. Vallat (2009), Electric Fields and Magnetic Fields in the Plasmasphere: A Perspective from CLUSTER and IMAGE, *Space Sci Rev.*, 145: 107135, DOI 10.1007/s11214-008-9471-8.

McNamara, L. F. (2006), Quality figures and error bars for autoscaled Digisonde vertical incidence ionograms, *Radio Sci.*, 41, RS4011, doi:10.1029/2005RS003440.

McNamara, L. F., D. L. Cooke, C. E. Valladares, and B. W. Reinisch (2007), Comparison of CHAMP and Digisonde plasma frequencies at Jicamarca, Peru, *Radio Sci.*, 42, RS2005, doi:10.1029/2006RS003491.

Meng, C. I. and K. Liou (2002), Global auroral power as an index for geospace disturbances, *Geophys. Res. Lett.*, 29, 1600.

Menvielle, M., T. Iyemori, A. Marchaudon, and M. Nose (2011), Geomagnetic Observations and Models, IAGA Special Sopron Book Series 5, 183, DOI 10.1007/978-90-481-9858-0-8, Springer Science+Business Media B.V.

Mielich, J. and J. Bremer (2013), Long-term trends in the ionospheric F2 region with differentDsisoculsasiorns activity indices, *Ann. Geophys.*, doi:10.5194/angeo-31-291-2013.

Migoya-Orue, Y.O., S.M. Radicella, B. Nava (2013), Comparison of topside electron density computed by ionospheric models and plasma density observed by DMSP satellites. *J. Adv. Space Res.*, http://dx.doi.org/10.1016/j.asr.2013.01.032.

Miller, N. J. and L. H. Brace (1969), Some winter characteristics of northen high latitude ionosphere, *J. Geophys. Res.*, 74, 5752.

Moldwin, M. B., M. F. Thompson, S. J. Bame D. J. McComas D.J. and G. D. Reeves (1995), The fine structure of the outer plasmasphere., *J. Geophys. Res.*, 100, 8021-9.

Moldwin, M. B., L. Downward, H. K. Rassoul, R. Amin, and R. R. Anderson (2002), A new model of the location of the plasmapause: CRRES results, *J. Geophys. Res.*, 107(A11), 1339, doi:10.1029/2001JA009211.

Mosier, S. R., M. L. Kaiser, and L.W. Brown (1973) Observation of noise band associated with upper hybrid resonance by Imp 6 radio astronomy experiment, *J. Geophy. Res.*, 78, 1673.

Mozer, F. S., C. A. Cattell, M. Temerin, R. B. Torbest, S. Von Glinski, M. Woldorff and J. Wygant (1979), The dc and ac electric field, plasma density, plasma temperature and field allighned current experiment on S3-3 satellite, *J. Geophys. Res.*, 84, 5875.

Nsumei, P. A., X. Huang, B. W. Reinisch, P. Song, V. M. Vasyliunas, J. L. Green, S. F. Fung, R. F. Benson, and D. L. Gallagher (2003), Electron density distribution over the northern polar region deduced from IMAGE/radio plasma imager sounding, *J. Geophys. Res.*, 108, 1078.

Nsumei, P. A., P. Song, B. W. Reinisch, J. Tu, and X. Huang (2008), Ionospheric electron upflow in the polar cap region: Derived from ISIS 2 measurements, *J. Geophys. Res.*, 113, A03312, doi:10.1029/2007JA012567.

Nsumei, P. A., B. W. Reinisch, X. Huang, D. Bilitza (2010), Comparing topside and bottomside-measured characteristics of the F2 layer peak, *Adv. in Space Res.*, 46, 974-983.

Nsumei, P., B. W. Reinisch, X. Huang, and D. Bilitza (2012), New Vary-Chap profile of the topside ionosphere electron density distribution for use with the IRI model and the GIRO real time data, *Radio Sci.*, 47, RS0L16, doi:10.1029/2012RS004989.

O'Brien, T. P., and M. B. Moldwin (2003), Empirical plasmapause models from magnetic indices, *Geophys. Res. Lett.*, 30(4), 1152, doi:10.1029/2002GL016007.

Ozhogin, P., J. Tu, P. Song, and B. W. Reinisch (2012), Field-aligned distribution of the plasmaspheric electron density: An empirical model derived from the IMAGE RPI measurements, *J. Geophys. Res.*, 117, A06225, doi:10.1029/2011JA017330.

Persoon, A. M., D. A. Gurnett and S. D. Shawhan (1983), Polar cap electron densities from

DE1 plasma wave obsevation, *J. Geophys. Res.*, 88, 10123.

Persoon, A. M., D. A. Gurnett, W. K. Peterson, J. H. White Jr., J. L. Burch, and J. L. Green (1988), Electron density depletion in the night side auroral zone, *J. Geophys. Res.*, 93, 1871.

Reddy, B. M., D. R. Lakshmi, and L. H. Brace (1969), Response of the 1000-Kilometer Ionosphere to Magnetic Storms, *Radio Sci.*, 4(9), 851857, doi:10.1029/RS004i009p00851.

Reinisch, B. W., D. M. Haines, K. Bibl, G. Cheney, I. A. Galkin, X. Huang, S. H. Myers, G. S. Sales, R. F. Benson, S. F. Fung, J. L. Green, W. W. L. Taylor, J. L. Bougeret, R. Manning, N. Meyer-Vernet, M. Moncuquet, D. L. Carpenter, D. L. Gallagher, and P. Rei (2000), The Radio Plasma Imager investigation on the IMAGE spacecraft, *Space Sci. Reviews*, IMAGE special issue, 91.

Reinisch, B. W. , X. Huang,D. M. Haines, I. A. Galkin, J. L. Green, R. F. Benson, S. F. Fung, W. W. L. Taylor, P. H. Reiff, D. L. Gallagher, J.-L. Bougeret, R. Manning, D. L. Carpenter, S. A. Boardsen (2001), First results from the Radio Plasma Imager on IMAGE *Geophys. Res. Lett.*, 28, 6.

Reinisch, B. W., X. Huang, P. Song, J. L. Green, S. F. Fung, V. M. Vasyliunas, D. L. Gallagher, and B. R. Sandel (2004), Plasmaspheric mass loss and refilling as a result of a magnetic storm, *J. Geophys. Res.*, 109, A01202, doi:10.1029/2003JA009948.

Reinisch, B. W., X. Huang, I. A. Galkin, V. Paznukhov, and A. Kozlov (2005), Recent advances in real-time analysis of ionograms and ionospheric drift measurements with Digisondes, *J. Atmos. Sol. Terr. Phys.*, 67, 10541062.

Reinisch B. W., M. B. Moldwin, R. E. Denton, D. L. Gallagher, H. Matsui, V. Pierrard, J. Tu (2009), Augmented Empirical Models of Plasmaspheric Density and Electric Field Using IMAGE and CLUSTER Data, *Space Sci. Rev.*, 145: 231261 DOI 10.1007/s11214-008-9481-6.

Rich, F. J., and P. J. Sultan (2000), Comparison of ion densities measured in the topside ionosphere at low latitudes and midlatitudes with calculations of ionospheric models over a full solar cycle, *Radio Sci.*, 35(5), 11931204, doi:10.1029/1999RS002284.

Richards, P. G. (2001), Seasonal and solar cycle variations of the ionospheric peak electron density: Comparison of measurement and models, *J. Geophys. Res.*, 106(A12), 12,803–12,819.

Richards, P. G., D. Bilitza, and D. Voglozin (2010), Ion density calculator (IDC): A new efficient model of ionospheric ion densities, *Radio Sci.*, 45, RS5007, doi:10.1029/2009RS004332.

Rishbeth, H. (1967), A review of ionospheric F region theory, *Proc IEEE*, 55, 16.

Rishbeth, H., and O. K. Garriott (1969), Introduction to Ionospheric Physics, 331 pp., Elsevier, New York.

Ritter, P., H. Luhr, S. Maus, A. Viljanen (2004), High-latitude ionospheric currents during very quiet times: their characteristics and predictability, *Ann. Geophys.*, 22, 2001.

Sandel, B. R., R. A. King, W. T. Forrester, D. L. Gallagher, A. L. Broadfoot, and C. C. Curtis (2001), Initial results from IMAGE extreme ultraviolet Imager, *Geophys. Res. Lett.*, 28, 1439.

Sawada, A., T. Nobata, Y. Kishi, I. Kimura, and H. Oya (1993), Electron density profile of the magnetosphere deduced from in situ electron density and wave normal direction of Omega signals observed by the Akebono (EXOS D) satellite, *J. Geophys. Res.*, 98, 11,267.

Scarf, F. L. and C. R. Chappell (1973), An association of magnetospheric whistler dispersion characteristics with changes in local plasma density, *J. Geophys. Res.*, 78, 1597.

Schulz, M. (1996), Eigenfrequencies of geomagnetic field lines and implications for plasma-density modeling, *J. Geophys. Res.*, 101(A8), 17,385.

Sethi, N. K., M. K. Goel, and K. K. Mahajan (2002), Solar cycle variations of fo F2 from IGY to 1990, *Ann. Geophys.*, 20, 1677–1685.

Shawhan, S. D. (1979), Magnetospheric plasma wave research 1975-1978, *Rev. Geophys.*, 17, 705.

Singh, N, J.L. Horwitz (1992), PlasmaphereR efilling: Recent Observationsa nd Modeling, *J. Geophys. Res.*, 92, A2, 1049-1079.

Sonwalkar, V., U. Inan, T. Bell, R. Helliwell, O. Molchanov, and J. Green (1994), DE 1 VLF observations during Activny wave injection experiments, *J. Geophys. Res.*, 99, 61736186.

Sonwalkar, V. S. (1995), Magnetospheric LF- VLF-, and ELF-waves, in: Handbook of Atmospheric Electrodynamics, H. Volland (Ed.), CRC Press, BocaRaton, Florida, USA.

Sonwalkar, V. S., U. S. Inan, T. L. Aggson, W. M. Farrell, and R. Pfaff (1995), Focusing of non-ducted whistlers by the equatorial anomaly, *J. Geophys. Res.*, 100, 7783.

Sonwalkar, V. S., X. Chen, J. Harikumar, D. L. Carpenter, and T. F. Bell (2001), Whistler-mode wave injection experiments in the plasmasphere with a radio sounder *J. Atmos. Solar-Terr. Phys.*, 63, 1199.

Sonwalkar, V. S., D. L. Carpenter, T. F. Bell, M. Spasojevic, U. S. Inan, J. Li, X. Chen, A. Venkatasubramanian, J.Harikumar, R. F. Benson, W. W. L. Taylor, and B. W. Reinisch (2004), Diagnostics of magnetospheric electron density and irregularities at altitude <5000 km using whistler and Z mode echoes from radio sounding on the IMAGE satellite, *J. Geophys. Res.*, 109, A11212.

Sonwalkar, V.S. (2006), The Influence of Plasma Density Irregularities on Whistler-Mode Wave Propagation, *Lect. Notes Phys.*, 687, 141191.

Sonwalkar, V.S., S. Hazra, K. Mayank, A. Reddy, D.L. Carpenter, and B.W. Reinisch (2009), Whistler Mode Echoes Observed Below 2,000 km Altitude by Radio Plasma Imager (RPI) on IMAGE: Radio Sounding of Electron Density and Ion Composition (H+, He+, O+), American Geophysical Union, Fall Meeting 2009.

Sonwalkar, V. S., D. L. Carpenter, A. Reddy, R. Proddaturi, S. Hazra, K. Mayank, and B. W. Reinisch (2011a), Magnetospherically reflected, specularly reflected, and backscattered whistler mode radio sounder echoes observed on the IMAGE satellite: 1. Observations and interpretation, J. Geophys. Res., 116, A11210, doi:10.1029/2011JA016759.

Sonwalkar, V. S., A. Reddy, and D. L. Carpenter, Magnetospherically reflected, specularly reflected, and backscattered whistler mode radio sounder echoes observed on the IMAGE

satellite: 2. Sounding of electron density, ion effective mass (meff), ion composition (H+, He+, O+), and density irregularities along the geomagnetic field line (2011b), *J. Geophys. Res.*, 116, A11211, doi:10.1029/2011JA016760.

Stix, T.H. (1962), The Theory of Plasma Waves, 283 pp., McGraw-Hill, New York.

Su, Y. Z., K.-I. Oyama, G. J. Bailey, S. Fukao, T. Takahashi, and H. Oya (1996), Longitudinal variations of the topside ionosphere at low latitudes: Satellite measurements and mathematical modelings, *J. Geophys. Res.*, 101(A8), 1719117205, doi:10.1029/96JA01315.

Su, Y. Z., G. J. Bailey, and S. Fukao (1999), Altitude dependences in the solar activity variations of the ionospheric electron density, *J. Geophys. Res.*, 104, 14,879 14,891.

Tarcsai, G., P. Szemeredy, and L. Hegymegi, Average electron density profiles in the plasmasphere between L = 1.4 and 3.2 deduced from whistlers, *J. Atmos. Terr. Phys.*, 50, 607611, 1988.

The Earth's Ionosphere, NASA's hand book 1971.

Thomas, J. O., A. Y. Sader (1964), Electron density at the Aloutte orbit, *J. Geophys. Res.*, 69, 4561.

Torr, M. R., J. C. G. Walker, and D. G. Torr (1974), Escape of fast oxygen from the atmosphere during geomagnetic storms, *J. Geophys. Res.*, 79(34), 52675271, doi:10.1029/JA079i034p05267.

Tsyganenko, N. A. (1995), Modeling the Earth's magnetospheric magnetic field confined within a realistic magnetopause, *J. Geophys. Res.*, 100(A4), 55995612, doi:10.1029/94JA03193.

Tsyganenko, N. A., and D. P. Stern (1996), Modeling the global magnetic field and the large-scale Birkeland current system, J. Geophys. Res., 101, 27817.

Triskova, L., Truhlik, V., J. Smilauer (2003) An empirical model of ion composition in the outer ionosphere, *Adv. Space Res.*, 31 (3), 653.

Triskova, L., Truhlik, V., J. Smilauer (2006), An empirical topside electron density model for

calculation of absolute ion densities in IRI, *Adv. Space Res.*, 37, 928934.

Titheridge, J.E. (1976), Ion transition heights from topside electrondensity profiles. Planetary and Space Science 24, 229245.

Truhlik, V., L. Triskova, and J. Smilauer (2005), Manifestation of solar activity in the global topside ion compositiona study based on satellite data, *Ann. Geophys.*, 23, 25112517.

Truhlik, V., D. Bilitza, L. Triskova (2012), A new global empirical model of the electron temperature with the inclusion of the solar activity variations for IRI, *Earth Planets Space*, 64, 531.

Tu, J., J. L. Horwitz (2004), simulation of polar cap field alligned electron density profiles measured with IMAGE radio plasma imager, *J. Geophys. Res.*, 109, A07206.

Tu, J., P. Song, B.W. Reinisch, X. Huang, J. L. Green, H. U. Frey, P. H. Reiff (2005), Electron density images the middle and high latitude magnetosphere in response to solar wind, *J. Geophys. Res.*, 110, A12210.

Tu, J., P. Song, B. W. Reinisch, J. L. Green, and X. Huang (2006), Empirical specification of field-aligned plasma density profiles for plasmasphere refilling, *J. Geophys. Res.*, 111, A06216, doi:10.1029/2005JA011582.

Tu, J. P. Song, B.W. Reinisch, J. L. Green (2007), Smooth electron density transition from plasmasphere to the sub auroral region, *J. Geophys. Res.*, 112, A05227.

Tulasi Ram, S., C. H. Liu, S.Y. Su, and R. A. Heelis (2010), A comparison of ionospheric O+/light ion transition height derived from ioncomposition measurements and the topside ion density profiles over equatorial latitudes, *Geophys. Res. Lett.*, 37, L20107, doi:10.1029/2010GL045199.

Walker, A. D. M., The theory of Whistler propagation (1976), *Rev. Geophys.*, 14, 629.

Wanliss, J. A., D. O. Cersosimo (2006), Scaling properties of high latitude magnetic field data during different magnetospheric conditions, *Int. Conf. Substorms-8*, 325.

Webb, P., R. Benson, R. Denton, J. Goldstein, L. Garcia, and B. Reinisch (2007), An inner magnetospheric electron density database determined from IMAGE/RPI passive dynamic spectra, *Eos Trans. AGU*, 88(52), Fall Meet. Suppl., Abstract SM12A-04.

Williams, D. J. (1985), Dynamics of the Earths ring current: Theory and observation, *Space Sci. Rev.*, 42(3-4), 375396.

Yue, X., W.S. Schreiner, J.Lei, C.Rocken, Y.H. Kuo, W.Wan, Climatology of ionospheric upper transition height derived from COSMIC satellites during the solar minimum of 2008 (2010), *J. Atmos. Solar-Terr. Phys.*, 72, 1270.

Yue, X., W. S. Schreiner, C. Rocken, and Y.-H. Kuo (2013), Validate the IRI2007 model by the COSMIC slant TEC data during the extremely solar minimum of 2008, *Adv. Space Res.*, 51, 647-653.

Zhang, X., J. Qian, and X. Shen (2014), Solar cycle variation of the electron density in the topside ionosphere at local nighttime observed byDEMETER during 20062008, *J. Geophys. Res.*, 119, 38033814, doi:10.1002/2013JA019463.